EMERGENT FUNCTIONALITY AND CONTROLLABILITY IN BEAMFORMING SYSTEM

Han Ren

Dissertation Prepared for the Degree of

DOCTOR OF PHILOSOPHY

UNIVERSITY OF NORTH TEXAS

December 2017

APPROVED:

Yuankun Lin, Major Professor
Hualiang Zhang, Committee Member
Xinrong Li, Committee Member
Eliezer Oren, Committee Member
Shengli Fu, Chair of the Department of Electrical Engineering
Costas Tsatsoulis, Dean of the College of Engineering
Victor Prybutok, Dean of the Toulouse Graduate School

Ren, Han. *Emergent Functionality and Controllability in Beamforming System*. Doctor of Philosophy (Electrical Engineering), December 2017, 113 pp., 7 tables, 69 figures, 127 numbered references.

This dissertation presents beamforming designs. Using novel techniques and methods, the performance of the beamforming is improved on dual-band, tri-band, flexible function, tunable function in THz, and dynamic controllability on incident wave.

ACKNOWLEDGEMENTS

I would never have been able to finish my dissertation without the guidance of my committee members, help from friends, and support from my family and wife.

I would first like to thank my major professor Dr. Yuankun Lin, who has the attitude and the substance of a genius. You supported me greatly and were always willing to help me. I would also like to express the deepest appreciation to my former professor, Dr. Hualiang Zhang, for his excellent guidance, caring, and patience, and for providing me with an excellent atmosphere for doing research in last six years. His expertise in the RF and microwave fields improved my research skills and prepared me for future challenges.

I would like to thank my committee member, Professor Xinrong Li for his helpful suggestions and valuable comments during my Ph.D. program. In addition, I am grateful to Dr. Oren Eliezer of PHAZR for providing advice from both industrial and academic point of view. I want to thank you for your excellent cooperation and for all of the opportunities I was given to conduct my research and publications.

I want to thank all of my lab mates for their help, support, and cooperation. Finally, I want to express thanks to my family, especially my wife for her constant source of inspiration and support.

TABLE OF CONTENTS

Page

LIST OF TABLES

Page

LIST OF FIGURES

Page

CHAPTER 1

INTRODUCTION

1.1 Background

Beamforming is a signal processing technique for directional signal transmission or reception. It is achieved by combining elements in an array in such a way that signals at particular angles experience constructive interference while others experience destructive interference. If the transmitting mode uses the conventional technique without beamforming, the signal will be transmitted in all directions. The transmitting gain would be quite small, causing a short transmitting distance. For the receiving mode, this conventional technique also encounters high noise and interference. As a result, the overall system features a low efficiency. If the beamforming is applied, the most signal can be transmitted in a desired direction with a high gain and a long range. Meanwhile, the noise and interference are also minimized, and the high efficiency is also realized. Therefore, the beamforming is more advanced for signal communication.

Currently, beamforming has be applied in numerous applications, such as wireless communication, radar, imaging, biomedicine, seismology, sonar, and acoustics. In all applications, beamforming can be used at both the transmitting and receiving ends in order to achieve spatial selectivity. For transmitting, the beamforming is used to control the phase and relative amplitude of the signal at each element in transmitter array, in order to create a pattern of constructive and destructive interference in the wave front. For receiving, information from different sources is combined in a way where the expected pattern of radiation is preferentially observed.

To realize the beamforming, the most common way is to add the weight vectors of the signals. In mathematics, the weight vector is a complex number consisting of real part and imaginary part. The real part dominates the amplitude while the imaginary part represents the phase. In the radiation pattern generated by the beamforming, the amplitude component control the sidelobe level and main beam width, and the phase component control the angle of the main beam and nulls. As a results, both amplitude an phase are the most critical parameters in the beamforming designs. The beamforming can be divided into two major types: digital beamforming and RF beamforming. In digital beamforming, the implementation of time delays are easy to achieve, and the signal is converted from analog signal to digital one by using A/D converter. However, multiple data converters are often required, leading a high cost and a large size. For RF beamforming, various RF devices are employed, such as phase shifter, directional coupler, power divider, and power combiner. This type of beamforming is available to design in a very small chip. The true time delay is achieve by phase shifter while the large bandwidth and low power consumption are also available in RF beamforming.

To design RF beamforming, the most common method is to apply phased array (it is often called as beamformer). Since Nobel Laureate Luis Alvarez designed a phased array antenna in a rapidly-steerable radar system for “ground-controlled approach” during World War II, phased arrays have been used as a beamformer around for more than half a century. In the early period, the phased array was the most advanced technology and only employed in military. The major applications were national missile defense and space probe communication. Especially in radar system, the phased array is an important component to detect and track the target’s location. In recent years, phased array’s

demand in the commercial area started to increase rapidly and the advanced technologies were also shared to the public, various application of the phased array has started to be applied in civil areas.

1.2 Motivation

5th generation wireless system (5G) has finished prototype and trial. It will be deployed in 2020. In 5G, faster speed, wider band, and higher efficiency will be the major requirement. Based on the current beamforming techniques and design, there are several technological bottlenecks, which limit the development of beamformers. First, the most dual-band operation designs feature a narrow range of the frequency ratio. Second, there is few tri-band operation design. Third, most phased array designs cannot achieve multiple and flexible function. Fourth, dynamic phase and amplitude tuning is impossible using current technology. Finally, the gain performance needs to be improved. Therefore, it is meaningful to find some novel ideas and approaches to improve the beamforming performance.

1.3 Overview of Dissertation

This dissertation presents several novel approaches to improve the beam-forming system. Chapter 2 introduces the principle of phased array and presents the fundamental design equations. In addition, the classification of feeding networks using in the phased array is also discussed.

Chapter 3 presents a novel design of dual-band 3 dB branch-line coupler. To realize the dual-band operation, a new dual-band transmission line is proposed.

Specifically, the proposed dual-band transmission line is constructed by coupled transmission lines and open-ended stubs. Using this dual-band transmission line, the designed branch-line coupler can achieve dual-band operation with a wide range of realizable frequency ratios (i.e. ratio between the two operating frequencies) and feature a flexible structure. To facilitate the design, analytical design equations are derived using the *ABCD*-matrix. To verify the design concept, a planar dual-band 3 dB branch-line coupler operating at 2/5.2 GHz is designed, fabricated, and characterized. Good simulation and measurement results are obtained to verify the design theory.

In Chapter 4, a novel multi-band branch-line coupler employing multi-band transmission lines is designed to operate at three different frequencies. To realize multi-band operations, a Pi-type-based multi-band transmission line network with open- and short-ended stubs is employed. Specifically, the Pi-type line is applied to realize the dual-band operation at the first two working frequencies. For the third operating frequency, the open- and short-ended stubs are tapped at the center of the Pi-type line. *ABCD*-matrix is employed to derive the design formulas for the proposed tri-band transmission line. To verify the design concept, a planar coupler operating at 1/2.5/4.5 GHz is designed and fabricated. The simulation and measurement results show good agreement with the design theory.

Chapter 5 presents a novel topology of 4×4 Butler matrix, which can realize relatively flexible phase differences at the output ports. The proposed Butler matrix employs couplers with arbitrary phase-differences to replace quadrature couplers in the conventional Butler matrix. By controlling the phase differences of the applied couplers, the progressive phase differences among output ports of the proposed Butler matrix can

be relatively flexible. To facilitate the design, closed-form design equations are derived and presented. For verifying the design concept, a planar 4×4 Butler matrix with four unique progressive phase differences (-30°, +150°, -120°, and +60°) is designed and fabricated. At the operating frequency, the amplitude imbalance is less than 0.75 dB, and the phase mismatch is within ±6°. The measured return loss is better than 16 dB, and the isolation is better than 18 dB. The bandwidth with 10 dB return loss is about 15%.

Several new designs of tunable terahertz devices using graphene parallel-plate waveguide (GPPWG) are introduced in Chapter 6. Graphene parallel-plate waveguide features tunable propagation constant and characteristic impedance which can be controlled by the external biasing voltage (through electrical gating). Specifically, GPPWG with the T-type structure is proposed, which can realize full-scale tunability (e.g. tunable operating frequency, characteristic impedance, and electrical length). To facilitate the design, closed-form design equations are derived. Based on the proposed GPPWG, a variety of two- and multiple-port tunable devices are designed in the terahertz (THz) range, including a phase shifter with tunable frequency, a phase shifter with tunable phase difference, and a coupler with tunable phase difference.

In Chapter 7, we report a novel design of electrically tunable metasurface, which is able to dynamically control the phase and amplitude of the electromagnetic wave simultaneously. The proposed metasurface consists of two major parts: phase control part with dominant phase tuning and amplitude control part with dominant amplitude tuning. Dynamic tuning on phase and amplitude is realized by loading several varactor diodes into the phase and amplitude control part respectively. The simulation of metasurface can achieve full 360° phase control and an amplitude control with a wide

range on the transmission wave. Both phase and amplitude are independently tuned by the varactor diodes. As an implementation, a metasurface with one array of three unit cells is fabricated and measured in a TEM cell. The measurement results demonstrate a full range of transmission phase tuning (360°) and a wide ratio of normalized transmission amplitude tuning (1/16). For the implementation, the proposed metasurface is also applied to constitute a phased array, which realize a beam steering function. The schematic structure of the proposed metasurface is also available to obtain similar phase control and amplitude control of the reflection wave.

Finally, the last chapter concludes the dissertation and outlines achievement in the Ph.D. program. Furthermore, direction for the future work is also presented.

CHAPTER 2

PRINCIPLE OF PHASED ARRAY

2.1 Introduction

Phased array is the common way to realize RF beamforming, and it is always constructed by RF device, such as phase shifter, crossover, directional coupler, power divider, and power combiner. In antenna design theory, a phased array is a classical antenna array which is a group of multiple identical antennas fed by a single signal source. It can generate a radiation pattern with a unique radiation beam angle. By varying the value of the phase difference between two adjacent antenna elements, the radiation angle of the main beam can be steered. This forms the fundamental operating mechanism of the phased array, leading the most common beamformer.

2.2 Structure of Phased Array

The general configuration of a phased array with N antenna elements is shown in Fig. 2.1. In the antenna array, each two adjacent antenna elements are spaced by a distance d along the horizontal axis. When the antenna array is employed for the transmitting mode, all antenna elements are assigned with identical amplitudes while each succeeding antenna element generates a progressive phase with the value of β to realize a current excitation relative to the preceding one. To assign the special values of amplitude and phase for each antenna element, the feeding network should be employed, which can generate the identical magnitude response and the β progressive phase response to the antenna array. After feeding the input signal to go through the feeding network, there will be multiple signal sections, which will be transmitted by the antenna

elements. As a result, a radiation pattern will be generated, and the maximal gain will appear at a unique radiation angle θ. At the θ direction, the signal intensity is always the strongest among all regions.

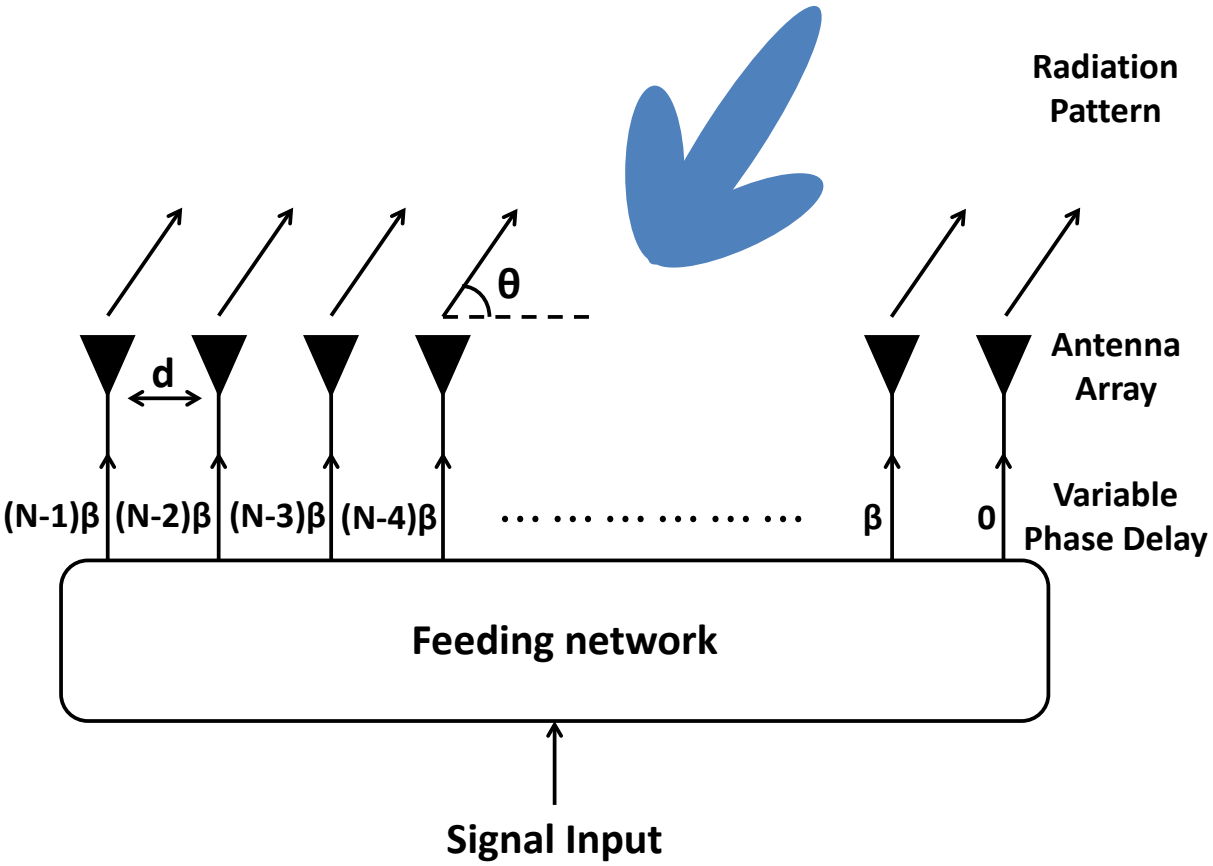

Figure 2.1: General configuration of *N*-element phased array.

Based on the structure of phased array, the total field of the array can be obtained by deriving the single element's field and the array factor (AF) generated by the antenna array:

$$E(\text{total}) = [E(\text{single element at reference point})] \times [\text{array factor}] \quad (2.1)$$

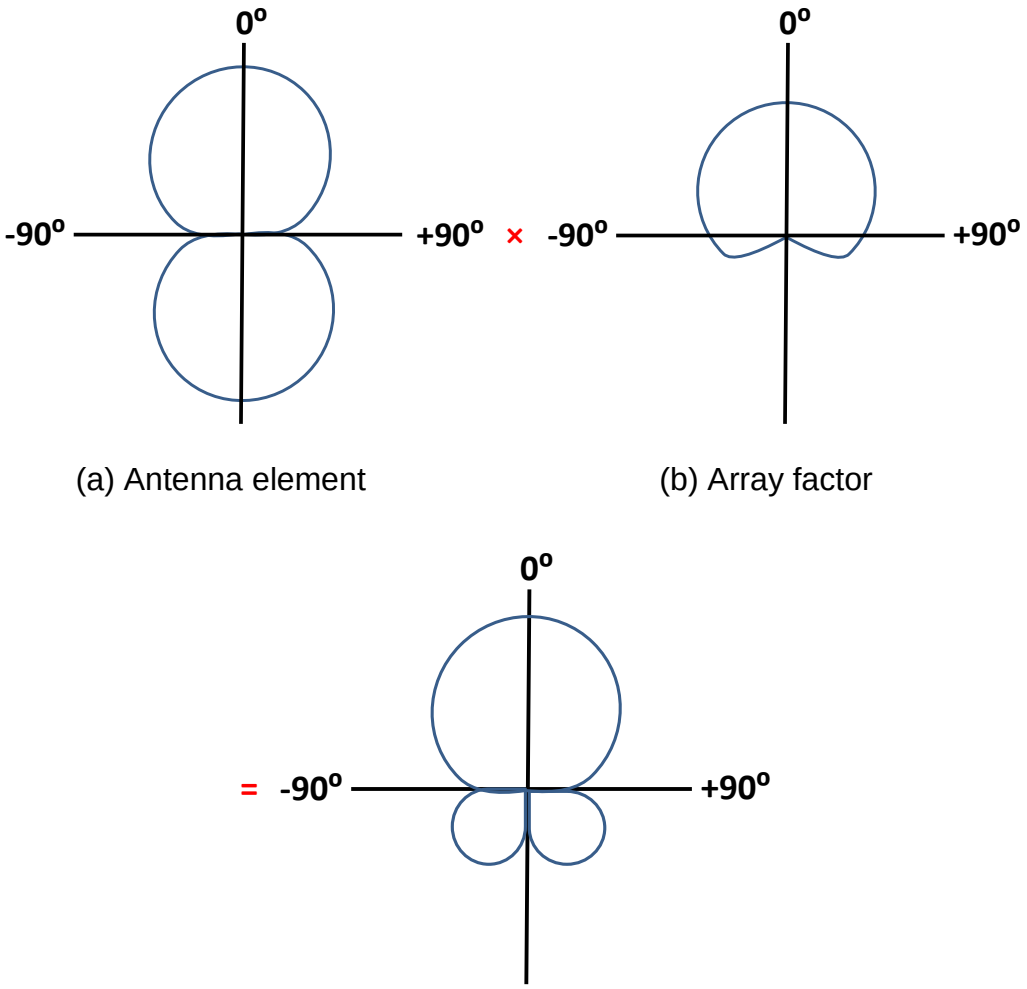

(a) Antenna element (b) Array factor

(c) Total radiation pattern

Figure 2.2: The pattern of (a) antenna element only and (b) array factor only (c) a dipole antenna array after pattern multiplication.

Eqn. 2.1 is the fundamental formula for the pattern multiplication of phased array, and it only applies for the assumption that all antenna elements are the same with each other. For instance, Fig. 2.2 shows three patterns of a single antenna element, array factor, and the antenna array respectively. Because both the single antenna element and the array factor have the main beam angle zero degree (as shown in Fig. 2.2(a)-(b)), the final radiation beam angle of the antenna array is also zero degree (as shown in Fig. 2.2(c)).

For nulls, the power of the signal is minimal. From the pattern of the array factor, minimal signal is at ±180º, so the null in the radiation pattern of the antenna array is located at ±180º.

For the *N*-element linear antenna array with uniform amplitude and spacing, the equation of the array factor (AF) can be written as Eqn. 2.2.

$$AF = 1 + e^{j(kd\cos\theta+\beta)} + e^{j2(kd\cos\theta+\beta)} + \cdots + e^{j(N-1)(kd\cos\theta+\beta)}$$

$$AF = \sum_{n=1}^{N} e^{j(n-1)(kd\cos\theta+\beta)}, \quad k = \frac{2\pi}{\lambda} \tag{2.2}$$

Here, λ is the wavelength of the signal, d and β is the distance and phase difference between two adjacent antenna elements respectively. The direction of the radiation beam is depended on the value of θ. Finally, Eqn. 2.2 can be summarized to Eqn. 2.3.

$$AF = \sum_{n=1}^{N} e^{j(n-1)\psi}, \ \psi = kd\cos\theta + \beta \tag{2.3}$$

Since most of phased array design for realizing beamforming, the value of main beam angle is an important and necessary design parameter, which can be derived by finding the direction of the maximum value of array factor in Eqn. 2.3. The maximal value of the array factor can be obtained when the design parameter ψ is equal to $2m\pi$ ($m = 0, \pm1, \pm2, \pm3$ ... ...). As a result, the main beam's angle in the radiation pattern can be written as Eqn. 2.4.

$$\theta_{main} = \cos^{-1}\left(\frac{2m\pi-\beta}{kd}\right), \ m = 0, \pm1, \pm2, \pm3 \ldots\ldots \tag{2.4}$$

From Eqn. 2.4, it is clear to show the relationship between beam angle θ, phase difference β, and element spacing d. These three parameters are often applied in the phased array designs.

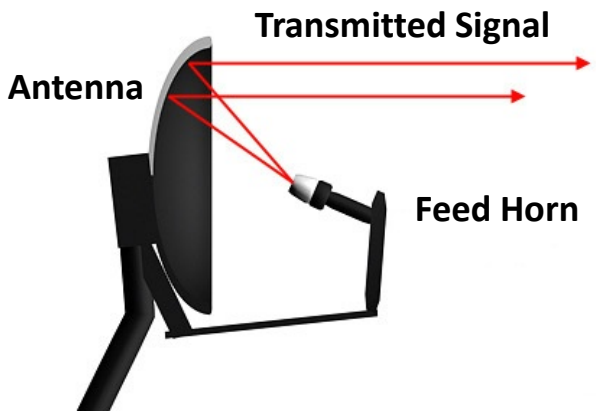

Figure 2.3: General diagram of the space feeding.

2.3 Classification of Phased Array

As mentioned in the last section, a general phased array is usually designed for beamforming. It is often realized by a feeding network connected with an antenna array. Generally speaking, the feeding network is a special layout consisting various RF devices to distribute the input signal into each element in an antenna array. Based on different design goal and application, the feeding network can generate various values for magnitude and phase for each antenna element. The classification of phased array is mainly based on the topology used in the feeding network. There are total three basic types of feeding network: space feeding, constrained feeding, and semi-constrained feeding which is a combination of the space and constrained feeding [1]. Fig. 2.3 exhibits the space feeding, which is usually realized by installing a separate feed horn at an appropriate distance from the antenna array [2]. Because there is a free space between the feed horn and antenna array, this type of feeding network always has a complex structure with a large size. It is not available for the 2D phased arrays. On the other hand, the constrained feeding is considered as the best way to feed the antenna array. This

category generally consists of some transmission lines and various microwave devices. The constrained feeding can be classified into two three major types: parallel-fed, series-fed [3], and Butler matrix. These three types are the most common methods to design the feeding network. Their structures are also discussed below.

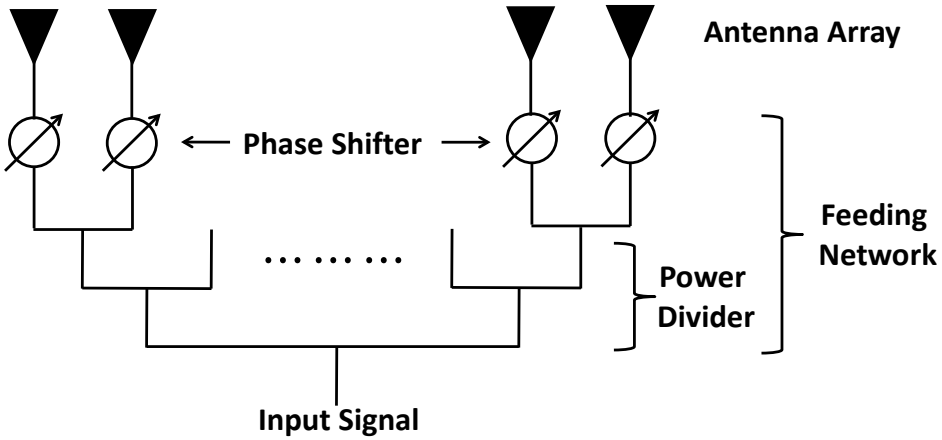

Figure 2.4: General diagram of the phased array applying parallel-fed network.

2.3.1 Parallel-Fed Network

In parallel-fed network, the input signal is divided by the power divider in a corporate tree network to generate multiple signal sections for feeding all elements in the antenna array (as shown in Fig. 2.4). Besides the power divider, phase shifters with the progressive phase response are also employed for each antenna element [4]. In an *N*-element phased array using parallel-fed network, the required amount of power divider and phase shifter is $N-1$ and $2N$ respectively. As a result, the performance of phased array with parallel-fed network critically depends on the numbers of the power dividers and phase shifters. These two components are often the major source to generate loss, such as insertion loss.

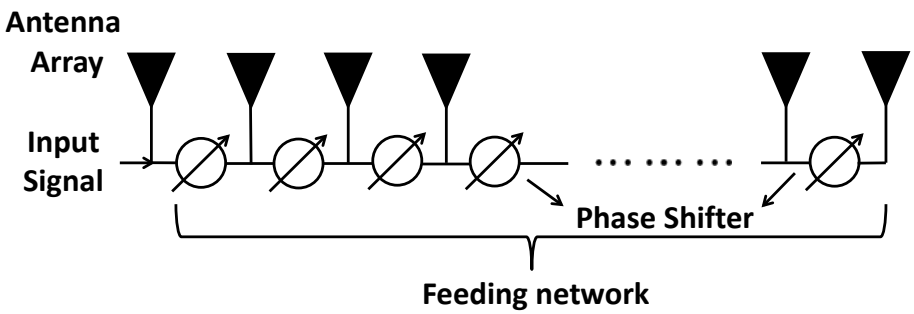

Figure 2.5: General diagram of the phased array applying series-fed network.

2.3.2 Series-Fed Network

In series-fed network, the input signal is fed from one end of the feeding network and coupled serially to each antenna element as shown in Fig. 2.5. Between two adjacent antenna elements, there is a phase shifter with the identical phase response. For each antenna path, a directional coupler is also deployed to split the signal. The main advantage of series-fed network is it features less number of phase shifter than the parallel-fed network, leading less insertion and radiation losses of the phased array [5]. The compact size with low cost is also realized in the parallel-fed network. Moreover, the series-fed network has a flexibility on the phase tuning range of the phase shifters. In an *N*-element phased array with series-fed network, the required number of phased shifters is usual less than the parallel-fed network (normally by a factor of $(N-1)$). However, the loss is still introduced by the consecutive couplers and phase shifters, so it is very difficult to generate identical magnitude for each antenna element using the series-fed network.

2.3.3 Special Network – Butler Matrix

The Butler matrix is a special type of beam-forming network, which was first described by Jesse Butler and Ralph Lowe in 1961 [6]. Depending on which of N inputs

is accessed, the antenna beam is steered in a specific direction in one plane; Butler matrices can be combined in two "layers" to facilitate 3D scanning. It performs a similar function to a Rotman lens, or a phased array antenna system. The primary characteristics of the Butler matrix are: 1) N inputs and N outputs, with N usually 4, 8 or 16; 2) Inputs are isolated from each other; 3) Phases of N outputs are linear with respect to position, so beam is tilted off main axis; 4) None of the inputs provides a broadside beam; 5) The phase increment between the outputs depends on which input you use. Because Butler matrix is a passive reciprocal network, so it works the same when it transmits energy as when it receives energy. The Butler matrix featuring a symmetrical structure is composed of couplers, crossovers, and phase shifters. For example, the 4×4 Butler matrix has four input and output ports, which consists of four 3 dB hybrid couplers, two 45° phase shifters, two crossovers (as shown in Fig. 2.6).

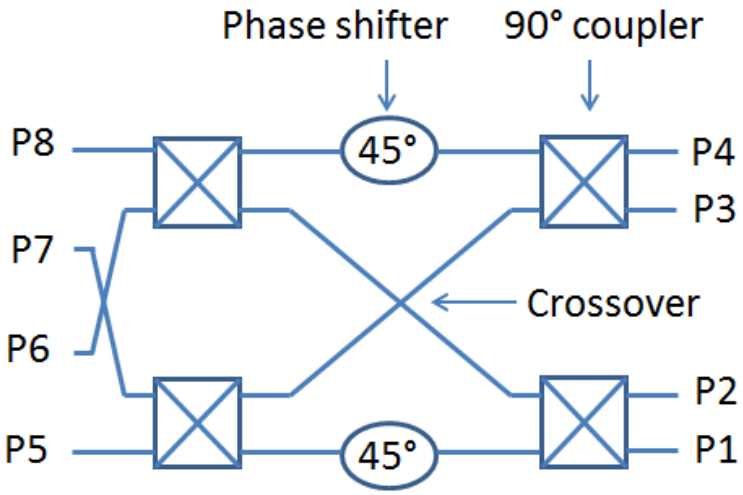

Figure 2.6: Configuration of a conventional 4×4 Butler matrix with four input ports P1-P4 and four output ports P5-P8.

CHAPTER 3

NEW DUAL-BAND BRANCH-LINE COUPLER WITH COUPLED-LINE BASED DUAL-AND TRANSMISSION LINES

3.1 Background and Motivation

With the recent development in modern communication systems, such as wireless local area network systems (WLAN) and high-speed local area networks (LANs), dual-band or multiband beam-forming becomes an attractive feature with increased demand. For example, the applications of dual-band microwave devices [7]-[27] (including baluns, filters & duplexers, power dividers, couplers, etc.) in communication systems can lead to both size and cost reductions of the whole systems (since it can support multiple frequency bands simultaneously). Among various passive microwave components, the 3-dB branch-line coupler is one of the fundamental circuit components. It has been applied extensively in various microwave circuits including power amplifiers, mixers, multipliers, data modulators, and antenna feeding networks [28].

Up to now, owing to the efforts of a lot of researchers, several different structures of dual-band branch-line couplers have been proposed. In [29], additional open- or short-ended stubs are tapped to the end of each branch-line to achieve the dual-band operation. In [30], the composite right/left-handed transmission lines are employed in the dual-band design. Couplers using the stepped-impedance section with two shunt open stubs to replace the quarter-wavelength line are presented in [31]. A coupler with rectangular patch structure [32] can operate at two arbitrary frequency bands. In [33], the authors presented a dual-band operation scheme using port extensions. A dual-band coupler employing stepped-impedance-stub lines tapped in the center of branch line is presented

in [34]. In [35], a compact dual-band coupler consisting of three quarter-wave coupled-line sections is proposed. However, all of the above-mentioned dual-band couplers have a narrow range of frequency ratios and the implementations of them are not flexible. Therefore, to address these issues (especially to achieve a wider range of realizable frequency ratios), more new dual-band branch-line couplers need to be proposed.

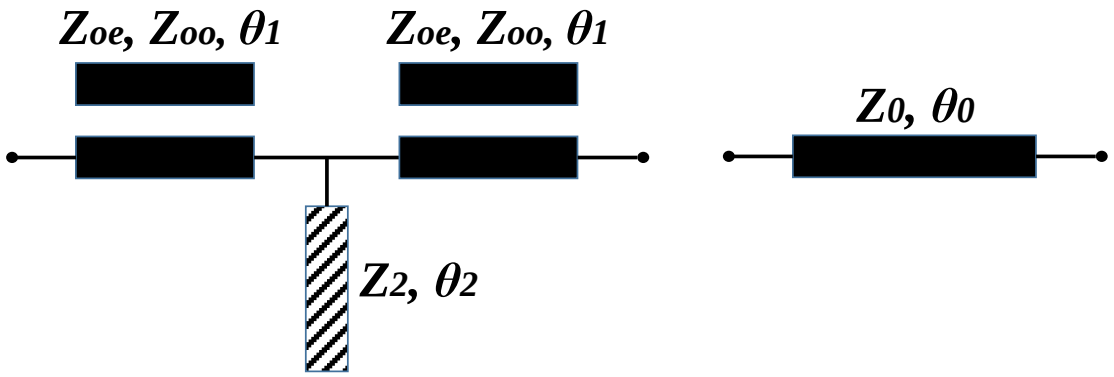

Figure 3.1: Schematic diagram of (a) proposed dual-band transmission line based on coupled-lines and (b) the equivalent transmission line of the structure shown in (a).

3.2 Design and Analysis

Fig. 3.1 shows the schematic diagram of the proposed dual-band transmission line and the corresponding equivalent transmission line of it at the two operating frequencies. From Fig. 3.1(a), the proposed dual-band transmission line consists of two sections of coupled transmission lines with identical structures (within the coupled-line, the top section is open-circuited at its two ends and the bottom section is connected with input/output signals). An additional open-ended stub is tapped at the center of these two coupled-line sections. As labeled in Fig. 3.1(a) (the black-colored sections), the even- / odd-mode characteristic impedances of the coupled-line are Z_{oe}, Z_{oo}, and the electrical length of it is θ_1. The section marked with shaded lines is the open-ended stub with the

characteristic impedance of Z_2 and the electrical length of θ_2. For a single coupled-line section (either the left or the right coupled-line section as shown in Fig. 3(a)), its *ABCD*-matrix can be derived as:

$$\begin{bmatrix} A & B \\ C & D \end{bmatrix}_{Coupled} = \begin{bmatrix} \cos\theta_1 & \frac{j(Z_{oe}+Z_{oo})}{2\csc\theta_1} \\ \frac{j2}{(Z_{oe}+Z_{oo})\csc\theta_1} & \cos\theta_1 \end{bmatrix} \tag{3.1}$$

The total *ABCD*-matrix of the proposed dual-band transmission line can be written as the following:

$$\begin{bmatrix} A & B \\ C & D \end{bmatrix} = \begin{bmatrix} A & B \\ C & D \end{bmatrix}_{Coupled} \times \begin{bmatrix} A & B \\ C & D \end{bmatrix}_{Stub} \times \begin{bmatrix} A & B \\ C & D \end{bmatrix}_{Coupled} \tag{3.2}$$

where

$$\begin{bmatrix} A & B \\ C & D \end{bmatrix}_{Stub} = \begin{bmatrix} 1 & 0 \\ \frac{j}{Z_2\cot\theta_2} & 1 \end{bmatrix} \tag{3.3}$$

Substituting Eqn. 3.1 and 3.3 into Eqn. 3.2, the final formulas of the *ABCD*-parameters of the dual-band transmission line can be derived as:

$$A = D = \frac{2Z_2\cot\theta_2\,(\cot^2\theta_1 - 1) - \cot\theta_1\,(Z_{oe}+Z_{oo})}{2Z_2\cot\theta_2\,(\cot^2\theta_1 + 1)} \tag{3.4}$$

$$B = j\frac{4Z_2\cot\theta_1\cot\theta_2\,(Z_{oe}+Z_{oo}) - (Z_{oe}+Z_{oo})^2}{4Z_2\csc^2\theta_1\cot\theta_2} \tag{3.5}$$

$$C = j\frac{4\cos\theta_1}{(Z_{oe}+Z_{oo})\csc\theta_1} + j\frac{\cos^2\theta_1}{Z_2\cot\theta_2} \tag{3.6}$$

In principle, to support dual-band operations, the proposed structure needs to be equivalent to a conventional transmission line with the characteristic impedance of Z_0 and the electrical length of θ_0 (as shown in Fig. 3.1(b)) at the two assigned working frequencies. Correspondingly, the ABCD-matrix of it should be equal to that of the equivalent transmission line, yielding

$$\begin{bmatrix} A & B \\ C & D \end{bmatrix} = \begin{bmatrix} \cos\theta_0 & jZ_0 \sin\theta_0 \\ jY_0 \sin\theta_0 & \cos\theta_0 \end{bmatrix} \tag{3.7}$$

Realize where *A*, *B*, *C*, *D* are given in Eqn. 3.4 – 3.6, and $Y_0 = 1/Z_0$. By setting $A = \cos\theta_0$ and $B = jZ_0 \sin\theta_0$ (Based on the symmetrical structure of the proposed dual-band transmission line, only parameters *A* and *B* are needed), two important design equations can be obtained:

$$\frac{2Z_2 \cot\theta_2 (\cot^2\theta_1 - 1) - \cot\theta_1 (Z_{oe} + Z_{oo})}{2Z_2 \cot\theta_2 (\cot^2\theta_1 + 1)} = \cos\theta_0 \tag{3.8}$$

$$\frac{4Z_2 \cot\theta_1 \cot\theta_2 (Z_{oe} + Z_{oo}) - (Z_{oe} + Z_{oo})^2}{4Z_2 \csc^2\theta_1 \cot\theta_2} = Z_0 \sin\theta_0 \tag{3.9}$$

Meanwhile, to support the dual-band operation, the electrical lengths of transmission line sections within the proposed structure are assumed as the following:

$$\text{For } f_1, \quad \begin{cases} \theta_1 \\ \theta_2 \end{cases} \tag{3.10}$$

$$\text{For } f_2, \quad \begin{cases} n_1\pi - \theta_1 \\ n_2\pi - \theta_2 \end{cases} \tag{3.11}$$

where f_1 is the lower working frequency, and f_2 is the higher working frequency, n_1, n_2 = 1, 2, 3, ….

Based on Eqn. 3.10 and 3.11, the formulas of the electrical lengths θ_1 and θ_2 (referring to Fig. 3.1(a)) can be derived as:

$$\theta_1 = \frac{f_1}{f_1 + f_2} n_1\pi \quad @f_1 \tag{3.12}$$

$$\theta_2 = \frac{f_1}{f_1 + f_2} n_2\pi \quad @f_1 \tag{3.13}$$

Finally, the design procedures of the proposed dual-band transmission line can be summarized as follows:

1) Select the lower working frequency f_1 and the higher one f_2.

2) Choose suitable n_1, n_2 to obtain the values of θ_1 and θ_2 by Eqn. 3.12 – 3.13.

3) Solve Eqn. 3.8 – 3.9 to get the values of $Z_{oe}+ Z_{oo}$ and Z_2.

In general, by following the above design steps, the proposed dual-band transmission line can be designed to work as a transmission line with arbitrary impedance and electrical length at different combinations of working frequencies (f_1 and f_2). Moreover, according to design step (3) and design Eqn. 3.4 – 3.9, the dual-band operation of the proposed structure is determined by the sum of even- and odd-mode characteristic impedances (Z_{oe}, Z_{oo}). This property indicates that, for a given frequency ratio (f_2/f_1), different combinations of Z_{oe} and Z_{oo} can be applied as long as the total of them is the same. As a result, in practical implementations, the strip width and the gap between strips of the coupled-lines can be adjusted, without affecting the dual-band performance of the proposed structure. Due to such an implementation flexibility, the proposed dual-band transmission line can provide flexible structures and support a wide range of frequency ratios for dual-band applications (as will be shown in the next section).

3.3 Design of a Dual-Band Branch-Line Coupler

As mentioned before, the new dual-band branch-line coupler is designed using the proposed dual-band transmission line. Fig. 3.2 shows the configuration of it, where each section of the conventional single-band coupler has be replaced with dual-band lines. Specifically, as shown in Fig. 3.2, 50 Ω quarter-wavelength line and 35.35 Ω quarter-wavelength line are needed for the new coupler. The design details of these branch lines and the range of the frequency ratio are discussed below.

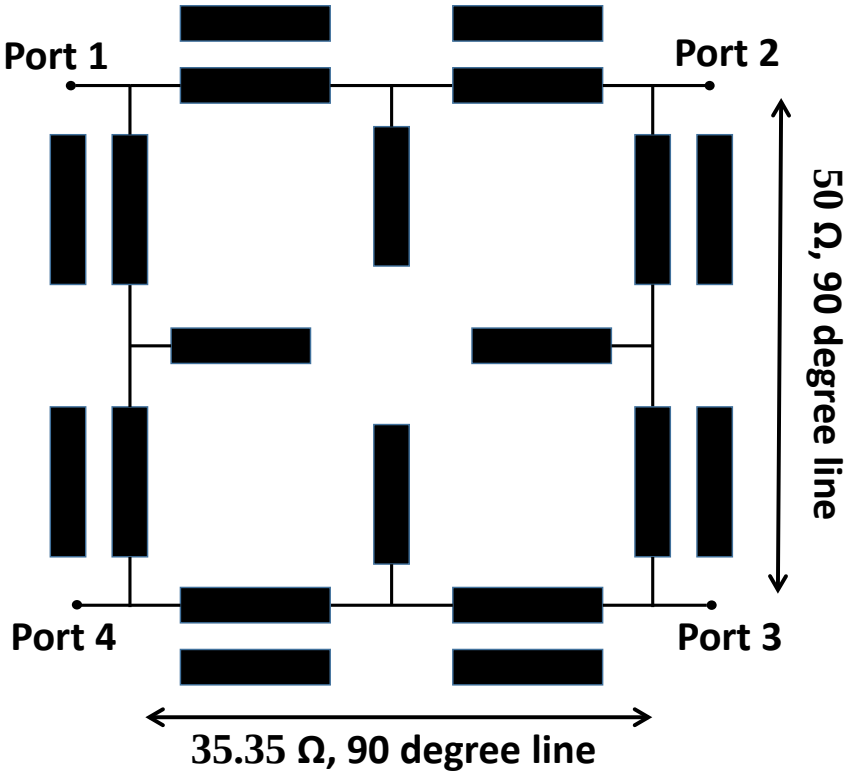

Figure 3.2: Configuration of proposed dual-band branch-line coupler with dual-band transmission lines.

For the branch line using 50 Ω quarter-wavelength transmission line, Z_0 = 50 Ω and θ_0 = 90°. Substituting the values of Z_0 and θ_0 into Eqn. 3.8 – 3.9, these two equations can be re-calculated as:

$$\frac{2Z_2 \cot\theta_2 \left(\cot^2\theta_1 - 1\right) - \cot\theta_1 \left(Z_{oe} + Z_{oo}\right)}{2Z_2 \cot\theta_2 \left(\cot^2\theta_1 + 1\right)} = 0 \tag{3.14}$$

$$\frac{4Z_2 \cot\theta_1 \cot\theta_2 \left(Z_{oe} + Z_{oo}\right) - \left(Z_{oe} + Z_{oo}\right)^2}{4Z_2 \csc^2\theta_1 \cot\theta_2} = 50 \tag{3.15}$$

Based on Eqn. 3.14 – 3.15, the design formulas for $Z_{oe} + Z_{oo}$ and Z_2 can be derived as:

$$Z_{oe} + Z_{oo} = \frac{100}{\tan\theta_1} \tag{3.16}$$

$$Z_2 = \frac{50 \tan\theta_2}{1 - \tan^2\theta_1} \tag{3.17}$$

Substituting Eqn. 3.12 – 3.13 into Eqn. 3.16 – 3.17, the final design formulas are shown as follows:

$$Z_{oe} + Z_{oo} = \frac{100}{\tan\left(\frac{n_1\pi}{1+R}\right)} \tag{3.18}$$

$$Z_2 = \frac{50\tan(\frac{n_2\pi}{1+R})}{1-\tan^2(\frac{n_1\pi}{1+R})} \tag{3.19}$$

where R is the frequency ratio ($R = f_2/f_1$).

For the branch line using 35.35 Ω quarter-wavelength transmission line, $Z_0 = 50/\sqrt{2}$ Ω and $\theta_0 = 90°$. Following the same analysis procedure, the design formulas for $Z_{oe} + Z_{oo}$ and Z_2 under this case can be derived as:

$$Z_{oe} + Z_{oo} = \frac{100}{\sqrt{2}\tan(\frac{n_1\pi}{1+R})} \tag{3.20}$$

$$Z_2 = \frac{50\tan(\frac{n_2\pi}{1+R})}{\sqrt{2}-\sqrt{2}\tan^2\left(\frac{n_1\pi}{1+R}\right)} \tag{3.21}$$

Applying Eqn. 3.18 – 3.21, the design parameters of $Z_{oe} + Z_{oo}$ and Z_2 for different branch lines of the coupler can be calculated under different frequency ratios. Moreover, by applying different combinations of n_1 and n_2, different solutions can be obtained.

To show the range of realizable frequency ratios of the proposed dual-band branch-line coupler, Eqn. 3.18 – 3.21 are employed to calculate the design values of $Z_{oe} + Z_{oo}$ and Z_2 for 50/35.35 Ω quarter-wavelength lines. The results are plotted in Fig. 3.3. The proposed coupler can also operate at a frequency ratio larger than 4). As shown in Fig. 3.3(a), within the range of frequency ratio from 1.3 to 4, the value of $Z_{oe} + Z_{oo}$ varies from 35 Ω to 310 Ω. For Z_2, the value of it is between 18 Ω and 130 Ω when the frequency

ratio is from 1.3 to 4 (as shown in Fig. 3.3(b)). All of these impedance values can be easily realized (using transmission lines such as microstrip lines). Therefore, it is shown that the new dual-band branch-line coupler using the proposed dual-band transmission lines can realize a wide range of frequency ratios, which is at least from 1.3 to 4 (it can be beyond this range).

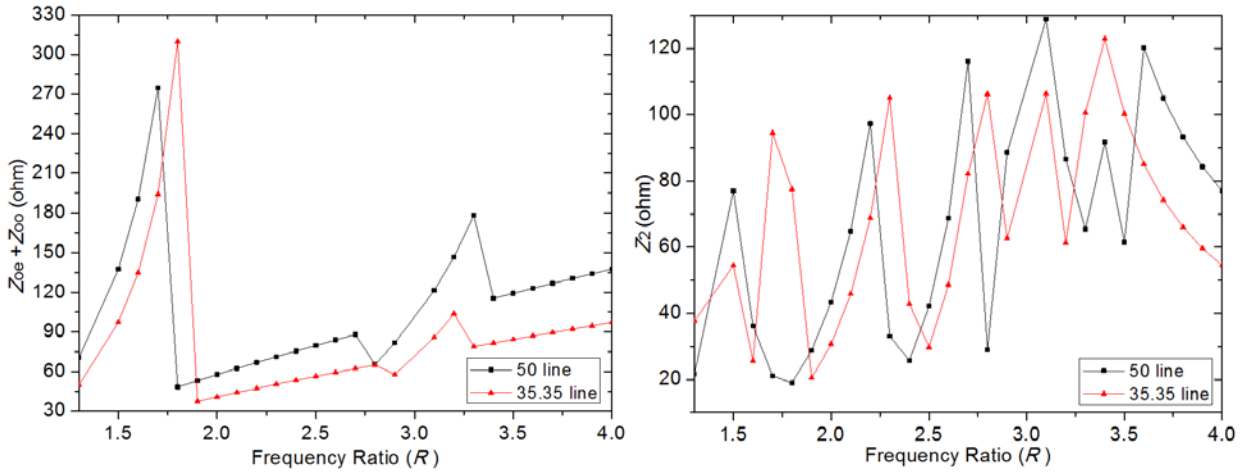

(a) (b)

Figure 3.3: (a) Variations of $Z_{oe} + Z_{oo}$ versus the frequency ratio R for different transmission lines (50 Ω and 35.35 Ω). (b) Variations of Z_2 versus the frequency ratio R for different transmission lines (50 Ω and 35.35 Ω).

3.4 Simulation and Measurement Results

To verify the proposed design concept, a dual-band microstrip branch-line coupler operating at 2/5.2 GHz (the lower frequency f_1 = 2 GHz and the higher frequency f_2 = 5.2 GHz) is designed. Based on the given frequency ratio (R = 2.6), the values of impedance and electrical length for each branch line within the coupler can be obtained. For the branch using 50 Ω quarter-wavelength line, the values of electrical length θ_1 and θ_2 are 50° and 150° evaluated at the lower frequency f_1 (using Eqn. 3.12 – 3.13, n_1 = 1 and n_2 = 3). Applying Eqn. 3.18, the value of $Z_{oe} + Z_{oo}$ is calculated to be 83.9099 Ω (in the practical implementation, Z_{oe} is set to be 50 Ω, and Z_{oo} is 33.9099 Ω). The value of characteristic

impedance Z_2 is found to be 68.6869 Ω by applying Eqn. 3.19. For the branch using 35.35 Ω quarter-wavelength line, the values of θ_1 and θ_2 are equal to 50° and 150°, which are evaluated at the lower frequency f_1 ($n_1 = 1$ and $n_2 = 3$). The value of $Z_{oe} + Z_{oo}$ is found to be 59.3333 Ω from (20). In the practical implementation, the values of Z_{oe} and Z_{oo} are set to be 39.3333 Ω and 20 Ω respectively. Applying Eqn. 3.21, the value of Z_2 is equal to 48.5690 Ω.

Applying the calculated design parameters, an experimental prototype is designed and simulated (the simulation is conducted by using the full-wave simulator HyperLynx). The simulation results of the 2/5.2 GHz dual-band branch-line coupler are shown in Fig. 3.4. Fig. 3.4(a) shows the simulation results of insertion loss. At the lower frequency of 2 GHz, the insertion losses $|S_{21}|$ and $|S_{31}|$ are equal to -3.11 dB and -3.18 dB respectively. At the higher frequency of 5.2 GHz, $|S_{21}|$ is equal to -3.42 dB, while $|S_{31}|$ is about -3.49 dB. For the return loss $|S_{11}|$, Fig. 3.4(b) shows that it is less than -20 dB at two working frequencies (-24.04 dB at 2 GHz and -35.36 dB at 5.2 GHz). The simulated isolation $|S_{41}|$ is equal to -26.23 dB and -24.61 dB at 2/5.2 GHz respectively (as shown in Fig. 3.4(b)). Fig. 3.4(c) shows the simulated phase responses ($\angle S_{31}$ and $\angle S_{21}$). The phase difference is close to 90° at two design frequencies (87.72° at 2 GHz and 87.87° at 5.2 GHz). Overall, the simulation results of the proposed dual-band branch-line coupler are in good agreement with the design theory.

For experimental verification, the proposed 2/5.2 GHz dual-band branch-line coupler is fabricated on RT/Duroid 5880 substrate with the substrate thickness of 0.787 mm and the dielectric constant of 2.2. Fig. 3.5 shows the photograph of the fabricated dual-band branch-line coupler (size: 47.67 mm × 51.78 mm ($0.32\lambda_0$ by $0.35\lambda_0$, λ_0 is the

free-space wavelength at 2 GHz)). The final measurement results are presented in Figs. 3.6 – 3.8.

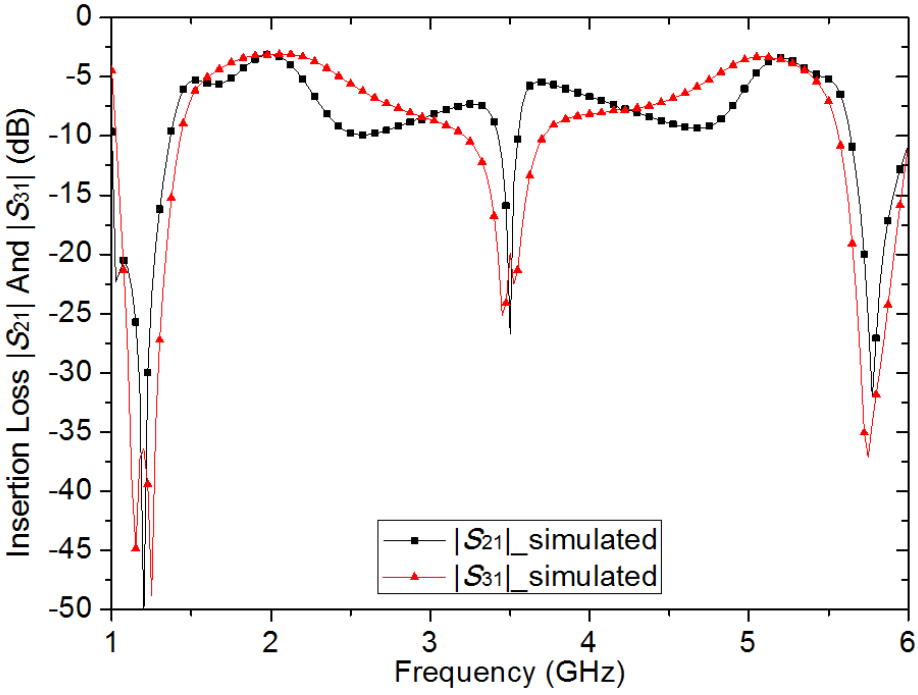

(a)

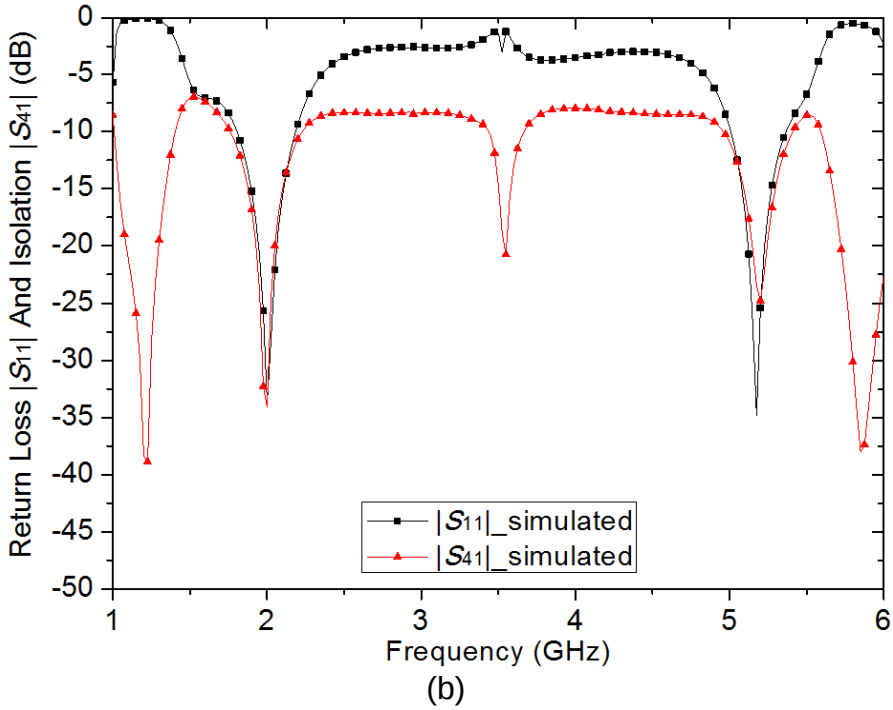

(b)

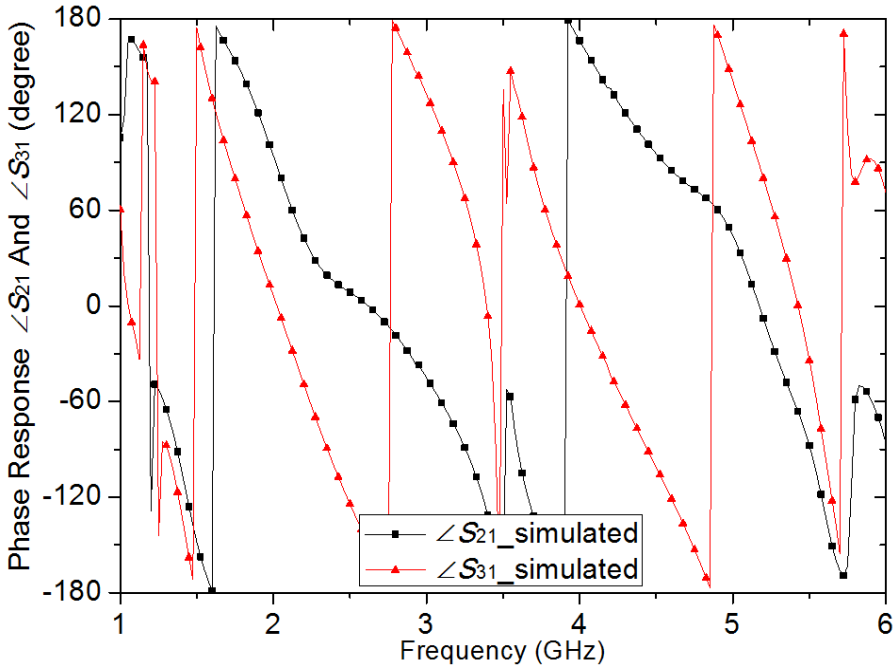

(c)

Figure 3.4: Simulation results of (a) insertion loss; (b) return loss and isolation; (c) phase response.

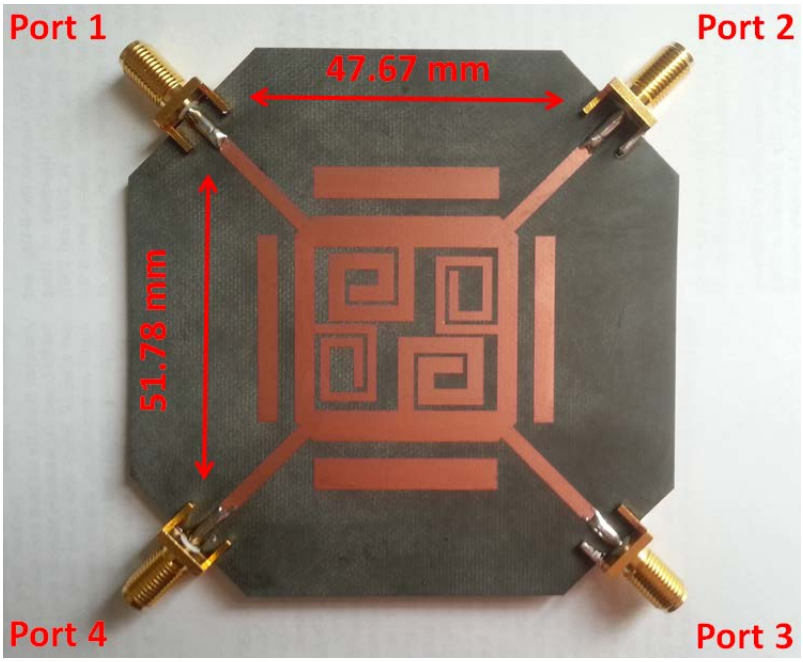

Figure 3.5: Photograph of the fabricated dual-band branch-line coupler.

At 2 GHz, the measured insertion losses $|S_{21}|$ and $|S_{31}|$ are -3.32 dB and -3.06 dB respectively, while $|S_{21}|$ and $|S_{31}|$ are about -3.55 dB and -3.72 dB at 5.2 GHz (as shown

in Fig. 3.6). The amplitude imbalance ($|S_{31}| - |S_{21}|$) is less than 0.3dB at both lower and higher frequencies. Fig. 3.7 shows the measured results of return loss |S11| and isolation |S41|. For |S11|, the measured value is -30.45 dB at 2 GHz and -23.49 dB at 5.2 GHz. Meanwhile, the isolation |S41| is equal to -26.49 dB and -29.03 dB at 2/5.2 GHz respectively. Fig. 3.8 shows the measured results of phase responses. The measured phase difference of between the two output ports is close to 90° at the two design frequencies (87.56° at 2 GHz and 88.51° at 5.2 GHz). The measured bandwidths of the designed coupler (assuming the amplitude mismatch is less than 0.5 dB and the phase mismatch (compared to 90°) is less than 5°) at the lower and higher bands are approximately 100 MHz and 275 MHz, respectively. Overall, it is observed that the measured results of the proposed dual-band branch-line coupler match well with the simulation results, which further verifies the design concept.

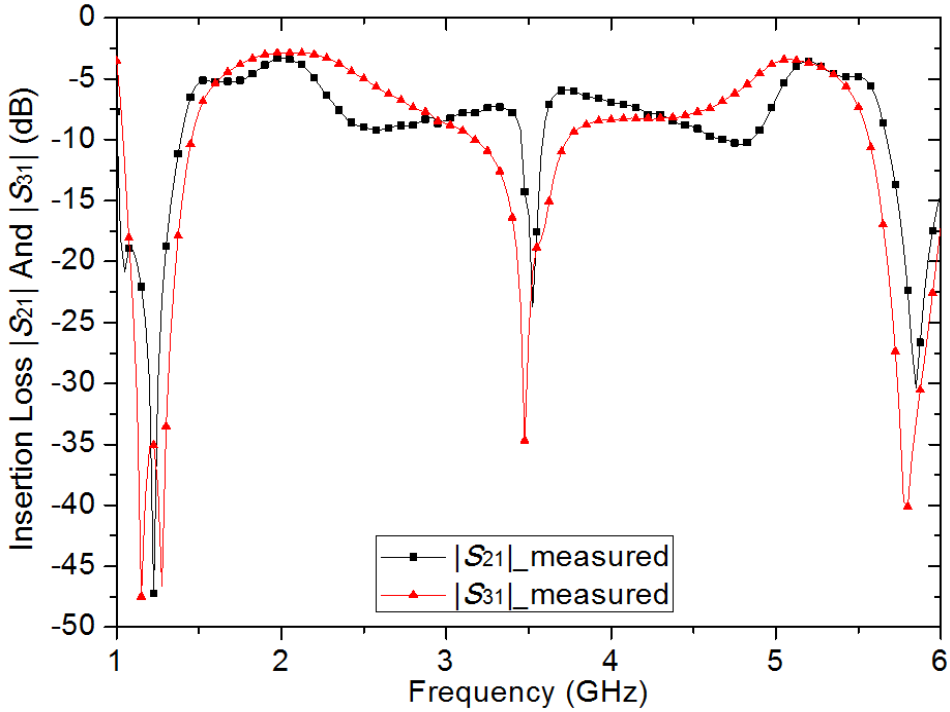

Figure 3.6: Measured results of insertion losses |S_{21}| and |S_{31}| of designed dual-band branch-line coupler.

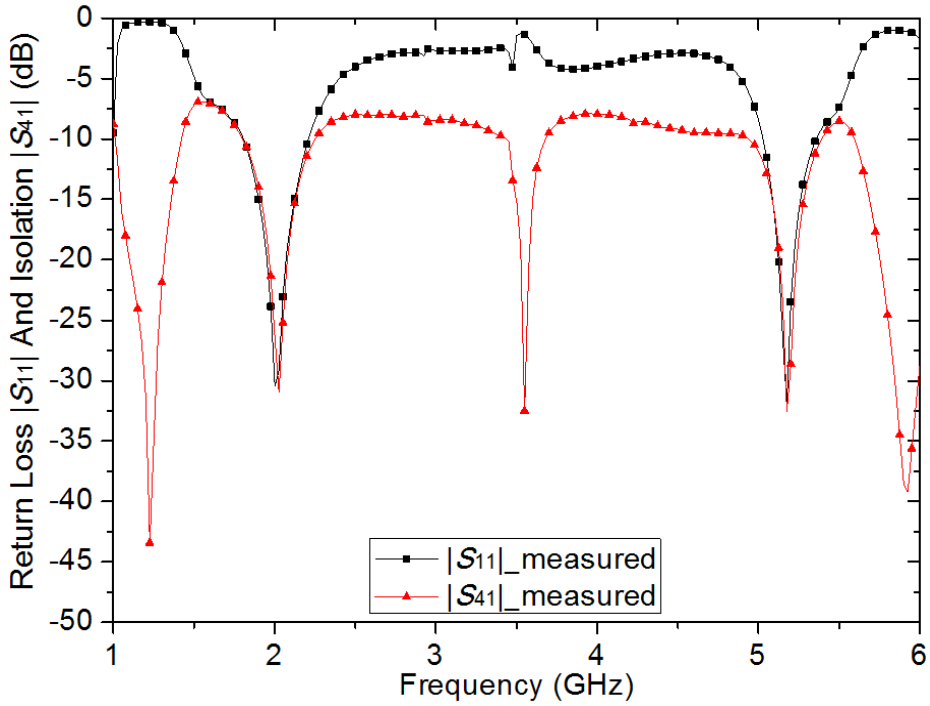

Figure 3.7: Measured results of return loss $|S_{11}|$ and isolation $|S_{41}|$ of designed dual-band branch-line coupler.

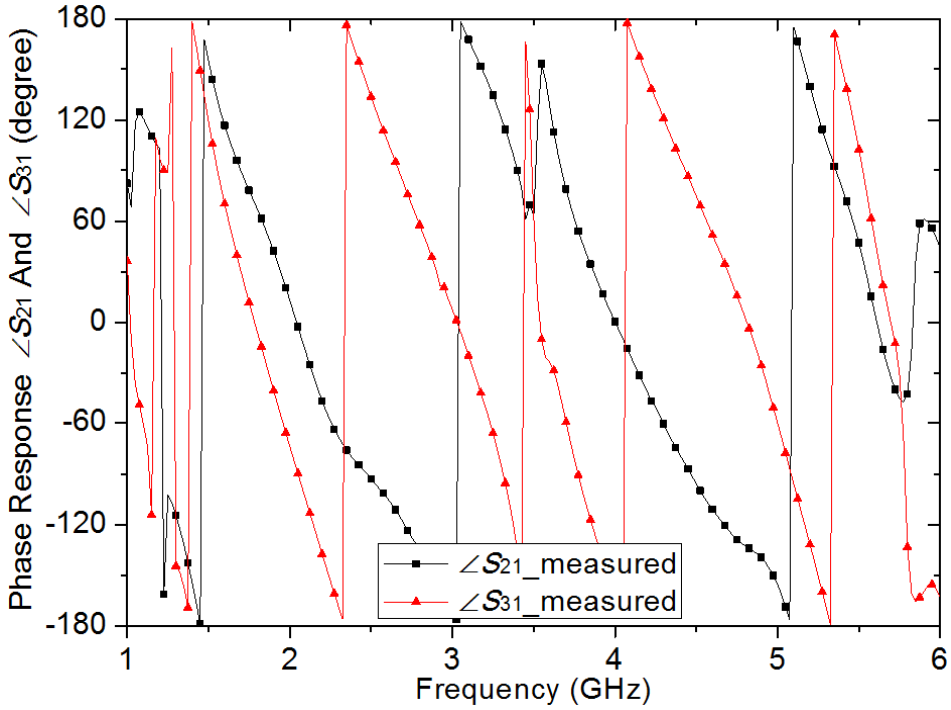

Figure 3.8: Measured results of phase response $\angle S_{31}$ and $\angle S_{21}$.

3.5 Conclusion

A novel design of dual-band branch-line coupler has been presented. To realize

the dual-band operation, a new dual-band transmission line is employed. The proposed dual-band transmission line consists of coupled lines with open-ended stub. Using this new transmission line, the dual-band branch-line coupler features a wide range of frequency ratios and a flexible structure. To verify the design concept, a dual-band branch-line coupler working at 2/5.2 GHz is designed and fabricated. Good agreement has been achieved between the measured and simulated results. In addition, it is worth to mention that the proposed dual-band transmission line can be also applied to design other dual-band microwave components such as Wilkinson power dividers, rat-race couplers, and baluns which are important in beam-forming system.

CHAPTER 4

A NOVEL DESIGN OF MULTI-BAND BRANCH-LINE COUPLER USING MULTI-BAND TRANSMISSION LINES *

4.1 Introduction

Modern beam-forming systems have imposed new design requirements such as compact size, low cost and multi-band operation. Among these characteristics, the multi-band operation can result in reductions in both the size and cost of the whole system. Therefore, it is attractive to design multi-band microwave circuits and components. Up to now, a lot of works have been reported on dual-band microwave components. Meanwhile, coupler is one of the fundamental passive components in beam-forming systems. Recently, some researches of dual-band couplers have been published. However, only a few works have been reported for tri-band couplers [36]-[37]. In [36], a tri-band coupler is realized by using compensation technique to match the pass-band region. Another design of tri-band coupler employs matching circuits at each port of the conventional coupler [37].

A novel coupler using multi-band transmission lines is designed, which can operate at three different frequencies. To support the multi-band operation, a novel multi-band transmission line is designed to replace each section of the conventional branch-line coupler. Fig. 4.1 shows the general configuration of the proposed multi-band coupler. From Fig. 4.1, the proposed multi-band transmission line consists of Pi-type line with open- and short-ended stubs. The original Pi-type line is employed to achieve dual-band operation at f_2/f_1, and the operation at the third frequency f_3 is realized by tapping open-

* This chapter is reproduced from Han, R, Shao, J, Zhou, M., Arigong, B., Ding, J., and Zhang, H. (2014). Novel Design of Multi-Band Branch-Line Coupler Using Multi-Band Transmission Lines. Microwave and Optical Technology Letters, vol. 56, pp. 2841-2845, with permission from Wiley-Blackwell.

and short-ended stubs at the center of the Pi-type line. The explicit design equations are derived for each constituting components of the proposed coupler. For the purpose of experimental demonstration, a multi-band coupler operating at 1/2.5/4.5 GHz is designed and tested. Finally, it is found that both simulation and measurement results can match well with the proposed design theory.

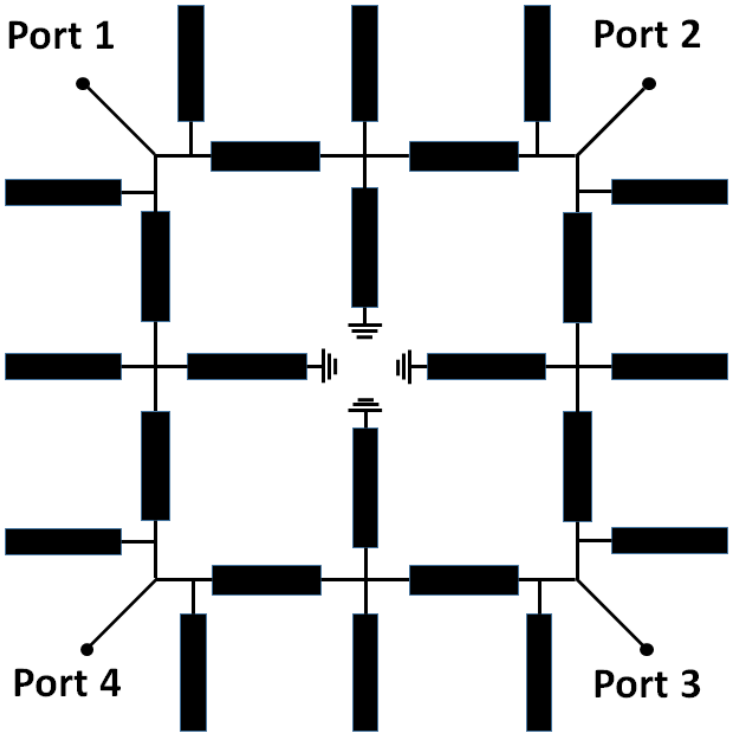

Figure 4.1: General configuration of the proposed multi-band coupler using multi-band transmission lines.

4.2 Design and Analysis

To realize multi-band operation, a novel multi-band transmission line is employed in the proposed design to replace each single-band transmission line section of the conventional branch-line coupler. Fig. 4.2 depicts the structure of the proposed multi-band transmission line. In Fig. 4.2, the black-colored transmission line sections constitute the Pi-type line, which consists of two series sections and two shunt sections. In the

proposed design, the Pi-type line is used to achieve dual-band operation at two frequencies f_2/f_1. The other two sections marked with shaded lines are open- and short-ended stubs. By tapping these two stubs at the center of the Pi-type line, the operation at the third frequency f_3 is realized. Meanwhile, these two tubs do not cause any interference to the first two operating frequencies f_2/f_1. Therefore, combining the Pi-type line with open- and short-ended stubs, the tri-band operation can be achieved. To obtain the values of design parameters, the details of design procedure are presented as follows.

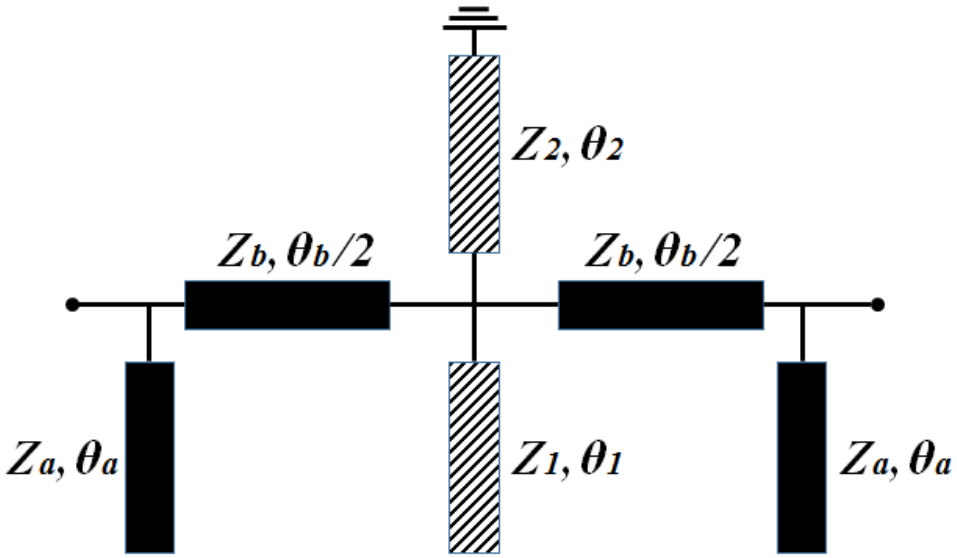

Figure 4.2: Structure of the proposed tri-band transmission line (Note: solid-filling sections represent the Pi-type line; others with shaded lines are open- and short-ended stubs).

For the dual-band operation at f_2/f_1, the values of Z_a, θ_a, Z_b, and θ_b within the Pi-type line can be obtained. As shown in Fig. 4.2, Z_a and Z_b are the characteristic impedances of transmission lines in the Pi-type line, and θ_a and θ_b are the electrical lengths of them at the first frequency f_1. The *ABCD*-matrix of Pi-type line is employed to simplify the analysis, and the formulas of each parameter can be derived as the following:

$$A_{Pi} = D_{Pi} = \frac{Z_a \cos\theta_b - Z_b \tan\theta_a \sin\theta_b}{Z_a} \tag{4.1}$$

$$B_{Pi} = jZ_b \sin\theta_b \tag{4.2}$$

$$C_{Pi} = \frac{j2\tan\theta_a \cos\theta_b}{Z_a} + \frac{j\sin\theta_b}{Z_b} - \frac{jZ_b \tan^2\theta_a \sin\theta_b}{{Z_a}^2} \tag{4.3}$$

From Eqn. 4.1 - 4.3, it is found that replacing θ_a and θ_b with $n_a\pi$ - θ_a and $2n_b\pi$ - θ_b (n_a and n_b are integers) can make A_{Pi} and B_{Pi} remain the same magnitude. This is the key to realize the dual-band operation with the Pi-type line. In the proposed design, the electrical lengths of these sections are "θ_a and θ_b" and "$n_a\pi$ - θ_a and $2n_b\pi$ - θ_b" at f_1 and f_2 respectively:

$$\text{For } f_1, \quad \begin{cases} \theta_a \\ \theta_b \end{cases} \tag{4.4}$$

$$\text{For } f_2, \quad \begin{cases} n_a\pi - \theta_a \\ 2n_b\pi - \theta_b \end{cases} \tag{4.5}$$

where f_1 is the lower working frequency, and f_2 is the higher working frequency, n_a, n_b = 1, 2, 3, …. Based on (4) and (5), the design formula of the electrical lengths θ_a and θ_b can be obtained as:

$$\theta_a = \frac{n_a\pi}{R_1 + 1} \quad @f_1 \tag{4.6}$$

$$\theta_b = \frac{2n_b\pi}{R_1 + 1} \quad @f_1 \tag{4.7}$$

where $R_1 = f_2/f_1$. To realize dual-band operation with characteristic impedance Z_0 and electrical length θ_0, the conditions $A_{Pi} = A_0$ and $B_{Pi} = B_0$ (A_0 and B_0 are *ABCD*-matrix parameters of the conventional transmission line with an impedance of Z_0 and an electrical length of θ_0, $A_0 = \cos\theta_0$ and $B_0 = jZ_0 \sin\theta_0$) need to be satisfied. Finally, the values of Z_a and Z_b can be calculated as:

$$Z_a = \frac{Z_0 \sin\theta_0 \tan\theta_a}{\cos\theta_b - \cos\theta_0} \tag{4.8}$$

$$Z_b = \frac{Z_0 \sin\theta_0}{\sin\theta_b} \tag{4.9}$$

For a dual-band 50 Ω quarter-wavelength transmission line realized by the Pi-type line, the range of the realizable frequency ratio is 1.3 < R_1 < 2.5, as shown in Fig. 4.3 (Assuming that the impedance is normalized to 50 Ω and the available normalized impedance is between 0.4 and 2.6 for conventional microstrip lines).

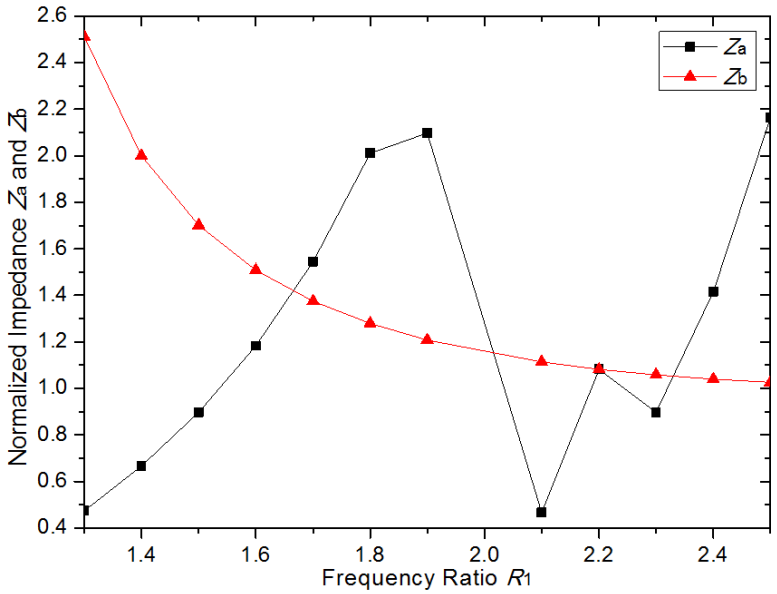

Figure 4.3: Normalized impedance Z_a and Z_b versus the first frequency ratio R_1 ($R_1 = f_2/f_1$).

After realizing the dual-band operation at f_2/f_1, the third operating frequency f_3 is considered. In the proposed design, additional open- and short-ended stubs are tapped at the center of the Pi-type line to form a new transmission line (as showing Fig. 4.2). This new transmission line will be equivalent to a transmission line with a characteristic impedance of Z_0 and an electrical length of θ_0 at the third working frequency f_3. Meanwhile, the open- and short-ended stubs cannot disturb the performance of the original Pi-type line at f_2/f_1. Once these two conditions are satisfied, the desired tri-band operation can be achieved. To satisfy the second condition, the total impedance (shunted) of these open-

and short-ended stubs (with impedances of Z_1 and Z_2) should be infinity at f_1 and f_2. Based on this theory, the following equations are derived:

$$Z_1 = \tan\theta_1 \tan\theta_2 \, Z_2 \tag{4.10}$$

$$\theta_1 = \frac{n_1\pi}{R_1-1} \ @f_1, \theta_2 = \frac{n_2\pi}{R_1-1} \ @f_1 \text{ or } \theta_1 = \frac{n_1\pi}{R_1+1} \ @f_1, \theta_2 = \frac{n_2\pi}{R_1+1} \ @f_1 \tag{4.11}$$

where Z_1, θ_1, Z_2, θ_2 (θ_1, θ_2 are evaluated at f_1) are characteristic impedance and electrical length of open- and short-ended stubs respectively, and n_1, n_2 are integers. To find the relationship between f_3 and f_2/f_1, the overall *ABCD*-matrix of the proposed multi-band transmission line is considered (Based on the symmetrical structure of the multi-band transmission line, only parameters *A* and *B* are needed):

$$A = \cos R_2\theta_b - \frac{Z_b \sin R_2\theta_b \, (Z_2 \tan R_2\theta_1 \tan R_2\theta_2 - Z_1)}{2Z_1Z_2 \tan R_2\theta_2} - \frac{\tan R_2\theta_a}{Z_a} B \tag{4.12}$$

$$B = -\frac{jZ_b{}^2(1 - cos\, R_2\theta_b)(Z_2\, tan\, R_2\theta_1\, tan\, R_2\theta_2 - Z_1)}{2Z_1Z_2\, tan\, R_2\theta_2} + jZ_b\, sin\, R_2\theta_b \tag{4.13}$$

where $R_2 = f_3/f_1$, and the values of θ_a, θ_b, Z_a, Z_b can be obtained from Eqn. 4.6 - 4.9. Substituted Eqn. 4.10 into $A = A_0$ and $B = B_0$ (again A_0 and B_0 are parameters in the *ABCD*-matrix of the conventional transmission line with a characteristic impedance of Z_0 and an electrical length of θ_0, $A_0 = \cos\theta_0$ and $B_0 = jZ_0 \sin\theta_0$), the following design equation can be derived:

$$(1 - cos\, R_2\theta_b)[tan\, \theta_a\, (cos\, R_2\theta_b - cos\, \theta_0) - tan\, R_2\theta_a\, (cos\, \theta_b - cos\, \theta_0)]$$

$$= tan\, \theta_a\, sin\, R_2\theta_b\, (sin\, R_2\theta_b - sin\, \theta_b) \tag{4.14}$$

From Eqn. 4.14, the value of R_2 can be obtained once θ_a and θ_b are known. Since the values of θ_a and θ_b are calculated from Eqn. 4.6 and 4.7, the relationship between R_1 and R_2 can be calculated as shown in Fig. 4.4. Finally, the design formula for Z_2 is derived as the following:

$$Z_2 = \frac{{Z_b}^2(tan\, R_2\theta_1\, tan\, R_2\theta_2 - tan\, \theta_1\, tan\, \theta_2)(1 - cos\, R_2\theta_b)}{tan\, \theta_1\, tan\, \theta_2\, tan\, R_2\theta_2\, (2Z_b\, sin\, R_2\theta_b - Z_0\, sin\, \theta_0)} \quad (4.15)$$

Fig. 4.5 exhibits the normalized Z_1 and Z_2 is realizable within the range of the first frequency ratio R_1. In summary, to design the proposed multi-band transmission line, the design procedures are given as the following:

1) Select R_1 and obtain the values of θ_a, θ_b, Z_a and Z_b from Eqn. 4.6 – 4.9;
2) Use the values of θ_a and θ_b to get the corresponding R_2 by Eqn. 4.14;
3) Choose values of θ_1, θ_2 from Eqn. 4.11 and obtain the value of Z_2 by Eqn. 4.15;
4) Use Eqn. 4.10 to determine the value Z_1.

4.3 Simulation and Measurement Results

To verify the proposed design theory, a multi-band branch-line coupler using multi-band transmission lines is designed to operate at 1/2.5/4.5 GHz (f_1=2.5 GHz, f_2=4.5 GHz, and f_3=1 GHz). Following the design procedures mentioned in the previous section, the values of parameters for each branch line are calculated. For the branch of 50 Ω quarter-wavelength line, $\theta_a = \theta_b = \theta_1 = \theta_2 = 128.57°$, Z_a = 100.56 Ω, Z_b = 63.95 Ω, Z_1 = 90.51 Ω, Z_2 = 57.56 Ω. For the branch of 35.35 Ω quarter-wavelength line, $\theta_a = \theta_b = \theta_1 = \theta_2 = 128.57°$, Z_a = 71.11 Ω, Z_b = 45.22 Ω, Z_1 = 78.62 Ω, Z_2 = 128.57 Ω. The proposed design is simulated by using the full-wave simulator HyperLynx. For the measurement, the designed coupler is fabricated on RT/Duroid 5880 substrate with the substrate thickness of 0.787 mm and the dielectric constant of 2.2. Fig. 4.6 presents the photograph of the fabricated multi-band branch-line coupler with the size of 9.82 cm × 9.76 cm. Figs. 4.7 – 4.9 show the simulated and measured results of the proposed multi-band branch-line coupler. At the

three operating frequencies 1/2.5/4.5 GHz, the insertion loss S_{21} is equal to -3.06/-3.64/-3.42 dB respectively, while the insertion loss S_{31} is -3.01/-3.42/-3.89 dB respectively (as shown in Fig. 4.7). The amplitude imbalance ($|S_{31}| - |S_{21}|$) is less than 0.5 dB at the design frequencies. For the return loss (as shown in Fig. 4.8), both simulation and measurement results are below -16 dB at operating frequencies, while the isolation is less than -20 dB (also shown in Fig. 4.8). Fig. 4.9 presents the simulated and measured results of the phase difference ($\angle S_{31} - \angle S_{21}$). At 1/2.5/4.5 GHz, the measured phase difference is -89.15°, -92.74°, and 89.65° respectively. All these results have clearly verified the multi-band responses of the designed branch-line coupler.

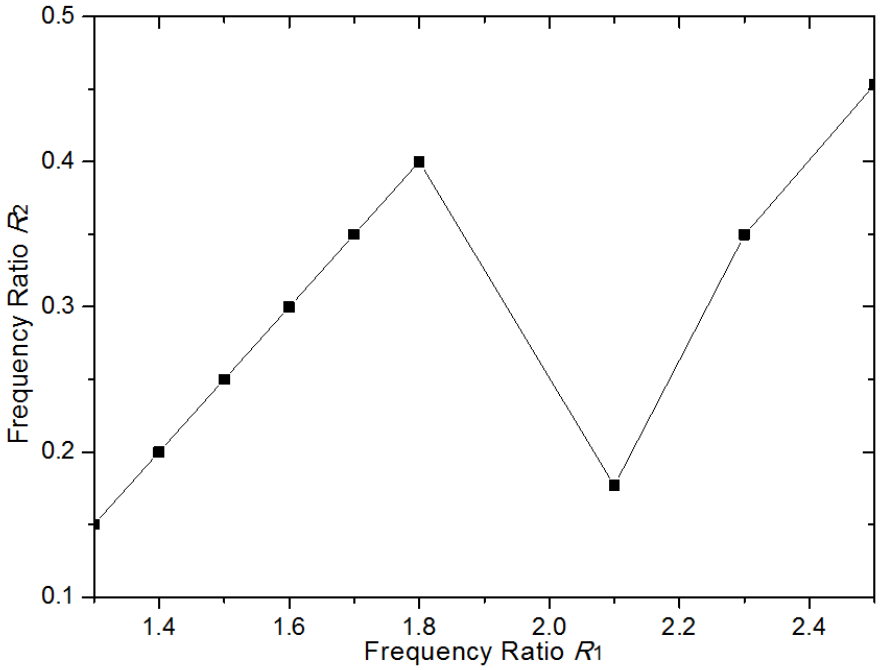

Figure 4.4: The relationship between R_1 and R_2 ($R_1 = f_2/f_1$, $R_2 = f_3/f_1$).

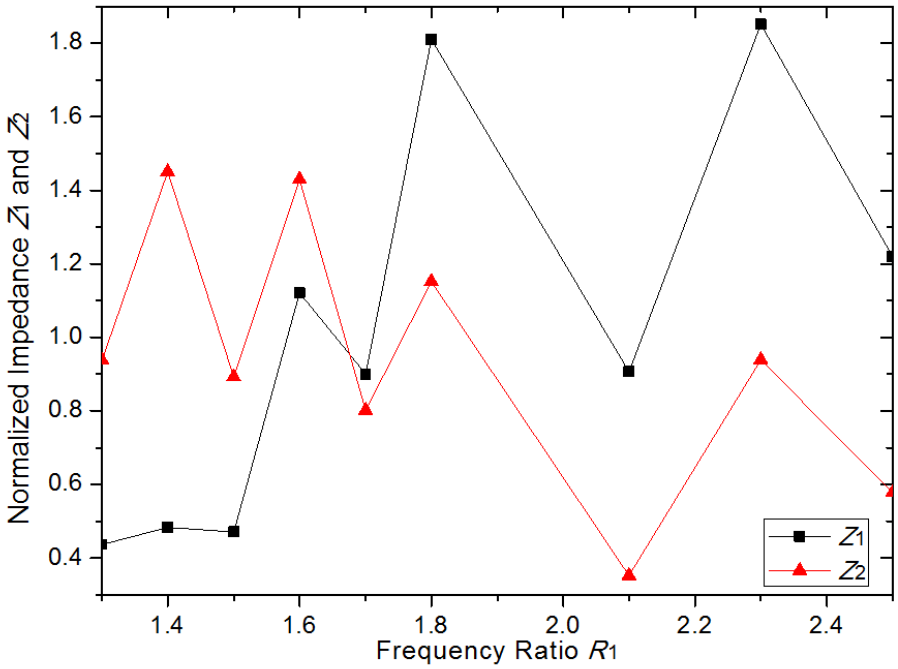

Figure 4.5: Variation of the normalized Z_1 and Z_2 versus the first frequency ratio $R_1 = f_2/f_1$.

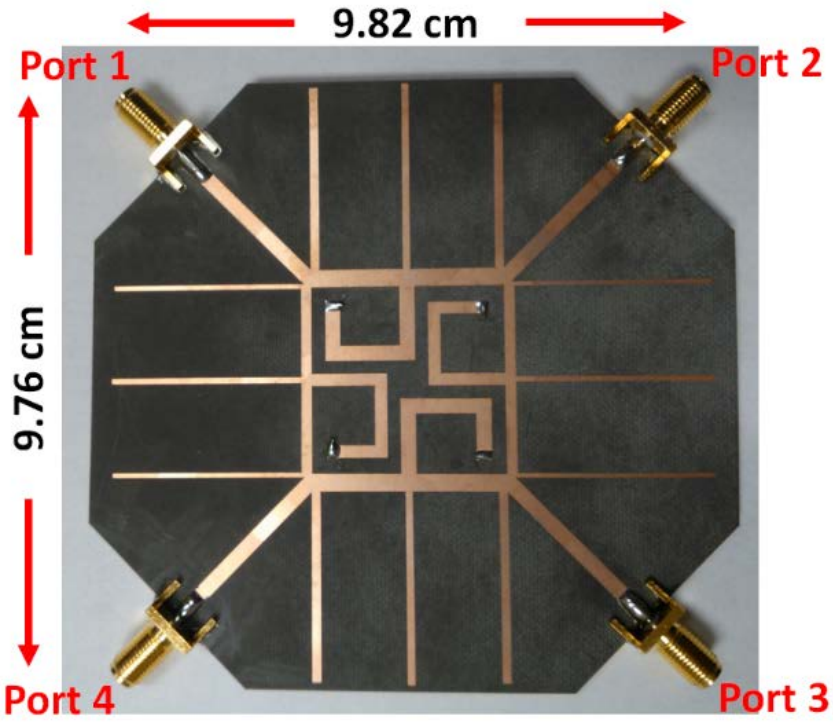

Figure 4.6: Photograph of the fabricated tri-band branch-line coupler.

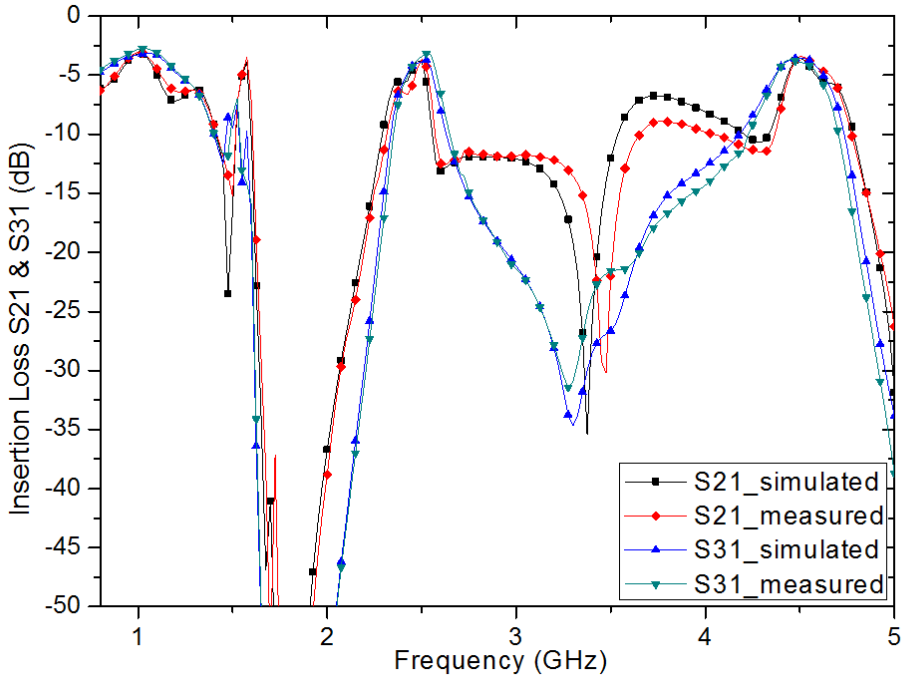

Figure 4.7: Simulated and measured results of insertion loss.

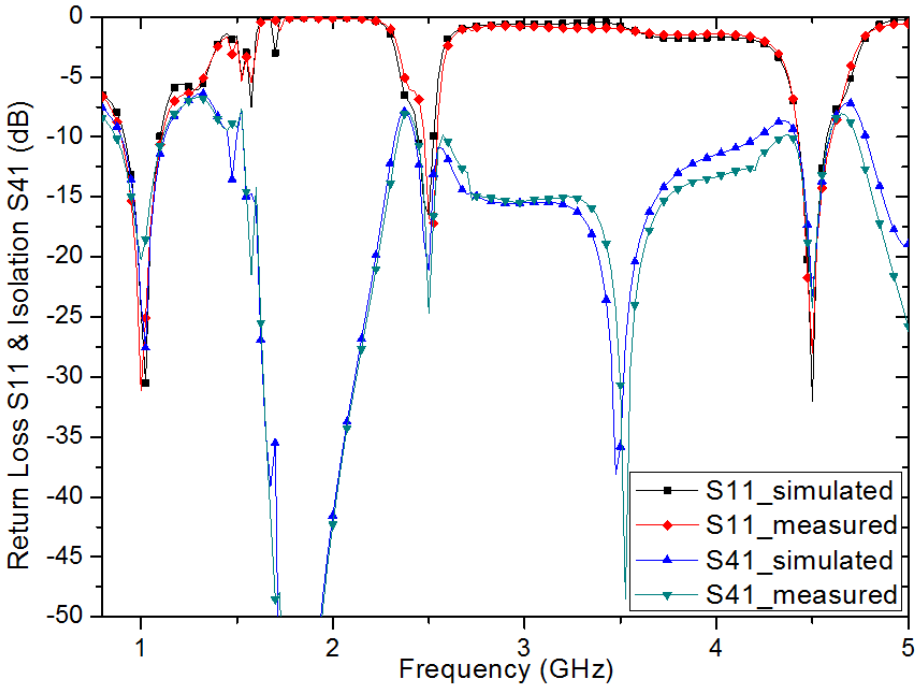

Figure 4.8: Simulated and measured results of return loss and isolation.

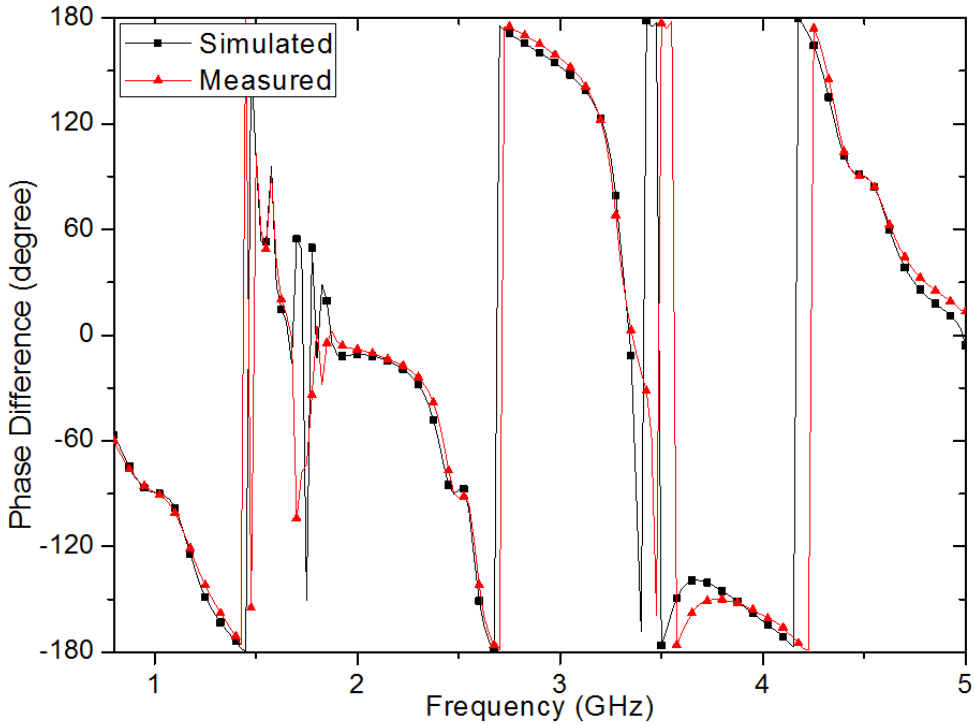

Figure 4.9: Simulated and measured results of phase response.

4.4 Conclusion

A novel design of multi-band branch-line coupler is realized by using a multi-band transmission line to replace each single-band section of the conventional branch-line coupler. The proposed multi-band transmission line consists of Pi-type line with open- and short-ended stubs. The Pi-type line supports the dual-band operation at first two working frequencies, while the open- and short-ended stubs are tapped at the center of the Pi-type line to realize the operation at the third working frequency. To prove the design concept, a multi-band branch-line coupler operating at 1/2.5/4.5 GHz is designed and tested. Both the simulated and measured results have verified the design theory.

CHAPTER 5

A NOVEL DESIGN OF 4×4 BUTLER MATRIX WITH RELATIVELY FLEXIBLE PHASE DIFFERENCES †

5.1 Introduction

Beam-forming antenna array has made a rapid development in civil and military sectors. For example, it can be applied for applications such as human-machine interfaces, search and rescue, remote sensing, imaging, and respiration measurement. The function of beam-forming antenna array is to provide the specific magnitude and phase responses to realize different angles of scanning beams. One common way to construct the beam-forming antenna array is to apply the Butler matrix [38]-[39]. The conventional Butler matrix featuring a symmetrical structure is composed of couplers, crossovers, and phase shifters. For example, the conventional 4×4 Butler matrix has four input and output ports, which consists of four 3 dB hybrid couplers, two 45° phase shifters, two crossovers (as shown in Fig. 2.6). By exciting one of the input ports, the equal-amplitude and progressive-phase-distribution responses (i.e. phase differences are ±45° and ±135°) can be generated at the output ports [40]. By connecting the 4×4 Butler matrix with an antenna array, there will be four distinct beams in the radiation pattern. Up to now, the design of Butler matrix has been focused on band engineering and size reduction. For example, the dual-band Butler matrix can be realized by using a modified structure [41]. In [42], it is reported that a Butler matrix using 180° hybrids instead of 90° couplers can achieve a broad bandwidth. By applying -45° phase difference coupler, compact

† This chapter is reproduced from Ren, H, Arigong, B, Shao, J, Zhou, M, Ding, J, Zhang, H. (2016). A Novel Design of 4Ã4 Butler Matrix with Flexible Phase Differences. IEEE Microwave and Wireless Components Letters, vol. 15, pp. 1277-1280, with permission from IEEE.

Butler matrix can be achieved without phase shifters [43]. A wideband Butler matrix for UWB band is realized by applying multilayer structures [44]. In [45], a broadband 8×8 Butler matrix is integrated with one isolator to measure S-parameters of two-port device. In order to further improve the performance of Butler matrix, it is meaningful to design un-conventional Butler matrix with arbitrary progressive phase difference. In [46], a modified Butler matrix is designed consisting of 90° and 180° hybrids. Due to the limitation of the 180° hybrid layout, it can only be realized by using multilayer structures, which increase the complexity and cost of the whole system and is not convenient for practical implementation.

A novel topology of 4×4 Butler matrix with relatively flexible progressive phase differences is presented. To realize the design goal, couplers with arbitrary phase-difference are engineered and allocated within the new Butler matrix [47]-[48]. The typical characteristics of the proposed design are summarized as follows. First, compared to the phase differences (±45° and ±135°) generated by the conventional 4×4 Butler matrix, the proposed design can generate different sets of phase differences, which can be realized from -180° to +180°. This feature can increase the options of feeding modes for antenna array, extending the range of the radiation beam angles. Second, the topology of the proposed Butler matrix is always symmetrical while the progressive phase difference varies in the full range. The resulting symmetrical Butler matrix will help to minimize the imbalance on amplitude and phase. Third, the proposed novel Butler matrix employs a single-layer structure, providing a low cost and convenient implementation. Finally, the closed-form design equations are derived and presented, which streamline the design process of the proposed Butler matrix.

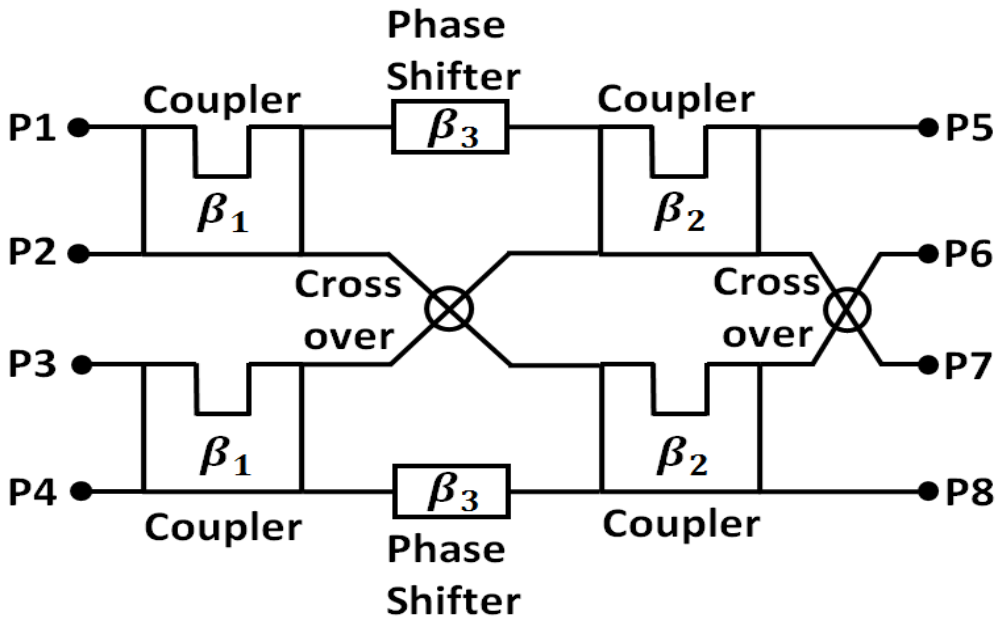

Figure 5.1: Configuration of the proposed 4×4 Butler matrix with arbitrary phase-difference couplers, phase shifters, and crossovers (P1 - P4 are input ports, and P5 - P8 are output ports).

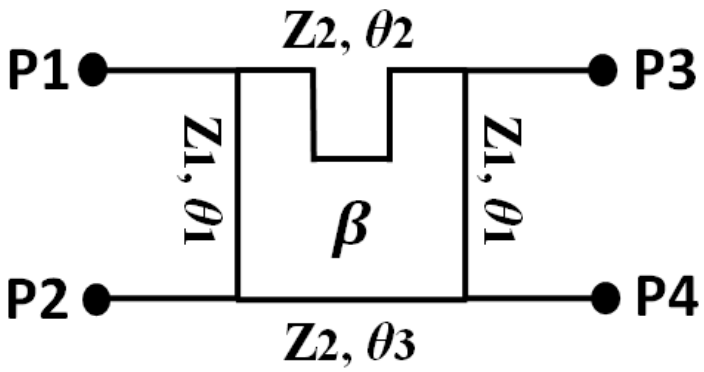

Figure 5.2: Configuration of the arbitrary phase-difference coupler applied in the proposed 4×4 Butler matrix (P1 - P2 are input ports, and P3 - P4 are output ports).

5.2 Design and Theory

To achieve the design goal of a generalized Butler matrix with flexible progressive phase difference at the output ports, a new topology of the 4×4 Butler matrix is proposed as shown in Fig. 5.1. There are four input ports P1-P4 and four output ports P5-P8. It is consisted of two couplers with phase-difference β_1, two couplers with phase-difference β_2, two phase shifters with phase-difference β_3, and two crossovers. Fig. 5.2 shows the

diagram of the coupler used in the proposed Butler matrix. The proposed coupler consists of four branch lines with characteristic impedances Z_1, Z_2 and electrical lengths θ_1, θ_2, θ_3. The phase responses of the couplers are summarized as follows:

$$\angle(S_{41}) - \angle(S_{31}) = \beta \tag{5.1}$$

$$\angle(S_{42}) - \angle(S_{32}) = \pi + \beta \tag{5.2}$$

$$\angle(S_{31}) - \angle(S_{42}) = -\pi - 2\beta \tag{5.3}$$

where the range of phase-difference β is from 0 to –π. From Eqn. 5.1 and 5.2, exciting one of the two input ports (P1 or P2 shown in Fig. 5.2) generates a unique phase difference between output ports. The difference between two unique phase differences is always equal to ±π. Based on the layout of the proposed Butler matrix (as shown in Fig. 5.1), the final phase response between the input and output ports are listed in Table 5.1.

Table 5.1

The Phase response of the proposed Butler matrix

Port	P1	P2	P3	P4
P5	α	$\alpha+\beta_1$	$\alpha+\beta_2-\beta_3$	$\alpha+\beta_1+\beta_2-\beta_3$
P6	$\alpha+\beta_1-\beta_3$	$\alpha+2\beta_1-\beta_3+\pi$	$\alpha+\beta_1+\beta_2$	$\alpha+2\beta_1+\beta_2+\pi$
P7	$\alpha+\beta_2$	$\alpha+\beta_1+\beta_2$	$\alpha+2\beta_2-\beta_3+\pi$	$\alpha+\beta_1+2\beta_2-\beta_3+\pi$
P8	$\alpha+\beta_1+\beta_2-\beta_3$	$\alpha+2\beta_1+\beta_2-\beta_3+\pi$	$\alpha+\beta_1+2\beta_2+\pi$	$\alpha+2\beta_1+2\beta_2+2\pi$

In order to facilitate the comparison, we have set the phase response between P1 and P5 as α. From Table 5.1, the progressive phase difference $\Delta\theta$ among the output ports when the signal is input from different input ports can be obtained as:

For P1: $\Delta\theta_1 = \beta_1 - \beta_3 = -\beta_1 + \beta_2 + \beta_3 + 2n_1\pi$ (5.4)

For P2: $\Delta\theta_2 = \beta_1 - \beta_3 + \pi = -\beta_1 + \beta_2 + \beta_3 - \pi + 2n_2\pi$ (5.5)

For P3: $\Delta\theta_3 = \beta_1 + \beta_3 = -\beta_1 + \beta_2 - \beta_3 + \pi + 2n_3\pi$ (5.6)

For P4: $\Delta\theta_4 = \beta_1 + \beta_3 + \pi = -\beta_1 + \beta_2 - \beta_3 + 2n_4\pi$ (5.7)

where $n_1, n_2, n_3, \text{and } n_4$ are integers. From Eqn. 5.4 – 5.7, two important design formulas can be derived as:

$$\beta_1 = \frac{2\beta_2 + \pi + 2(n_1 + n_3)\pi}{4} \tag{5.8}$$

$$\beta_3 = \frac{\pi - 2(n_1 - n_3)\pi}{4} \tag{5.9}$$

Based on the range of β_1 and β_2 (from 0 to -π), the sum of $n_1 + n_3$ should be between $-\frac{\beta_2}{\pi} - 2.5$ and $-\frac{\beta_2}{\pi} - 0.5$. To realize unique progressive phase differences at output ports, the condition of $\Delta\theta_1 \neq \Delta\theta_2 \neq \Delta\theta_3 \neq \Delta\theta_4$ must be satisfied. Within the valid range of $n_1 + n_3$, we can manage to obtain four unique phase differences of the designed Butler matrix. For easy implementation, we set $n_1 = 0$ and $n_3 = -1$, yielding

$$\beta_1 = \frac{\beta_2}{2} - \frac{\pi}{4}, \qquad \beta_3 = -\frac{\pi}{4} \tag{5.10}$$

Substituting Eqn. 5.10 into Eqn. 5.4 – 5.7, the final formulas for the Butler matrix's phase differences can be derived as:

$$\Delta\theta_1 = \frac{\beta_2}{2} \tag{5.11}$$

$$\Delta\theta_2 = \frac{\beta_2}{2} + \pi \tag{5.12}$$

$$\Delta\theta_3 = \frac{\beta_2 - \pi}{2} \tag{5.13}$$

$$\Delta\theta_4 = \frac{\beta_2 + \pi}{2} \tag{5.14}$$

From Eqn. 5.11 – 5.14, the progressive phase differences generated by the proposed Butler matrix depend on the couplers with arbitrary phase-difference β_2. It is clear that using different phase-difference of the couplers can lead to different progressive phase differences in the 4×4 Butler matrix. Table 5.2 provides two groups of generated

progressive phase differences based on two different sets of β_1 and β_2. Therefore, based on the range of β_2, the proposed 4×4 Butler matrix can provide a wide range of phase differences (from -180° to +180°). Integrating the proposed symmetrical Butler matrix with an antenna array (e.g. half-wavelength distance between adjacent antennas), asymmetrical patterns can be generated, and the available range of radiation beam angles can be extended from -90° and +90°. In this way, the beam-forming antenna array's performance can be significantly improved.

Table 5.2

Phase differences of Butler matrix and corresponding couplers' phase differences

$\boldsymbol{\beta_2}$	-60°	-30°
$\boldsymbol{\beta_1}$	-75°	-60°
$\boldsymbol{\Delta\theta_1}$	-30°	-15°
$\boldsymbol{\Delta\theta_2}$	+150°	+165°
$\boldsymbol{\Delta\theta_3}$	-120°	-105°
$\boldsymbol{\Delta\theta_4}$	+60°	+75°

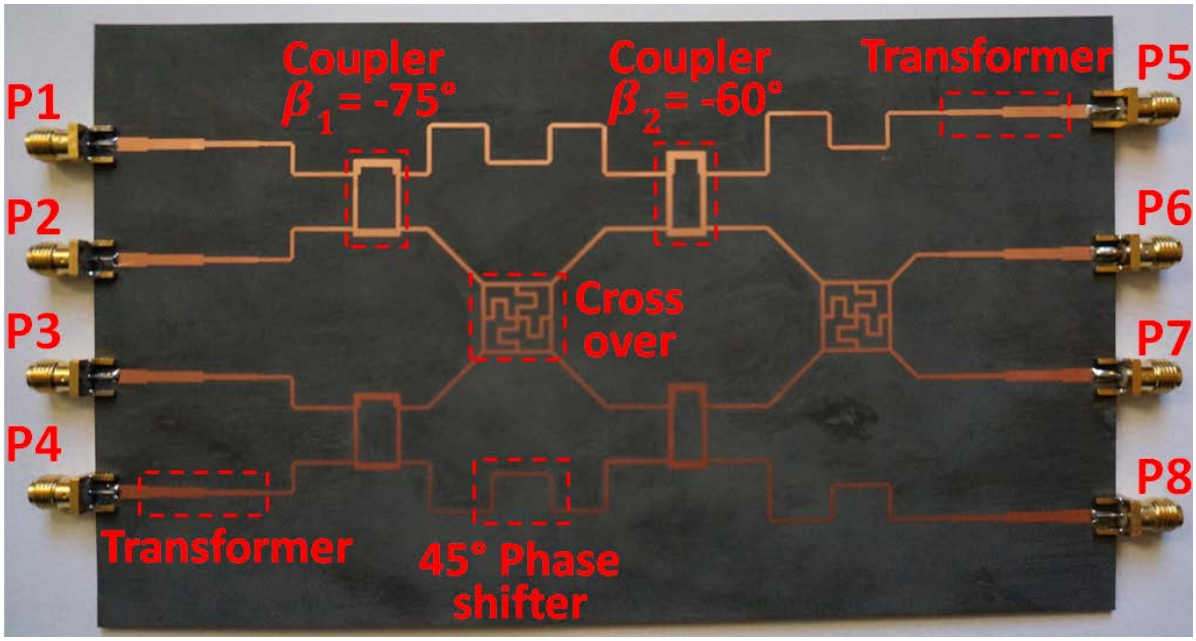

Figure 5.3: Photograph of the fabricated 4×4 Butler matrix.

5.3 Simulation and Measurement Results

To verify the design concept, a Butler matrix with phase differences -30°, +150°, -120°, and +60° (as shown in column 2 of Table 5.2) is designed to operate at 5.8 GHz. This Butler matrix employs two -60° phase-difference couplers and two -75° phase-difference couplers. For the -60° phase-difference coupler, the normalized characteristic impedances are set as Z_1 = 0.866, Z_2 = 0.654, while the electrical lengths are set as θ_1 = 90°, θ_2 = 110.7°, θ_3 = 69.29° (the diagram is shown in Fig. 5.2). For the -75° coupler, the normalized characteristic impedances are set as Z_1 = 0.966, Z_2 = 0.694, while the electrical lengths are set as θ_1 = 90°, θ_2 = 100.54°, θ_3 = 79.45°. Fig. 5.3 shows the photograph of the fabricated Butler matrix on RT/Duroid 5880 substrate with the substrate thickness of 0.787 mm and the dielectric constant of 2.2. The dimension of the Butler matrix is about 182.82 mm × 75.19 mm. In the proposed design, since the width of the 50 Ω microstrip line is too wide to effectively implement the design, the system impedance is chose to be 100 Ω and several additional transformers are applied to match the 100 Ω system impedance with 50 Ω input/output ports. The simulated and measured magnitude responses for different input ports are given in Fig. 5.4 – 5.7.

From the simulation results, the amplitude imbalance of output signals when input from different input ports is less than 0.45 dB at 5.8 GHz. Both return loss and isolation are better than 17 dB at the design frequency. In the measurement, the working frequency is shifted to 5.99 GHz, which is mainly caused by the fabrication tolerance. When P1 is excited, the measured magnitude responses are S_{51}= -6.88 dB, S_{61}= -7.03 dB, S_{71}= -7.56 dB, S_{81}= -7.51 dB. When P2 is excited, the measured magnitude responses are S_{52}= -7.52 dB, S_{62}= -6.83 dB, S_{72}= -7.40 dB, S_{82}= -7.37 dB. For P3 excitation, the measurement

results are S_{53}= -7.30 dB, S_{63}= -7.41 dB, S_{73}= -6.76 dB, S_{83}= -7.05 dB. For P4 excitation, the measurement results are S_{54}= -7.51 dB, S_{64}= -7.52 dB, S_{74}= -6.83 dB, S_{84}= -6.77 dB. For all input ports, the maximum amplitude imbalance of output signals is about 0.75 dB at 5.99 GHz. The measured 3 dB bandwidth of the designed Butler matrix is about 11%. At the operating frequency, the measured return loss is better than 16 dB, and the isolation is better than 18 dB (the bandwidth with 10 dB return loss is about 15%). Fig. 5.8 – 5.11 show the simulated and measured phase responses of the Butler matrix. According to the simulation, the phase difference at 5.8 GHz is about -30°±3° for input port P1, +150°±4° for input port P2, -120°±3° for input port P3, and +60°±4° for input port P4. Correspondingly, the measured phase differences at 5.99 GHz are -30°±4°, +150°±6°, -120°±6°, and +60°±3° for different input ports. For all input ports, the maximum phase difference mismatch is about ±6°. To improve the stability of phase difference, broadband components (such as phase shifters, couplers, and crossovers) can be applied to realize a broadband Butler matrix. Overall, it is observed that the simulation and measurement results of the proposed 4×4 Butler matrix are in good agreement, verifying the design concept.

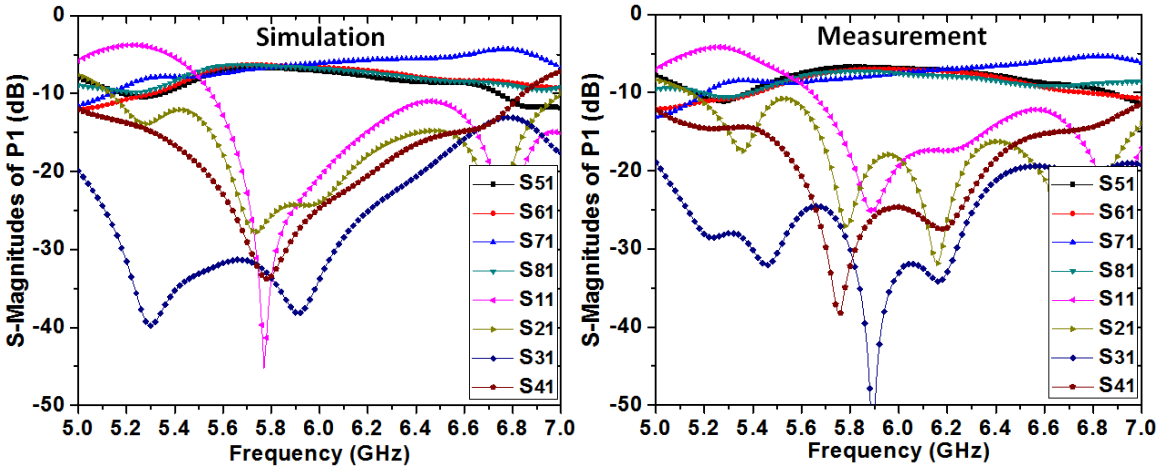

(a) (b)

Figure 5.4: (a) Simulated and (b) measured magnitude responses for input port P1.

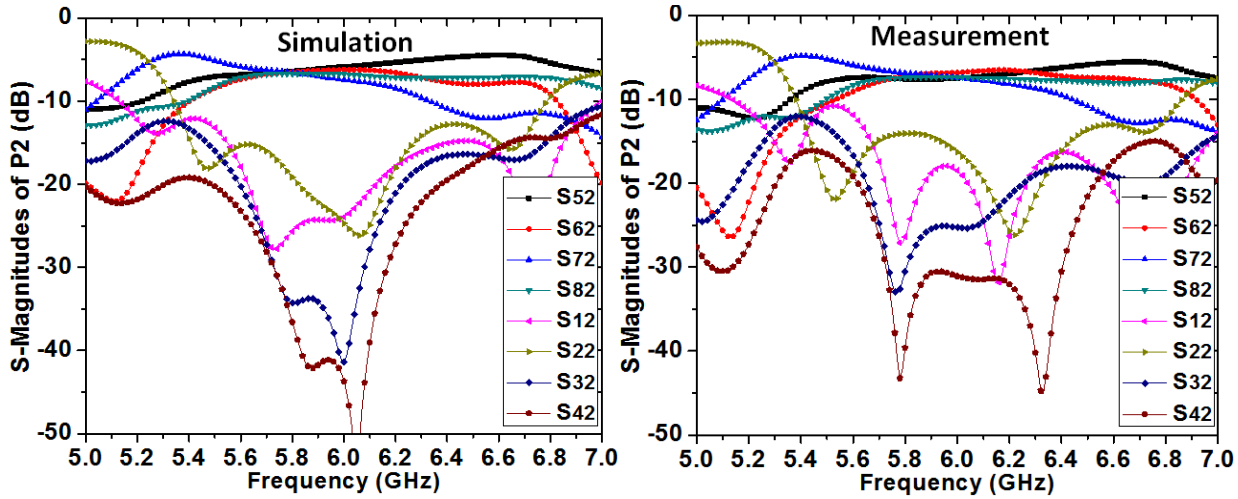

(a) (b)

Figure 5.5: (a) Simulated and (b) measured magnitude responses for input port P2.

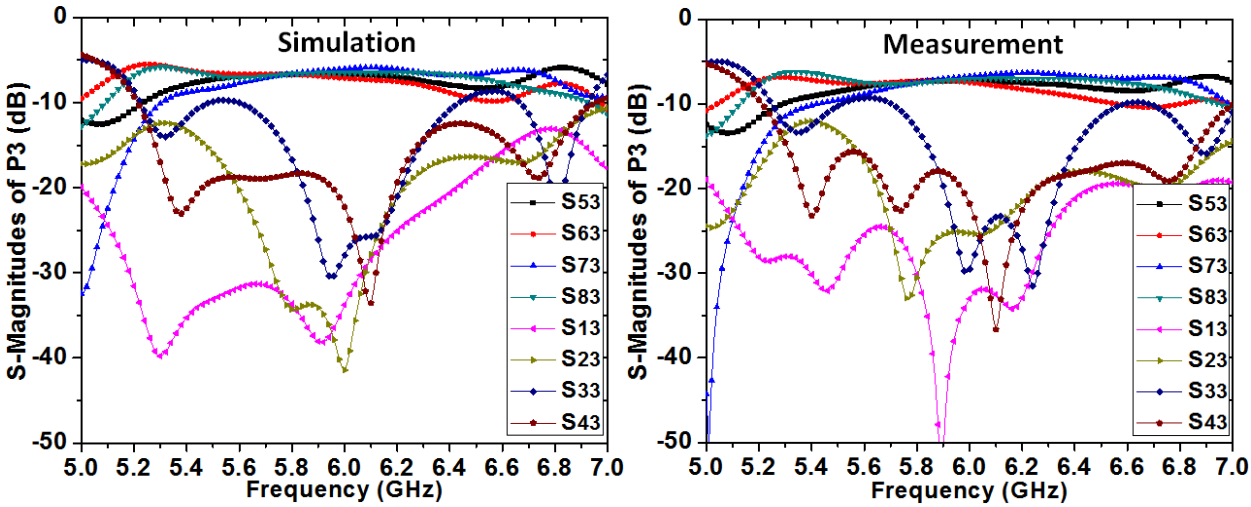

(a) (b)

Figure 5.6: (a) Simulated and (b) measured magnitude responses for input port P3.

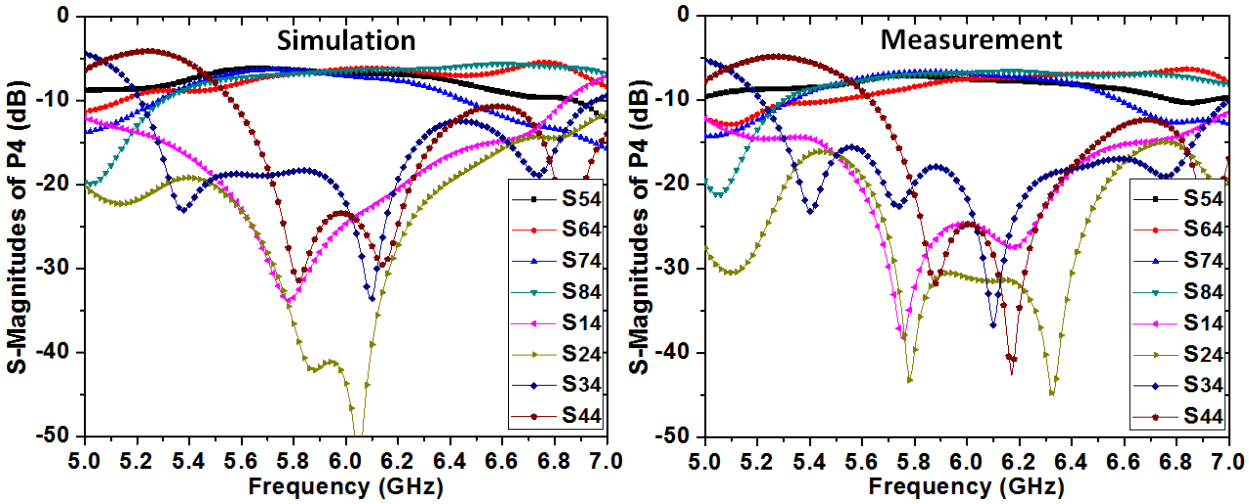

(a) (b)

Figure 5.7: (a) Simulated and (b) measured magnitude responses for input port P4.

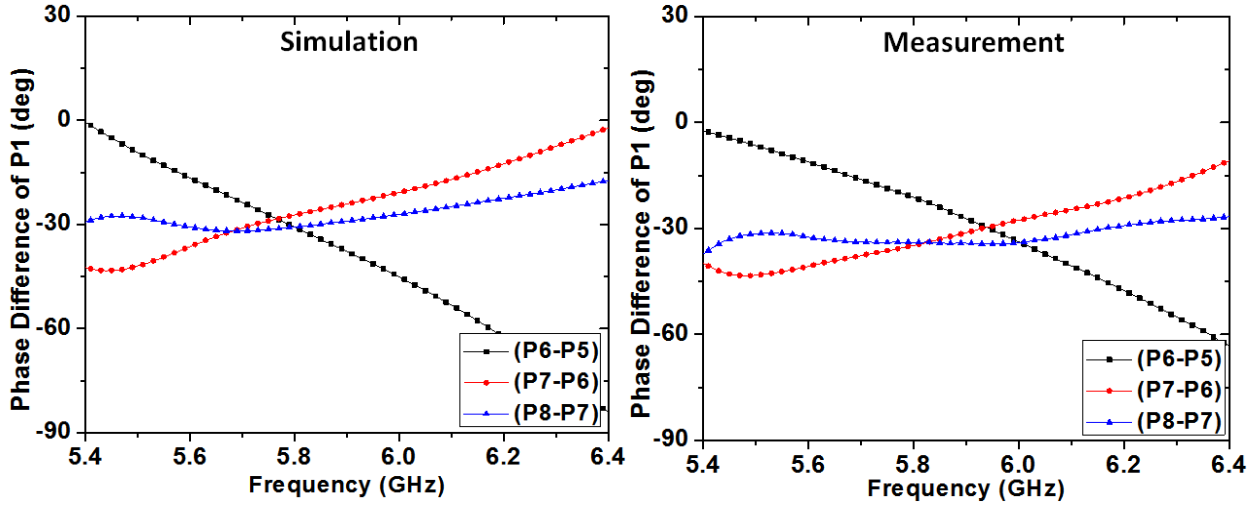

(a) (b)

Figure 5.8: (a) Simulated and (b) measured phase difference for input port P1.

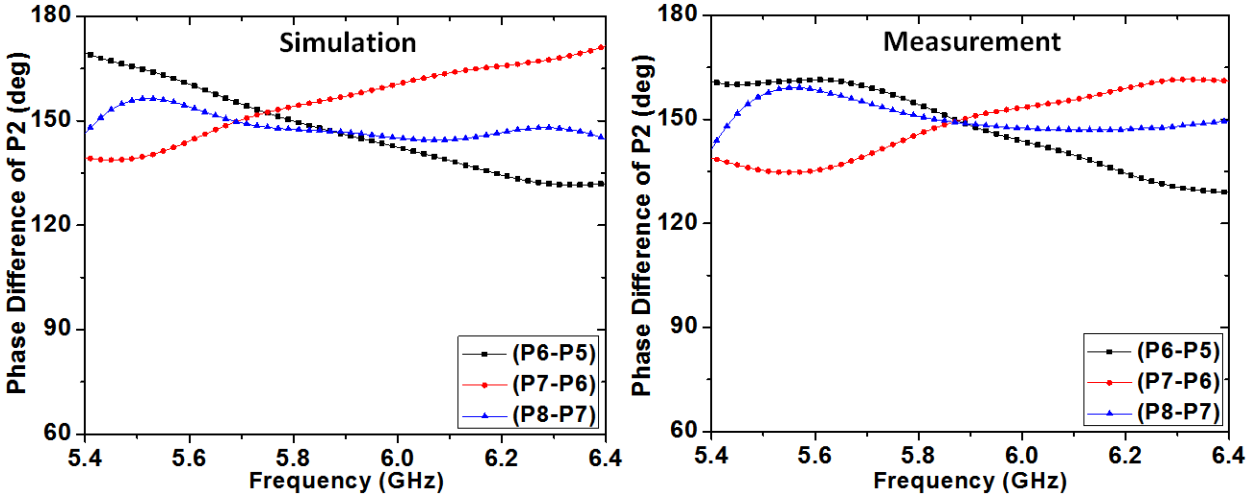

(a) (b)

Figure 5.9: (a) Simulated and (b) measured phase difference for input port P2.

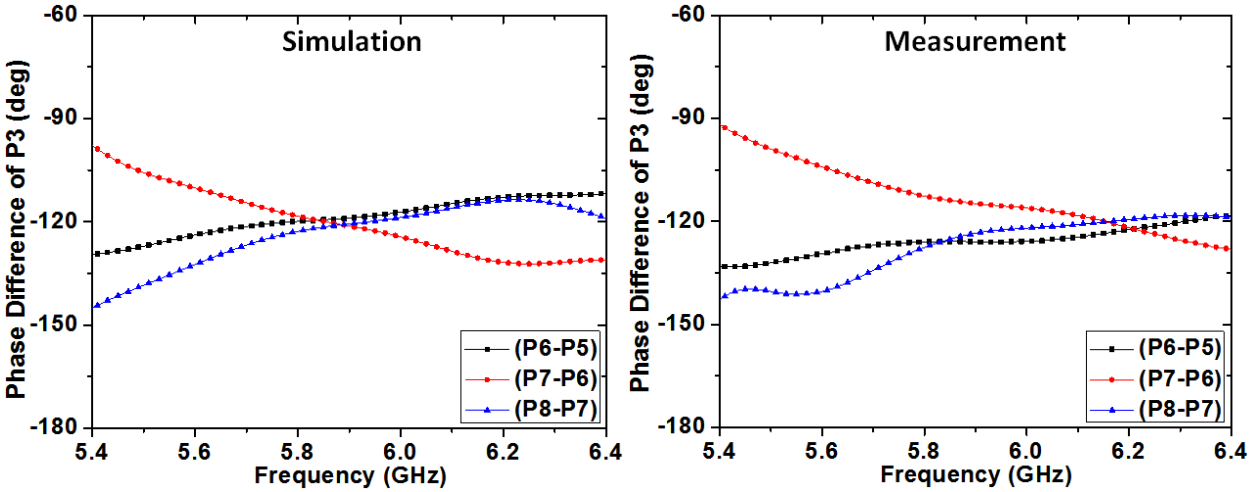

(a) (b)

Figure 5.10: (a) Simulated and (b) measured phase difference for input port P3.

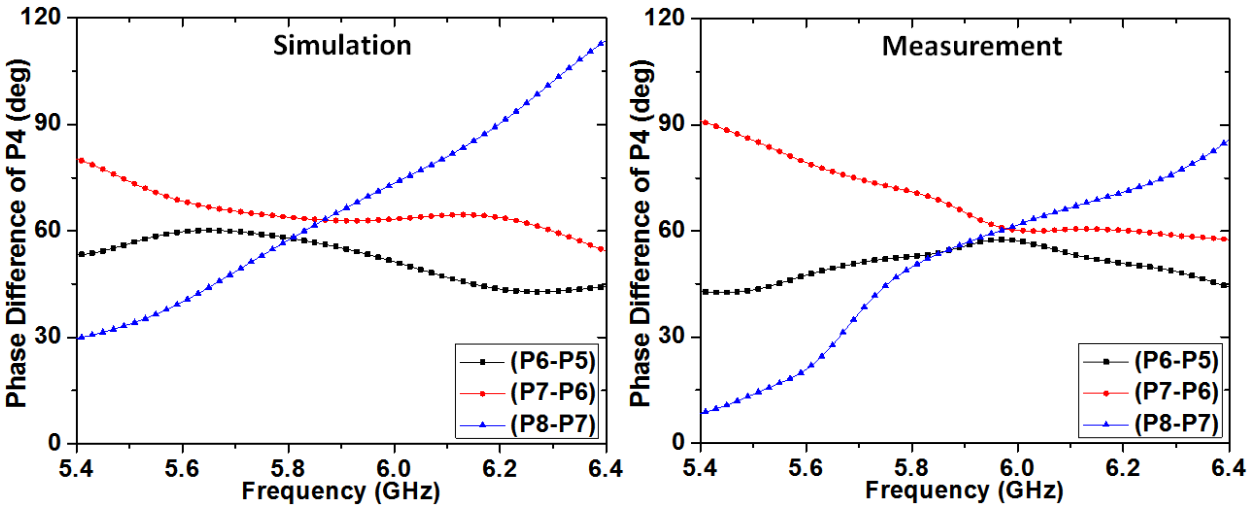

(a) (b)

Figure 5.11: (a) Simulated and (b) measured phase difference for input port P4.

5.4 Conclusion

A novel design of 4×4 Butler matrix is presented. Compared with the conventional Butler matrix, a new Butler matrix topology is proposed. The proposed Butler matrix can realize arbitrary combinations of progressive phase differences at the output ports. The structure of the proposed Butler matrix is single-layer and symmetrical, achieving a low cost and minimizing the imbalance on amplitude and phase. To verify the design concept, a Butler matrix with progressive phase differences -30°, +150°, -120°, and +60° is designed and characterized. Good agreement has been achieved between the measured and simulated results. The proposed design concept can be also applied to achieve a beam steering Butler matrix by using tunable couplers.

CHAPTER 6

NEW DESIGNS OF TUNABLE TERAHERTZ DEVICES USING GRAPHENE PARALLEL-PLATE WAVEGUIDE

6.1 Introduction

Graphene, one of the first two-dimensional (2D) materials, consists of 2-D arrangement of carbon atoms with a hexagonal structure [49]. Since the discovery of free-standing graphene in 2004 [50], there has been a rising attention about its applications in the physics, chemistry, and engineering domains. Graphene is a zero bandgap semiconductor which is very promising for nanoelectronic applications [51]. Graphene possesses a linear energy-momentum dispersion relation, which is similar with the dispersion relation of photons in free space [52]. This linear dispersion relation makes electrons behave like massless particles in graphene. As a result, graphene can obtain high carrier mobility ($5 \times 10^5\ \mathrm{cm}^2/\mathrm{Vs}$) [53]. Based on graphene's structure, its transport characteristics and conductivity can be tuned by the varying chemical potential (Fermi energy). To tune the chemical potential over a large range, methods using chemical doping, electrostatic bias, and magnetostatic bias have been applied and reported [54]-[61]. In the terahertz range, the monolayer graphene can provide unique surface plasmon polaritons (SPPs) with the low losses, strong field confinement, and powerful reconfiguration among many others [62]-[63]. Based on these unique electronic properties, a wide variety of graphene-based devices have been presented, including antennas [64]-[70], filters [71]-[72], switches [73]-[75], phase shifters [76], Faraday rotators [77]-[78], cloaks [79], absorbers [80], modulators [81]-[83], photomixers [84]-[85], polarizers [86], and transistors [87]-[91].

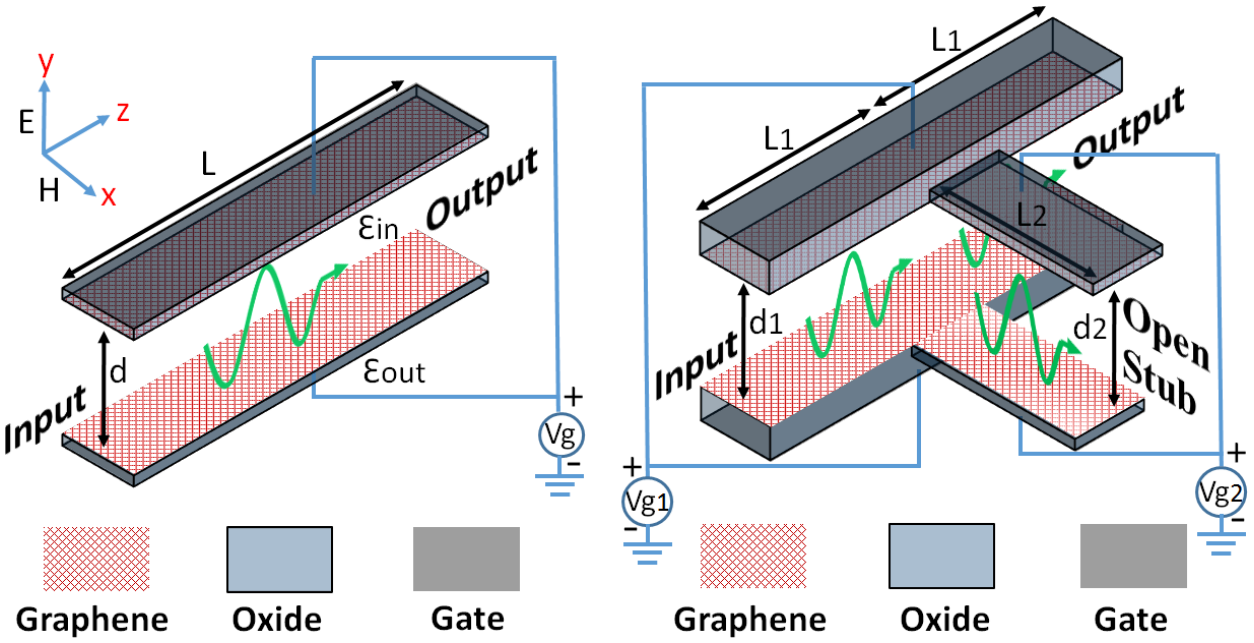

Figure 6.1: Schematic diagram of (a) the conventional GPPWG with a single uniform structure and (b) the proposed GPPWG with T-type structure.

Graphene parallel-plate waveguide (GPPWG) is formed by two graphene sheets spaced a distance apart [92]. GPPWG can guide quasi-transverse electromagnetic modes with attenuation similar to thicker-walled metal structures. Due to the surface conductivity on each graphene sheet, GPPWG's propagation characteristics can be tuned by varying the chemical potential. Recently, several tunable terahertz components have been designed using integrally-gated GPPWG (e.g. phase shifter [76]). However, adjusting the chemical potential of the gated section will simultaneously change the characteristic impedance and the electrical length of the GPPWG. As a result, it's difficult to keep one characteristic while tuning the other characteristics, making it difficult for realizing functional tunable THz devices such as multiple-port tunable THz devices.

To address this issue, several designs of two- and multiple-port tunable THz devices using the T-type GPPWG are developed. Using GPPWG with the T-type structure

can realize full-scale tunability of the GPPWG on operating frequency, characteristic impedance, and electrical length. Based on this new structure, it's possible to design two- and multiple-port terahertz devices with various tuning functions.

6.2 Features of GPPWG with Different Structures

Fig. 6.1(a) shows the original design of GPPWG with double-gate electrodes that are applied to control the chemical potential of the gated section [76]. Two laterally infinite graphene sheets are in parallel with a distance of *d*, and each graphene sheet is characterized by the surface conductivity. The surface conductivity σ can be derived from the Kubo formula [93], which is shown as follows:

$$\sigma(\mu_c) = \frac{je^2(\omega - j\tau^{-1})}{\pi\hbar^2} \times \left[\frac{1}{(\omega - j\tau^{-1})^2} \int_0^\infty \xi \left(\frac{\partial f_d(\xi, \mu_c, T)}{\partial \xi} - \frac{\partial f_d(-\xi, \mu_c, T)}{\partial \xi} \right) d\xi - \int_0^\infty \frac{f_d(-\xi, \mu_c, T) - f_d(\xi, \mu_c, T)}{(\omega - j\tau^{-1})^2 - 4\left(\frac{\xi}{\hbar}\right)^2} d\xi \right] \tag{6.1}$$

where μ_c is chemical potential, *e* is electron charge, ω is radian frequency, τ is phenomenological electron relaxation time, $\hbar$ is reduced Planck's constant, and ξ is energy. $f_d(\xi, \mu_c, T)$ is the Fermi-Dirac distribution:

$$f_d(\xi, \mu_c, T) = \left(e^{(\xi - \mu_c)/k_B T} + 1\right)^{-1} \tag{6.2}$$

where k_B is Boltzmann's constant, and *T* is temperature. Since the designed GPPWG operates in the THz frequency range, the intraband contributions dominate the surface conductivity. Then Eqn. 6.1 can be evaluated as

$$\sigma(\mu_c) = \sigma_{intra} = \frac{-je^2 k_B T}{\pi\hbar^2(\omega - j\tau^{-1})}\left[\frac{\mu_c}{k_B T} + 2ln\left(e^{-\mu_c/k_B T} + 1\right)\right] \tag{6.3}$$

Assuming $\mu_c/k_B T \gg 1$ over at least 500 K [92], the simplified equation of surface conductivity for all temperatures is obtained:

$$\sigma(\mu_c) = \frac{-je^2\mu_c}{\pi\hbar^2(\omega - j\tau^{-1})} \tag{6.4}$$

From Fig. 6.1(a), the propagation of GPPWG is along the *z*-axis, and the electromagnetic field is separated into transverse electric field TE (along the *y*-axis) and the transverse magnetic field TM (along the *x*-axis). A quasi-TEM can be realized by GPPWG since the graphene PPWG is similar to a perfectly conducting PPWG which supports a pure TEM mode [92]. For TM waves, the magnetic field can be described as $H_x(y)e^{\pm j\beta z}$, where β is the propagation constant. Assuming that two graphene sheets have the same surface conductivity, the approximate solution of β in GPPWG can be derived using Maxwell's equations [92]:

$$\beta \simeq k_0\sqrt{\frac{\varepsilon_{in}}{\varepsilon_0}\left\{1 + \frac{1}{{\eta_0}^2\sigma^2}\left[\frac{\varepsilon_{in}}{\varepsilon_0} - j\frac{2\eta_0\sigma}{k_0 d}\right]\right\}} \tag{6.5}$$

where ε_{in} is the material permittivity within the GPPWG (between two graphene sheets, as shown in Fig. 6.1(a)), $k_0 = \omega\sqrt{\mu_0\varepsilon_0}$ is the free-space wavenumber, and $\eta_0 = \sqrt{\mu_0/\varepsilon_0}$ is the free-space wave impedance. Due to sufficiently large surface conductivity, the material permittivity outside the waveguide plays a minor role on the propagation constant. For simplicity, both inside and outside permittivities are the same as free-space ($\varepsilon_{in} = \varepsilon_{out} = \varepsilon_0$). Under these assumptions, Eqn. 6.5 can be reduced as:

$$\beta \simeq \sqrt{\omega^2\mu_0\varepsilon_0 - j\frac{2\varepsilon_0\omega}{\sigma d}} \tag{6.6}$$

Substituting Eqn. 6.4 into 6.6, the relationship between the propagation constant β and the surface conductivity σ is derived as follows:

$$\beta \simeq \sqrt{\omega^2 \mu_0 \varepsilon_0 + \frac{2\omega^2 \varepsilon_0 \pi \hbar^2}{e^2 \mu_c d} - j\frac{2\omega \varepsilon_0 \pi \hbar^2}{e^2 \mu_c d\tau}} \tag{6.7}$$

In this work, we set the relaxation time τ = 4 ps, and the value of chemical potential is between 0 and 1 eV. In the THz frequency range, the real part of the propagation constant plays the major role. Applying the full-wave simulations and the transfer-matrix method [94]-[95], the propagation characteristics of GPPWG in free-space can be obtained as:

$$\theta_c = \beta L \tag{6.8}$$

$$Z_c = \frac{E_y d}{H_x} = \frac{\beta d}{\omega \varepsilon_0} \tag{6.9}$$

where θ_c is the electrical length, Z_c is the characteristic impedance, and L is the physical dimension of GPPWG. From Eqn. 6.7 – 6.9, the propagation characteristics of GPPWG depend on the propagation constant, which can be controlled by tuning the value of the chemical potential. Fig. 6.2 shows the contours of the normalized characteristic impedance and electrical length of the GPPWG with physical dimension L = 1 um and d = 300 nm, varying the operating frequency and the chemical potential. In the whole paper, Z_0 is set as the free-space impedance of the GPPWG with d = 300 nm.

To tune the chemical potential, the GPPWG is gated by the bias voltage V_g on the top and bottom graphene sheets (as shown in Fig. 6.1(a)). The variation of chemical potential is equivalent to the voltage drop V_{ch} across the quantum capacitance C_q. Based on the Kirchhoff's law, V_{ch} can be derived as [96]-[97]:

$$V_{ch} = \frac{\mu_c}{e} = \frac{C_{ox}V_g}{C_{ox} + \frac{1}{2}C_q(V_{ch})} \tag{6.10}$$

where $C_{ox} = \varepsilon_{ox}/t_{ox}$ (ε_{ox} and t_{ox} are the permittivity and thickness of the gate oxide, respectively) is the oxide capacitance. Under the condition $eV_{ch} \gg k_B T$, a simple equation of C_q can be expressed as:

$$C_q = \frac{2e^3|V_{ch}|}{\pi(\hbar v_F)^2} \tag{6.11}$$

where v_F is Fermi velocity. Substituting Eqn. 6.11 into Eqn. 6.10 yields:

$$\mu_c = \frac{\hbar v_F}{2e^2}\left(-\pi C_{ox}\hbar v_F + \sqrt{(\pi C_{ox})^2 + 4e^3\pi C_{ox}V_g}\right) \tag{6.12}$$

By changing the bias voltage, the propagation characteristics of GPPWG can be easily controlled. However, as mentioned previously, there is a strong constraint for the realizable propagation characteristics using the conventional GPPWG. From Eqn. 6.8 and 6.9, it is found that a given propagation constant will lead to a certain combination of electrical length and characteristics impedance. This property will prevent the GPPWG from achieving the full-scale tunability. Therefore, it is very difficult to achieve flexible combination of electrical length and characteristics impedance using the structure in Fig. 6.1(a).

To address this issue, a new T-type GPPWG as shown in Fig. 6.1(b) is proposed. This structure is constructed by two series-connected GPPWGs and one shunt open-ended GPPWG. The two series-connected GPPWGs have identical physical dimensions (length *L*1 and thickness *d*1) and are gated by the same bias voltage V_{g1}. An additional shunt open-ended GPPWG (length *L*2, thickness *d*2, and bias voltage V_{g2}) is tapped at the center of these two series sections. To avoid undesired influence on graphene

plasmons, the width of all GPPWGs should be larger than 20 nm [98]-[99]. The proposed T-type structure can be analyzed using the transfer matrix method (i.e. *ABCD*-matrix) [100]:

$$A_T = D_T = \cos 2\theta_1 - \frac{Z_1 \sin 2\theta_1 \tan \theta_2}{2Z_2} \tag{6.13}$$

$$B_T = jZ_1 \sin 2\theta_1 - j\frac{{Z_1}^2 \sin^2 \theta_1 \tan \theta_2}{Z_2} \tag{6.14}$$

$$C_T = j\frac{2 \sin \theta_1 \cos \theta_2}{Z_1} + j\frac{\cos^2 \theta_1 \tan \theta_2}{Z_2} \tag{6.15}$$

where Z_1, Z_2 and θ_1, θ_2 are the characteristic impedances and the electrical lengths of the series and open-ended sections, respectively. To realize the specific values of impedance Z_c and electrical length θ_c using the proposed T-type structure, $A_T = \cos \theta_c$ and $B_T = jZ_c \sin \theta_c$ should be satisfied. Substituting these two equations into Eqn. 6.13 - 6.14, yields:

$$Z_1 = \frac{Z_c \sin \theta_c \cot \theta_1}{1 + \cos \theta_c} \tag{6.16}$$

$$Z_2 = \frac{Z_c \sin \theta_c \cos^2 \theta_1 \tan \theta_2}{(\cos 2\theta_1 - \cos \theta_c)(1 + \cos \theta_c)} \tag{6.17}$$

Based on Eqn. 6.8 and 6.9, it is found that the characteristic impedance and the electrical length of each GPPWG section can be controlled by the corresponding propagation constant. By substituting Eqn. 6.8 – 6.9 into Eqn. 6.16 – 6.17, two important design equations can be obtained:

$$\frac{Z_c \sin \theta_c \cot(\beta_1 L_1)}{1 + \cos \theta_c} = \frac{\beta_1 d_1}{\omega \varepsilon_0} \tag{6.18}$$

$$\frac{Z_c \sin \theta_c \cos^2(\beta_1 L_1) \tan(\beta_2 L_2)}{(\cos(2\beta_1 L_1) - \cos \theta_c)(1 + \cos \theta_c)} = \frac{\beta_2 d_2}{\omega \varepsilon_0} \tag{6.19}$$

where β_1 and β_2 are the propagation constants of the series-connected and shunt open-ended GPPWGs, respectively. It is found that for a given combination of impedance Z_c and electrical length θ_c, the corresponding propagation constants β_1 and β_2 can be obtained by solving Eqn. 6.18 – 6.19. Therefore, by tuning the chemical potentials of these GPPWGs, full-scale tunabilitiy can be achieved by using the proposed T-type GPPWG. Fig. 6.3 shows that the values of normalized characteristic impedance and electrical length of the series and open-ended GPPWG sections can be flexible by tuning the chemical potential μ_{c1}, μ_{c2} respectively. Here, we set operating frequency *f* = 5 THz, *d*1 = *d*2 = 200 nm, *L*1 = 500 nm, and *L*2 = 1 um. In summary, the design procedure for the T-type GPPWG to achieve the desired characteristic impedance and electrical length can be described as the following:

1) Select the desired values of characteristic impedance Z_c and electrical length θ_c, which will be realized by the T-type GPPWG structure;
2) Use Eqn. 6.18 to solve the value of β_1, then obtain the value of β_2 by Eqn. 6.19;
3) Substitute β_1 and β_2 into Eqn. 6.7 to get the values of μ_{c1} and μ_{c2};
4) Finally, the corresponding bias voltages V_{g1} and V_{g2} can be obtained by solving Eqn. 6.12.

In the next sections, several two-port and multiple-port tunable terahertz devices using the proposed T-type GPPWG are presented to demonstrate its applications.

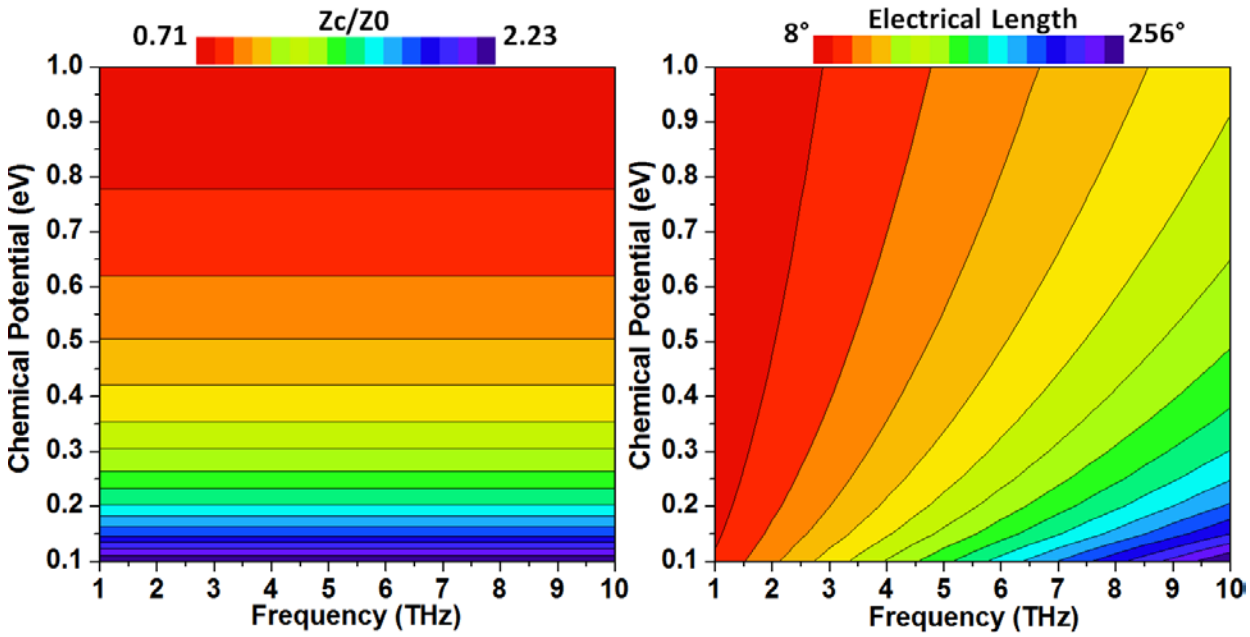

(a) (b)

Figure 6.2: Contours of (a) normalized characteristic impedance and (b) electrical length of the GPPWG in Fig. 6.1(a), varying the operating frequency and chemical potential.

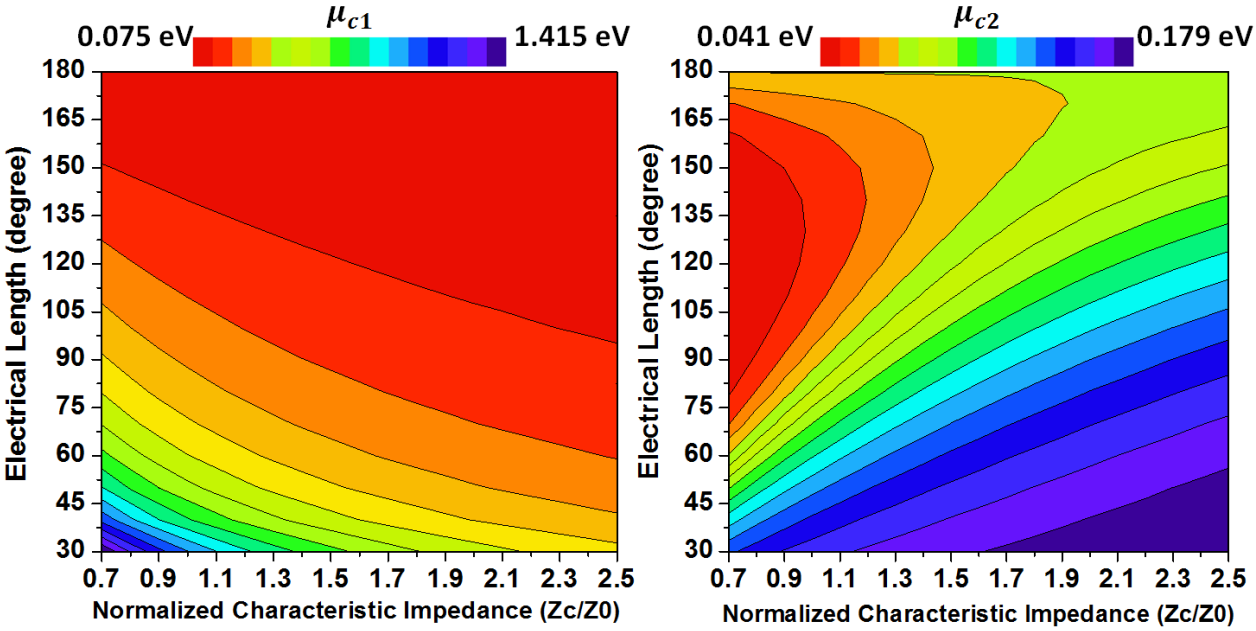

(a) (b)

Figure 6.3: Calculated results for the proposed GPPWG: (a) Contours of normalized characteristic impedance and electrical length of series GPPWG section with corresponding chemical potential μ_{c1}; (b) Contours of normalized characteristic impedance and electrical length of open-ended GPPWG section with corresponding chemical potential μ_{c2}.

6.3 Phase Shifter with Flexible Phase Difference

Phase shifter is an indispensable component in the beam-forming system for applications such as telecommunication and radar. The conventional phase shifter employs single transmission line with the characteristic impedance Z_c and the electrical length θ_c (as shown in Fig. 6.4(a)). But during the tuning of the phase shift, the characteristic impedance is also changed. To realize the tuning on phase shift with a fixed characteristic impedance, the proposed T-type GPPWG (as shown in Fig. 6.4(b)) is applied to replace the conventional structure. In the proposed design, the operating frequency is *f* = 5 THz, the physical lengths of the T-type GPPWG are *L*1 = 500 nm, *L*2 = 1 um, and the thickness of the GPPWG are *d*1 = *d*2 = 200 nm (referring to Fig. 6.1(b)). The tuning range of the phase shift θ_c is from -30° to -180°, and the characteristic impedance Z_c is matched with input/output port impedance (Z_0). Following the design procedure described in last section, the chemical potentials μ_{c1}, μ_{c2} corresponding to different phase difference can be obtained, and they are plotted in Fig. 6.5.

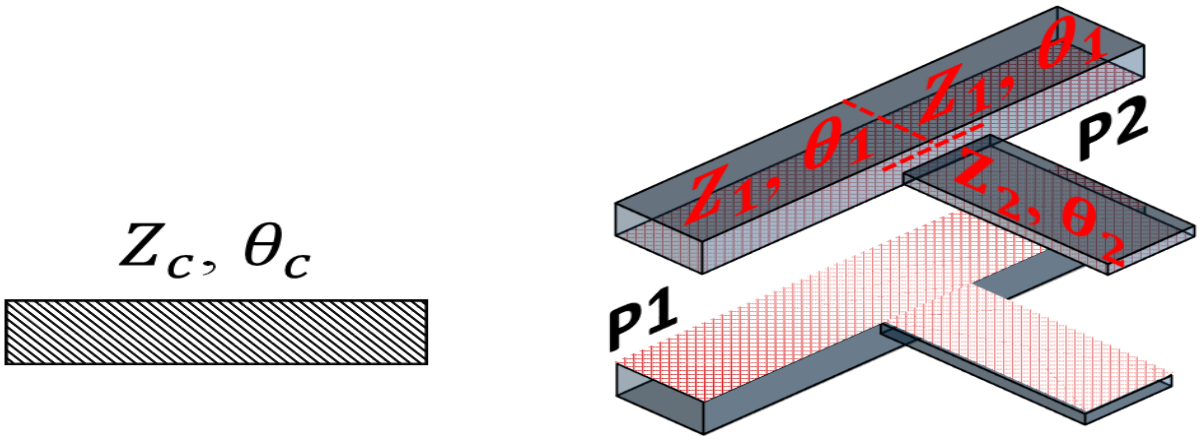

(a) (b)

Figure 6.4: Configuration of (a) the conventional phase shifter and (b) the proposed phase shifter using GPPWG with the T-type structure.

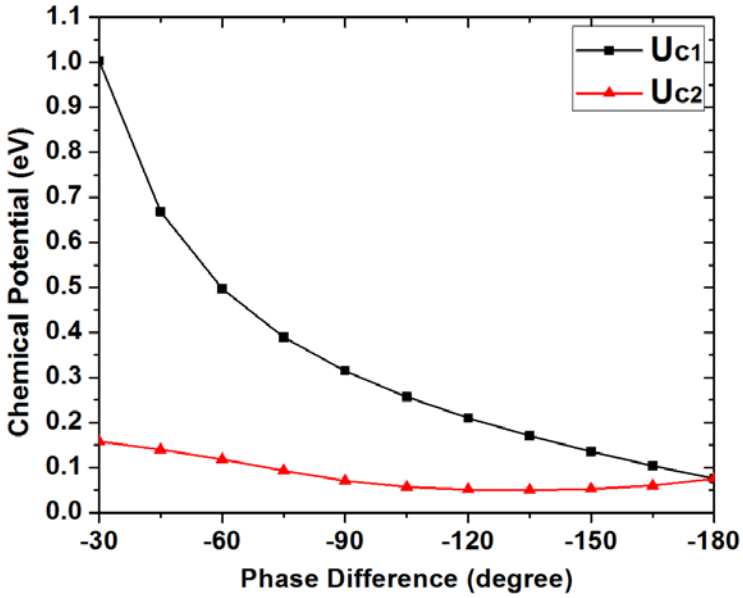

Figure 6.5: Variation of the chemical potentials μ_{c1} and μ_{c2} versus the phase difference of the proposed phase shifter.

Fig. 6.6 presents the simulation results of S-parameters and phase responses of the proposed phase shifter. From Fig. 6.6(a), it is observed that complete transmission ($|S_{21}|$ = 0 dB) is achieved at the operating frequency 5 THz. For the return loss, it can be better than 50 dB ($|S_{11}| > 50$ dB, as shown in Fig. 6.6(b)) at the working frequency, which indicates that the phase shifter is always matched to the input/output port impedance (Z_0) (therefore its characteristic impedance is fixed to Z_0). The phase responses are presented in Fig. 6.6(c). It is observed that, by tuning the chemical potential to the appropriate values (as shown in Fig. 6.5), the phase shift of the proposed THz phase shifter based on the T-type GPPWG can be tuned from -30° to -180°. Based on our calculations, the range of the realizable phase shift using the proposed design can be further extended, if a larger chemical potential is available in practice (e.g. $\mu_c > 1$ eV).

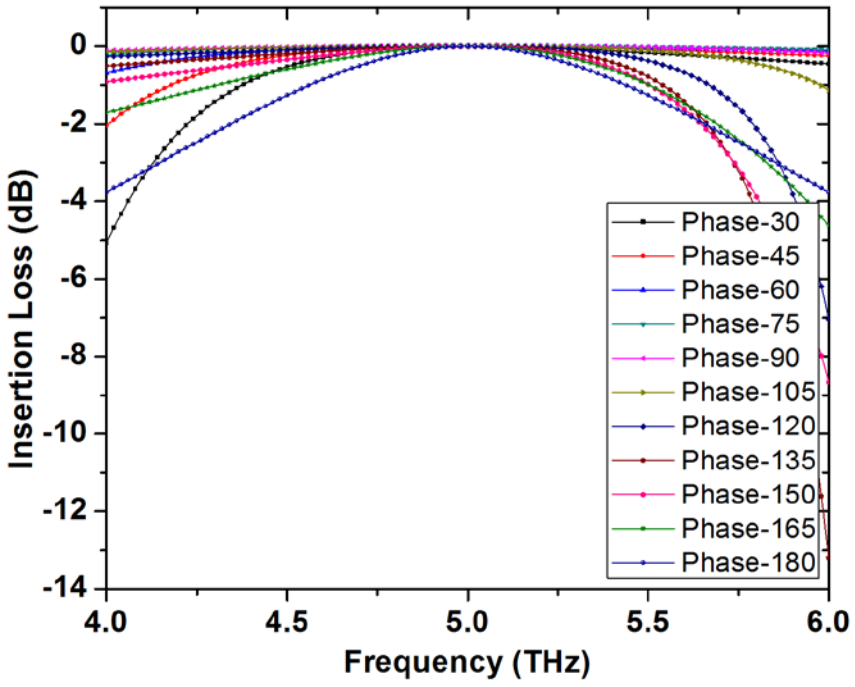
Insertion Loss (dB)
0
-2
-4
-6
-8
-10
-12
-14
4.0
4.5
5.0
5.5
6.0
Frequency (THz)
Phase-30
Phase-45
Phase-60
Phase-75
Phase-90
Phase-105
Phase-120
Phase-135
Phase-150
Phase-165
Phase-180

(a)

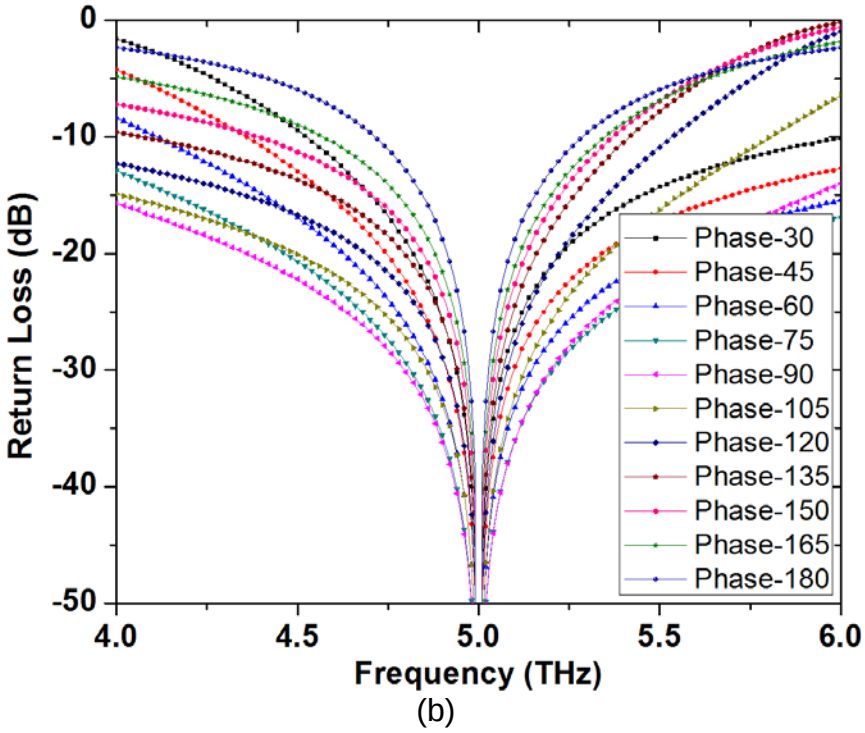
Return Loss (dB)
0
-10
-20
-30
-40
-50
4.0
4.5
5.0
5.5
6.0
Frequency (THz)
Phase-30
Phase-45
Phase-60
Phase-75
Phase-90
Phase-105
Phase-120
Phase-135
Phase-150
Phase-165
Phase-180

(b)

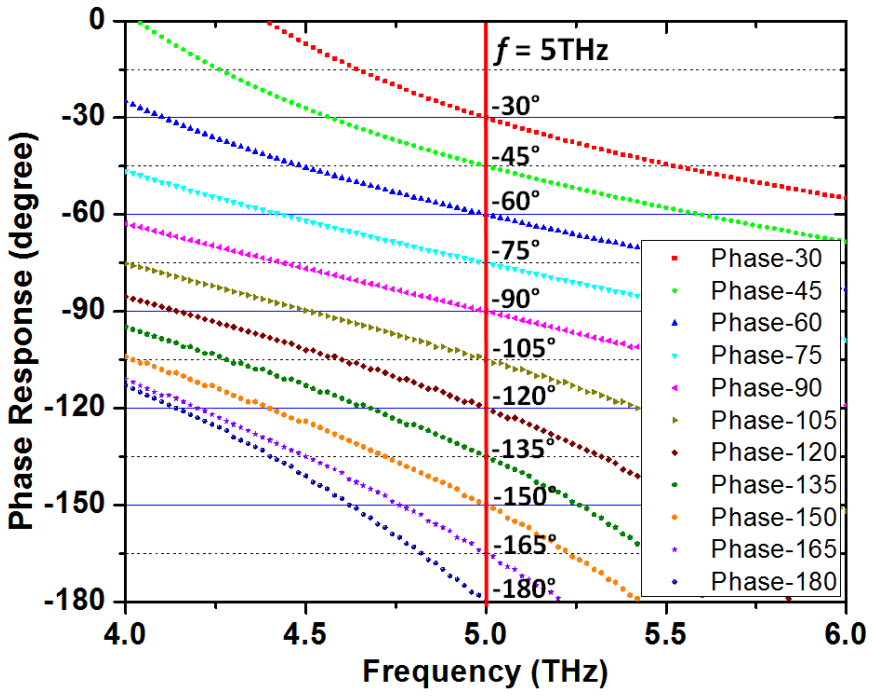

(c)

Figure 6.6: Simulation results of (a) insertion loss S_{21} (b) return loss S_{11} and (c) phase response of the proposed phase shifter with flexible phase difference.

6.4 Phase Shifter with Tunable Frequency

Recent development in modern communication systems has imposed new design requirements such as compact size, low cost and wide-band operation. Among these characteristics, the wide-band operation can result in reductions for both size and cost of the whole system. Therefore, it is attractive to design circuits and components covering a broad range of spectrum. To meet this requirement, we have designed THz phase shifters with tunable working frequencies and fixed phase shift and characteristic impedance to cover a wide frequency range. It is found that, using the proposed GPPWG as shown in Fig. 6.4(b), tuning of the operating frequency can be easily achieved. To verify the proposed design concept, a 45° THz phase shifter with tunable working frequency from 3 THz to 7 THz is designed and simulated. The physical dimensions of

the series/open-end GPPWGs applied in the designed phase shifter are: *L*1 = 500 nm, *L*2 = 1 um, and *d*1 = *d*2 = 200 nm. The input/output port impedance is again equal to Z_0. By solving Eqn. 6.18 – 6.19 and 6.7, the corresponding values of chemical potentials μ_{c1}, μ_{c2} when the phase shifter is operating at different frequencies are given in Table 6.1. Fig. 6.7(a) shows the simulation results of insertion loss. It is observed that the desired complete transmission ($|S_{21}|$ = 0 dB) is achieved at each operating frequency (e.g. 3, 4, 5, 6, 7 THz). In Fig. 6.7(b), extremely low return loss is obtained at desired operating frequencies (it is again tuned from 3 to 7 THz), verifying the good matching of the phase shifter. For the phase response, the induced phase shift is kept as -45° while the operating frequency is tuned from 3 THz to 7 THz (as shown in Fig. 6.7(c)). Therefore, by using the proposed GPPWG, a phase shifter with tunable working frequency and fixed characteristic impedance and phase shift can be realized.

Table 6.1

Calculated values of chemical potentials for phase shifter with tunable frequency

***f* (THz)**	**μ_{c1} (eV)**	**μ_{c2} (eV)**
3	0.384	0.034
4	0.523	0.079
5	0.668	0.140
6	0.819	0.215
7	0.977	0.307

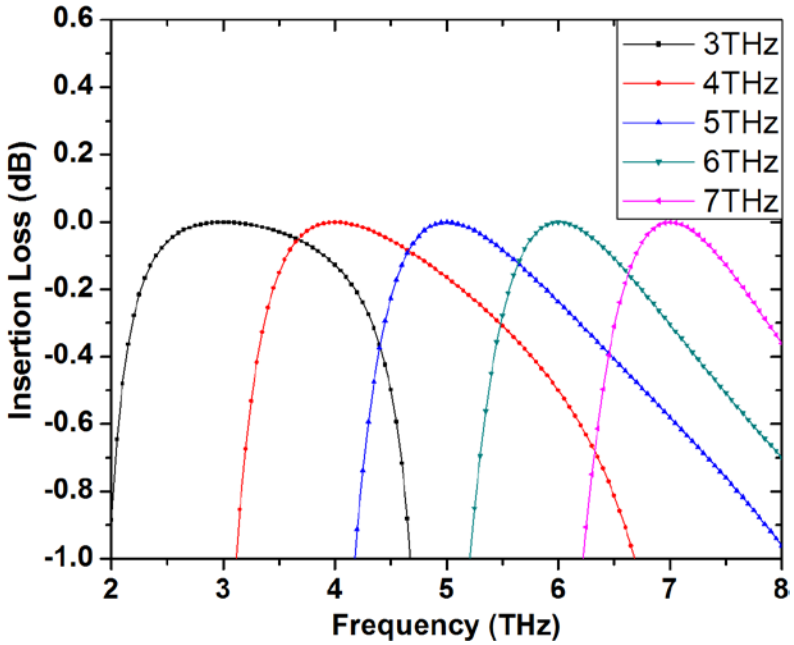
Insertion Loss (dB)
Frequency (THz)
3THz
4THz
5THz
6THz
7THz

(a)

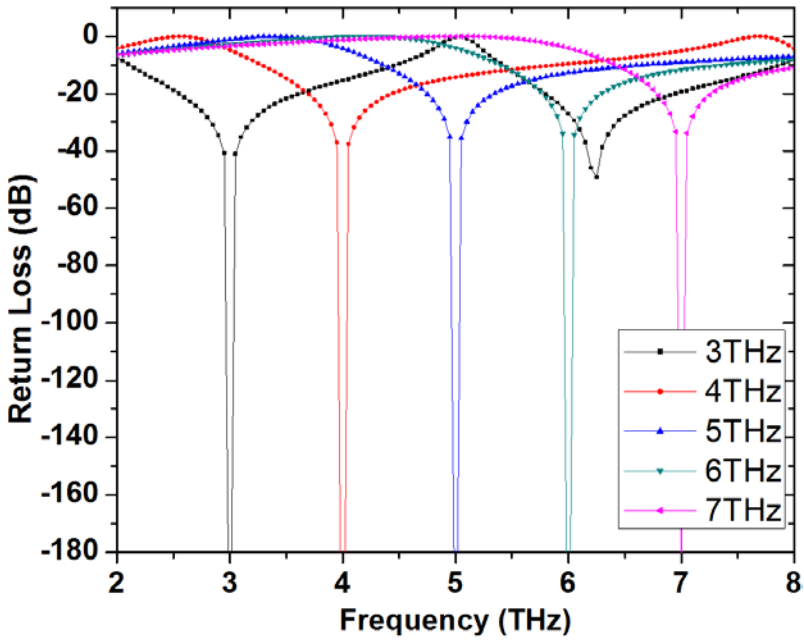
Return Loss (dB)
Frequency (THz)
3THz
4THz
5THz
6THz
7THz

(b)

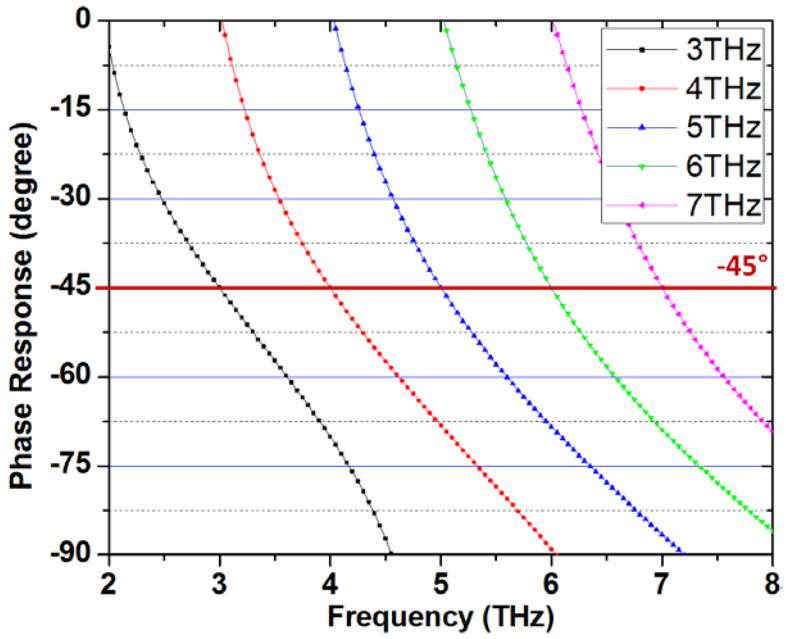

(c)

Figure 6.7: Simulation results of (a) insertion loss S_{21} (b) return loss S_{11} and (c) phase response of the proposed phase shifter with tunable frequency.

6.5 Power Divider with Tunable Power Ratio

Fig. 6.8(a) shows a Wilkinson power divider with unequal power splits. When the signal go through the input port P1, the power will be split as a ratio between output ports P2 and P3: P3/P2=*k*. The characteristic impedance and electrical length of each transmission line (TL) section can be obtained by the following design equations:

$$Z_a = Z_0\sqrt{K(1+K^2)} \tag{6.20}$$

$$Z_b = Z_0\sqrt{\frac{1+K^2}{K^3}} \tag{6.21}$$

$$Z_c = Z_0\sqrt{K} \tag{6.22}$$

$$Z_d = \frac{Z_0}{\sqrt{K}} \tag{6.23}$$

$$\theta_a = \theta_b = \theta_c = \theta_d = 90° \tag{6.24}$$

where $K = \sqrt{k}$ and Z_0 is the input/output port impedance. To realize tunable power ratio on the power divider, we can employ the proposed GPPWG with T-type structure to replace each section of the conventional power divider in Fig. 6.8(a). Fig. 6.8(b) shows the configuration of the power divider with tunable power ratio. Each T section will apply um. Fig. 6.9 shows the calculation values of chemical potential for each T section, varying the power ratio. The simulation results of S-parameter with *k* = 1/2, 1/4, and 1/6 are shown in Fig. 6.10, and the values of insertion losses at 5 THz are presented in Table 6.2. It is found that the values of insertion losses show good agreement with the desired power ratio, verifying our design concept.

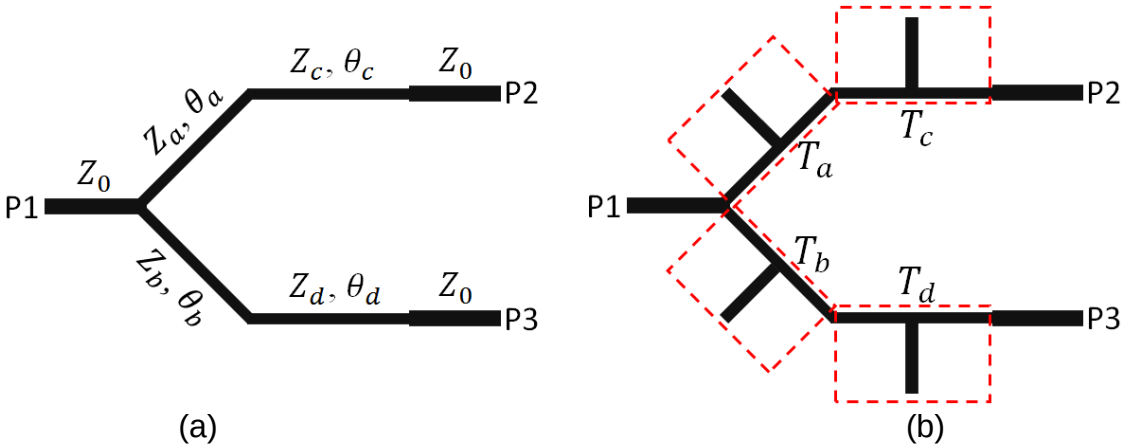

(a) (b)

Figure 6.8: Configuration of (a) the conventional power divider with unequal power splits and (b) the proposed power divider with tunable power ratio (overhead view).

Table 6.2

Simulation values of insertion losses of power divider with different power ratio

k	**½**	**¼**	**1/6**
S21(dB)	-1.741	-0.969	-0.669
S31(dB)	-4.748	-6.990	-8.451

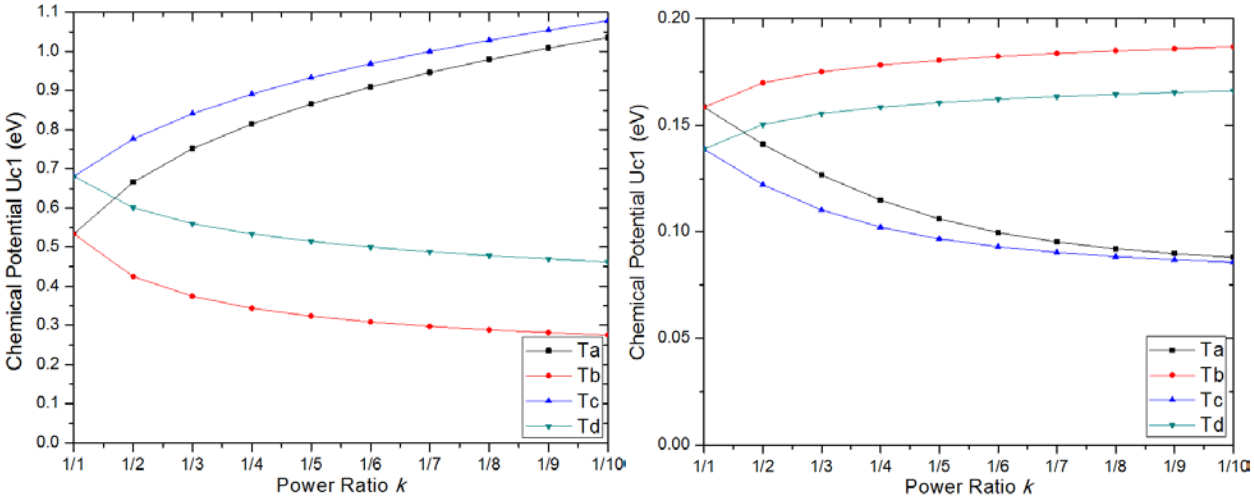

(a) (b)

Figure 6.9: Calculation values of the chemical potential (a) μ_{c1} and (b) μ_{c2} for each T section in the proposed power divider, varying the power ratio from 0.1 to 1.

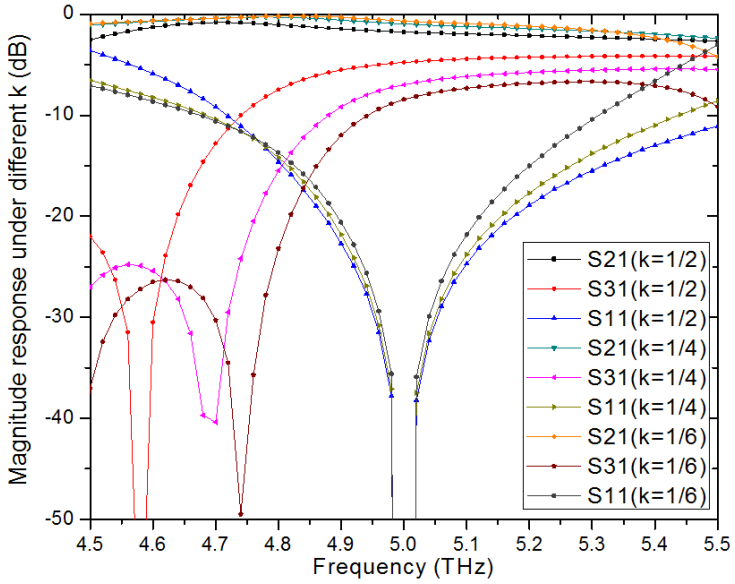

Figure 6.10: Simulation results of S-parameter of the proposed power divider with the power ratio *k* = ½, ¼, and 1/6.

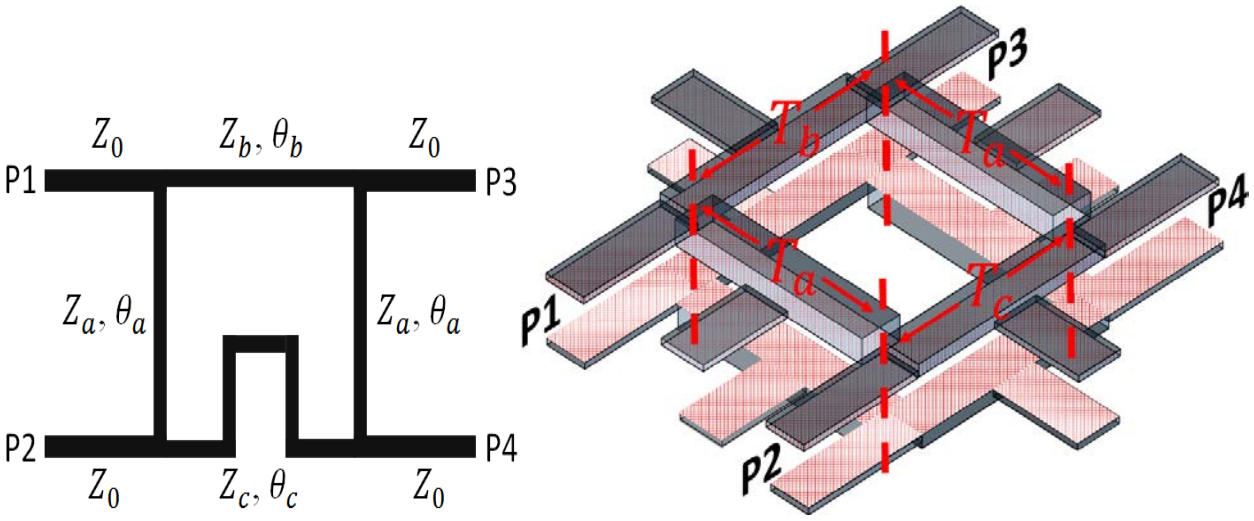

(a) (b)

Figure 6.11: Configuration of (a) the conventional coupler with fixed phase difference (top view) and (b) the proposed coupler with tunable phase difference (3D view), consisting T-type GPPWG sections *Ta*, *Tb*, and *Tc*.

6.6 Coupler with Tunable Phase Difference

Finally, we have devised a THz coupler with tunable phase difference. Coupler is one of the fundamental circuit components. It has been applied extensively in various high frequency systems including data modulators, multipliers, and antenna feeding networks. Fig. 6.11(a) shows the configuration of a conventional coupler with fixed phase difference. The phase difference $\Delta\theta$ between two output ports P3 and P4 can be characterized as:

$$P41 - P31 = -\Delta\theta \tag{6.25}$$

$$P32 - P42 = \pi + \Delta\theta \tag{6.26}$$

The characteristic impedances and electrical lengths of each transmission line section within the coupler can be derived as:

$$Z_a = Z_0 \sin \Delta\theta \tag{6.27}$$

$$Z_b = Z_c = \frac{Z_0 \sin \Delta\theta}{\sqrt{1 + \sin^2 \Delta\theta}} \tag{6.28}$$

$$\theta_a = 90° \tag{6.29}$$

$$\theta_b = \cos^{-1}\left(\frac{-\cos \Delta\theta}{\sqrt{2}}\right) \tag{6.30}$$

$$\theta_c = 180° - \theta_b \tag{6.31}$$

where Z_0 is the input/output port impedance. To realize a coupler with tunable phase difference, the proposed GPPWG (as shown in Fig. 6.1(b)) is applied to replace each TL section of the coupler in Fig. 6.11(a). The configuration of the designed tunable THz coupler is shown in Fig. 6.11(b). The design procedure of the proposed THz coupler can be summarized as the following: 1) determine the range of the phase difference $\Delta\theta$; 2) use Eqn. 6.27 – 6.31 to obtain the values of the characteristic impedance and electrical length of each TL section; 3) follow the design procedures mentioned before to get the values of chemical potentials for different GPPWG sections. To verify the proposed design concept, a coupler working at 3 THz with the phase difference (between two output ports P3 and P4) tuned from 20° to 160° is designed and simulated. For T_a sections (as marked in Fig. 6.11(b)), $L1$ = 800 nm, $L2$ = 1 um, and $d1$ = $d2$ = 300 nm. For T_b and T_c sections, $L1$ = 500 nm, $L2$ = 1 um, and $d1$ = $d2$ = 100 nm. Fig. 6.12 shows the calculated values of chemical potentials for each T section when the phase difference is varied. Fig. 6.13 shows the simulation results of the coupler with the phase difference $\Delta\theta$ = 30°. From Fig. 6.13(a), at the operating frequency 3 THz, the insertion losses are 3.01 dB ($|S_{31}|$, $|S_{41}|$, $|S_{32}|$, $|S_{42}|$ = 3.01 dB). The return loss and isolation are better than 50 dB ($|S_{11}|$, $|S_{21}|$ > 50 dB). In Fig. 6.13(b), the phase difference between two output ports is $P41$ - $P31$ = -30°, and $P32$ – $P42$ = -150° at 3 THz. In Fig. 6.14, the simulation results of the coupler

with the phase difference $\Delta\theta$ = 45° are plotted. At 3 THz, the insertion losses are about 3.05 dB while the return loss and isolation are both better than 50 dB (as shown in Fig. 6.14(a)). For the phase difference between output ports, *P*41 - *P*31 = -45°, and *P*32 – *P*42 = -135° at 3 THz (as shown in Fig. 6.14(b)). All the simulation results agree well with the design theory, verifying the performance of the designed tunable THz coupler with tunable phase difference.

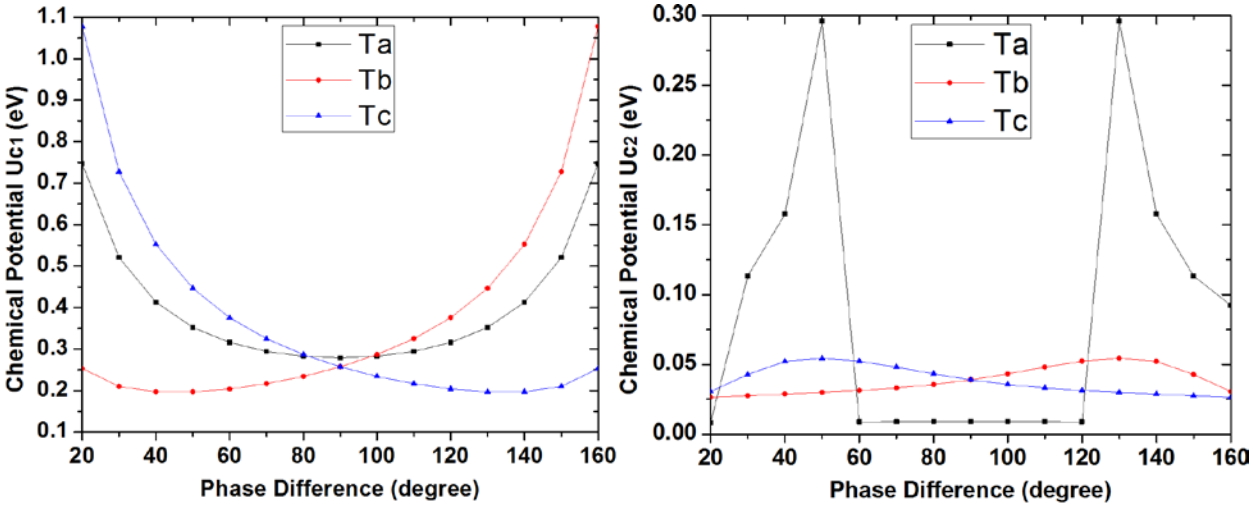

(a) (b)

Figure 6.12: Calculated chemical potentials (a) μ_{c1} and (b) μ_{c2} for each T section in the proposed tunable THz coupler, where the phase difference $\Delta\theta$ varies from 20° to 160°.

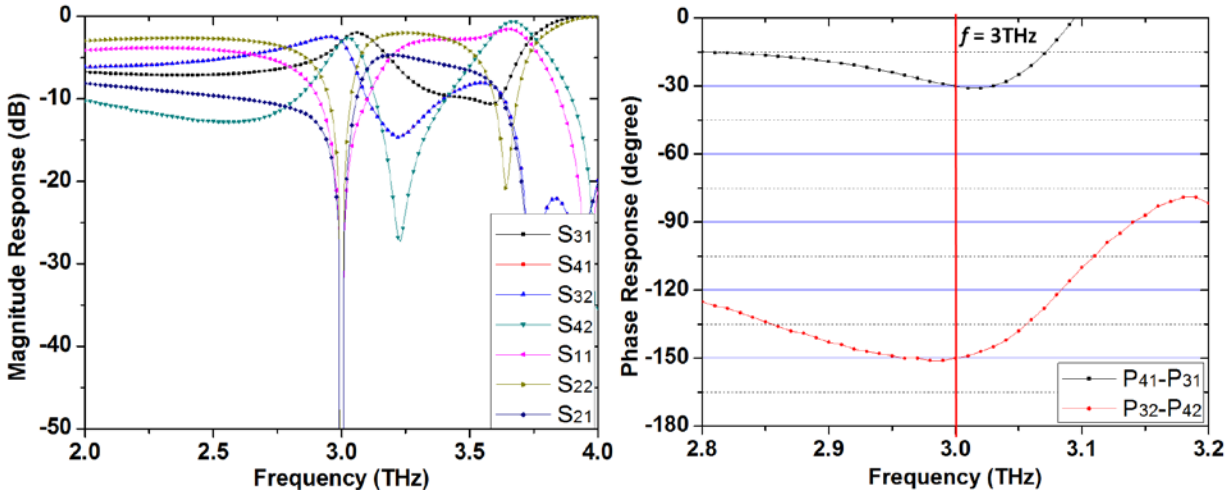

(a) (b)

Figure 6.13: Simulation results of (a) magnitude response and (b) phase response for the proposed tunable THz coupler when $\Delta\theta$ = 30°.

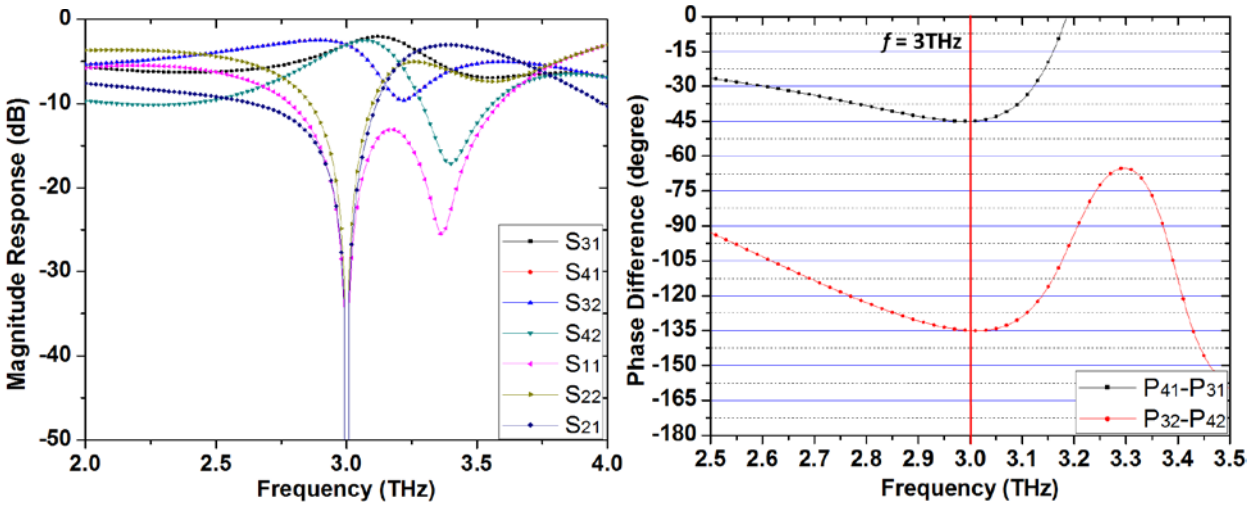

(a) (b)

Figure 6.14: Simulation results of (a) magnitude response and (b) phase response for the proposed tunable THz coupler when $\Delta\theta = 45°$.

Overall, the designed phase shifters and tunable couplers have proved that the proposed T-type GPPWG can be applied to realize two-/multiple-port tunable THz devices with flexible performance.

6.7 Conclusion

Novel designs of tunable THz devices using graphene parallel-plate waveguide (GPPWG) are proposed. Specifically, by combining the GPPWG with the T-type structure, the characteristic impedance and electrical length of GPPWG can be fully controlled. To verify the proposed design concept, several designs of tunable terahertz devices, such as a phase shifter with tunable phase difference, a phase shifter with tunable frequency, and a coupler with tunable phase difference are designed and simulated. All the simulation results show good agreement with the design theory. The proposed design provides a novel approach to design THz components with tunable and flexible responses, demonstrating the potential of graphene for THz systems and applications.

CHAPTER 7

NOVEL ELECTRICALLY TUNABLE FEW-LAYER METASURFACE FOR DYNAMICALLY AND SIMULTANEOUSLY CONTROLLING BOTH THE PHASE AND AMPLITUDE OF ELECTROMAGNETIC WAVES

7.1 Introduction

Electromagnetic metasurface is an artificial two-dimensional metamaterial structure consisting of planar electromagnetic (EM) units in subwavelength scales. Since metasurface was introduced to vary the propagation for incident light [101], it has been widely applied for controlling electromagnetic wave and light propagation. The manipulation of EM phase often play the key role in applications such as flat lens [102]-[104], wave-front manipulations [105]-[106], holograms [107]-[108], and polarization controls [109]. The conventional technology on phase modulation is achieved by modulating the refractive/reflective index of bulk metamaterials [110]-[111]. The total size of bulk metamaterials is frequently bulky (it can be the order of operating wavelength), increasing the degree of difficulty on fabrication. Due to the large volume of bulk metamaterials, a significant part of energy will be lost among the metal-layers. Comparing with the bulk metamaterials, the metasurface has attracted more attention from researchers due to its ultra-thin and planar structure. Recently, a mass of metasurface achievements have exhibited the great capability of phase control on the EM wave and light propagation. The most common efficient approach is to design resonators with various shapes and sizes and arrange them on a periodic layout [112]-[185]. Some literatures present a dynamic phase control by installing varactor diodes in the metasurface [186]-[188].

Based on the rapid development in the wireless communication, the only phase manipulation cannot satisfy the new requirements. The higher level of controlling on EM wave and light becomes the main demand in the novel application, such as high resolution imaging, multi-wave field analysis, dynamic holography, active emission control, and laser beam shaping. These applications not only need phase control but also require that the amplitude/magnitude can be controlled. It implies that an independent and complete manipulation is becoming the new challenge for metasurface research, forcing researchers to realize more approaches. Due to this attractive motivation, some successful approaches have been presented for simultaneous phase and amplitude/magnitude control [189]-[194]. One simple method is applying resonators with different shape or size [189]-[192]. This method can maintain a single two-dimensional structure, and it is conventional for fabrication. However, this metasurface are mostly passive, which means that it is impossible to tune the metasuface externally. Moreover, for the applications with the higher requirement on tuning scale (such as high resolution imaging), the amount of resonators in each periodic array will be very huge, increasing the total size of metasurface. In [193], the metasurface can fully control both the phase and magnitude of the transmission/reflection independently by employing the tunable element, such as varactor diode. Adjusting the external bias voltages on the varactor diodes can significantly improve the flexibility on controlling and realize a compact size. From the results in [193], although full 360° phase tuning is achieved, the magnitude control is seriously restricted within two extreme values (transmissivity equal to 0 or 1). It is necessary to extend the available range of magnitude control. Some novel metasurface is designed by replacing metal with graphene [194]. Graphene is a two-dimensional

material, consisting of 2-D arrangement of carbon atoms with a hexagonal structure. Based on graphene's structure, its transport characteristics and conductivity can be controlled by the varying chemical potential (Fermi energy). This implies that Graphene has powerful capability of controlling EM wave and light propagation. Meanwhile, due to the current technology, most designs using graphene suffer three major barriers. First, the practicable method for tuning chemical potential needs to be figured out. Second, the high difficulty and cost of graphene fabrication are frequently unavoidable. Third, the excellent controlling feature on graphene can only be applied in Terahertz band, which means that there is an obvious limitation of graphene in the low frequency applications.

To overcome above-mentioned limitation on controlling function, a design of tunable metasurface using few-layer has be reported. This proposed metasurface contains multiple layers comparing with conventional singe-layer metasureface. Due to the strong coupling between layers, the energy can be strongly redistributed in this novel metasurface. As a result, this few-layer metasurface can provide more degrees of freedom for amplitude/magnitude manipulation and achieve a phase control simultaneously. A few research achievements based on few-layer metasurface have been presented recently, showing the high performance of controlling on light processing. However, all of them are passive structure, leading the un-dynamical controlling function. Therefore, to realize dynamic phase and amplitude control with broad available range, more novel designs of metasurface need to be proposed.

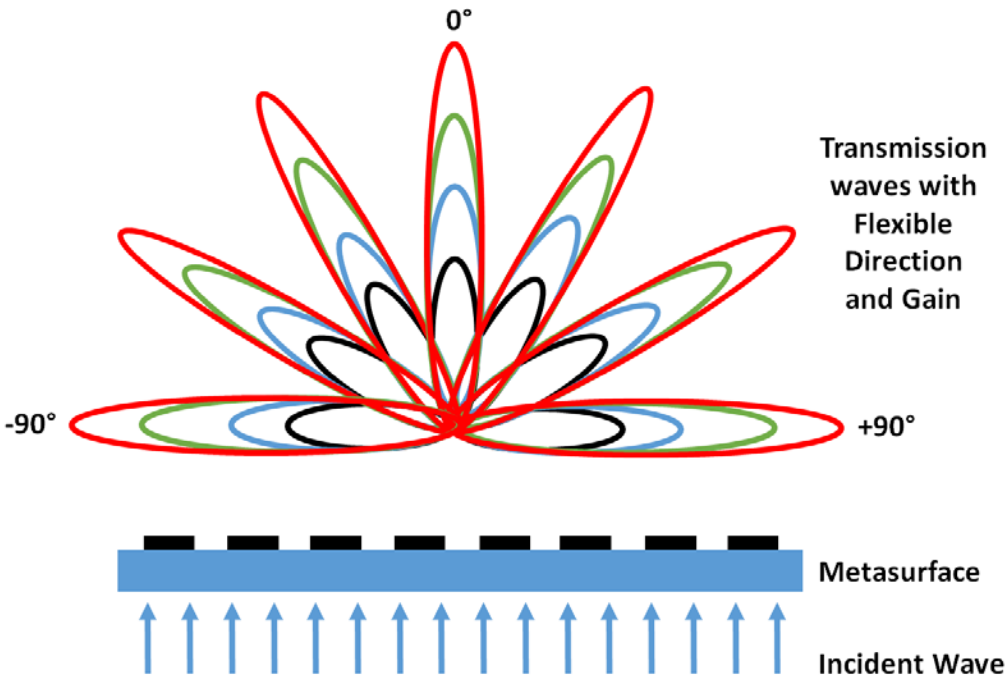

Figure 7.1: Schematic of the proposed metasurface for dynamically controlling the direction and gain of the transmission wave.

An experimental tunable metasurface with the capability to simultaneously control both the phase and amplitude of electromagnetic waves to a large dynamic range is designed and demonstrated. By integrating the high controllability of few-layer metasurface with externally tunable elements, the independently full control on phase and amplitude can be easily achieved (as shown in Fig. 7.1). The simulation of proposed metasurface exhibits full 360° phase control and a wide range amplitude control on the transmission wave. To verify our design concept, a metasurface with one array of three unit cells is fabricated and measured at 5.8 GHz. The measurement results provide a full range of transmission phase tuning (360°) and a wide ratio of normalized transmission amplitude tuning (1/16). Both simulation and measurement make an agreement with our design concept. Our design will take the metasurface research to new heights and extend the potentials for fast, real-time, and flexible electromagnetic wave manipulation.

7.2 Proposed Designs

In our design concept, the proposed few-layer metasurface consists of phase control part and amplitude control part. Both of them are constituted by several single-layer metasurfaces. For dynamical control function, the tunable elements, varactor diodes are loaded into the phase and amplitude control part. In next two sections, the equivalent circuit analysis for each control part and the corresponding simulation results are presented respectively. The closed-form expressions for the relations between the phase/amplitude and the tunable capacitance of varactor diodes are derived by the scattering parameters (*S*-parameters). A transfer matrix (*ABCD*-matrix) approach is applied to solve the scattering parameters of the structure. In third section, phase and amplitude control parts are integrated to compose the proposed electrically tunable metasurface. The simulation of the few-layer metasurface is shown to verify the dynamical phase and amplitude control can be realized by adjusting the capacitance of the varactor diodes.

7.2.1 Phase Control Part

To realize full 360° phase tuning range, one common approach is to design multiple resonators. It is well known that the available range of tuned phase directly depends on the total number of realized resonators. More resonators can more easily achieve wide phase range. In metasurface theory, increasing number of resonators will cause more layers or larger physical size. These phenomena usually have the ripple reaction of making more loss. As a result, the variation of amplitude can be huge, and it will be meaningless for phase control. In our design, the function of phase control part is

to achieve complete phase tuning (360°), regardless of the variation of amplitude. Based on this requirement, total three resonators are chosen. Fig. 7.2 schematically depicts the structure of phase control part in three-dimension view [195]. The structure consists of two square patch sheets and a ground plane spaced by two substrates. From Fig. 7.2, two square patch sheets are located at the top and bottom of the whole part respectively. In the center of each square patch, there is a gap to insert two tunable varactor C_1. These two square patch sheets can be modeled as two resonators using shunt LC circuit. Between two substrates, one ground plane is employed for third resonator. This ground plane contains upper ground and lower ground separated by a thin-film. In the lower ground, a slot is set at the center the ground (it is also centered with the square patch sheet), and one varactor C_2 is inserted to connect two sides of the slot. Due to varactor tuned by external DC voltage, a slight loop slot is drawn to split the ground for the bias line. However, this bias line will break the continuity of slot's edge. It will inevitably influence the behavior of third resonator. For this reason, additional upper ground is designed to maintain electrically continuous slot. Since the practical varactor diode has physical height, an appropriate square slot is need in the upper ground. Moreover, a thin-film is necessary to separate upper and lower ground and provide DC isolation for biasing varactor diode. In our design, Rogers 3001 bonding film with thickness 0.04 mm is used as the thin-film. Based on the thin thickness, this thin-film can be ignored in the equivalent circuit analysis.

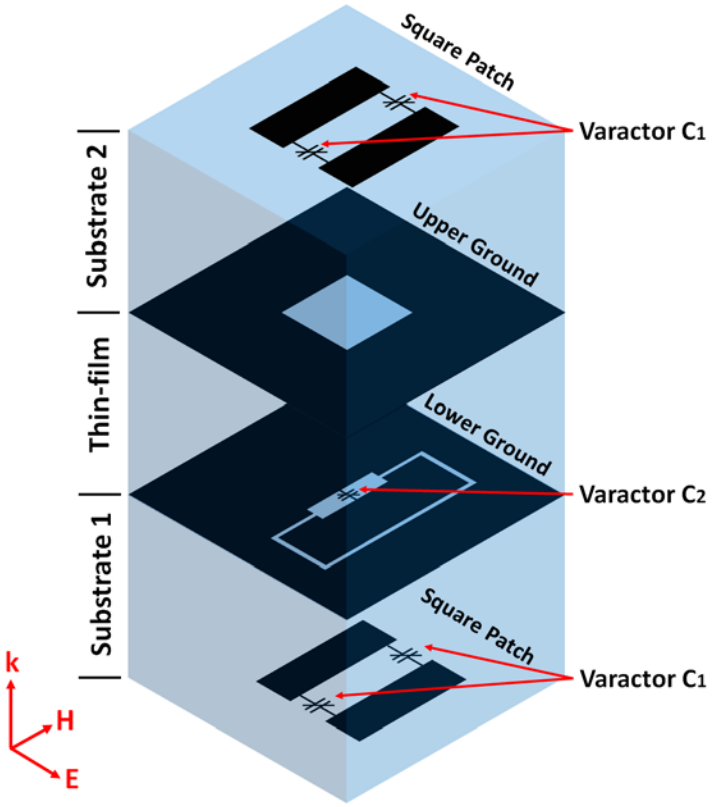

Figure 7.2: Schematic structure of the phase control part in 3D view.

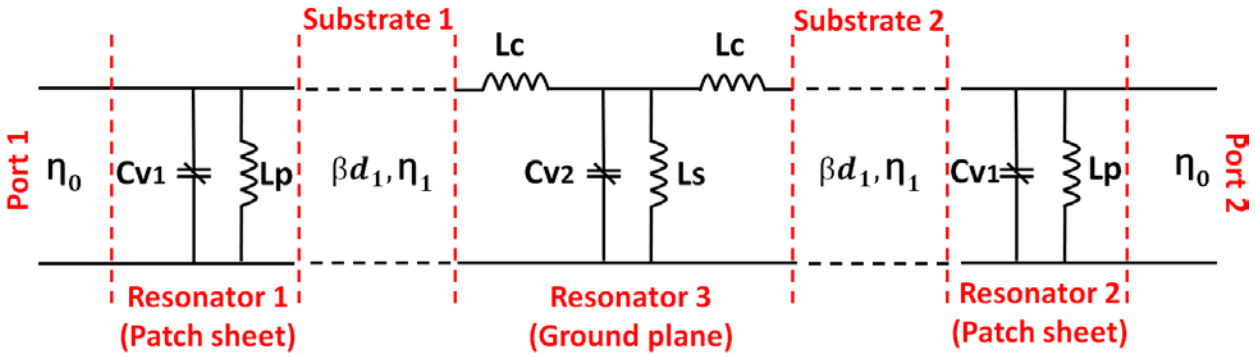

Figure 7.3: Equivalent circuit model of the phase control part (Port 1 is input port, and Port 2 is output port).

Fig. 7.3 shows the equivalent circuit model of the phase control part. Port 1 and 2 are the free-space port with wave impedance (η_0 = 377Ω). Along the direction of wave propagation (from Port 1 to Port 2), there are total five sections composing the circuit

model of the phase control part. For two patch sheets, they are modeled as a resonator with shunt LC circuit (shown as Resonator 1 and 2 in Fig. 3) [196]. Parameter C_{v1} is the total capacitance within the gap of the patch sheet:

$$C_{v1} = 2 \times C_1 + C_p \tag{7.1}$$

where C_1 is the capacitance of varactor, and C_p is the inherent capacitance in the gap of patch sheet. Parameter L_p is the inductance of the metallic sheet. From Resonator 3 in Fig. 7.3, the slot in the ground plane can be equivalent to a T-shape circuit with one shunt inductor L_s and two series inductors L_c [197]. The shunt capacitance C_{v2} is the total capacitance in the slot:

$$C_{v2} = C_2 + C_s \tag{7.2}$$

where C_2 is the capacitance of varactor inserted in the slot, and C_s is the inherent capacitance in the slot. For Substrate 1 and 2, they can be modeled as transmission line with intrinsic impedance η_1 and electrical length βd_1 (β is the wavenumber and d_1 is the thickness of substrate). For convenient implication, We set Substrate 1 and 2 have the identical characteristics and thickness. To develop the scattering parameters (*S*-parameters) on the phase control part, a transfer matrix (*ABCD*-matrix) of the whole equivalent circuit is derived as following:

$$\begin{bmatrix} A & B \\ C & D \end{bmatrix}_{pha}$$

$$= \begin{bmatrix} 1 & 0 \\ j[\omega C_{v1} - 1/(\omega L_p)] & 1 \end{bmatrix} \begin{bmatrix} \cos\beta d_1 & j\eta_1 \sin\beta d_1 \\ j\sin\beta d_1 / \eta_1 & \cos\beta d_1 \end{bmatrix} \begin{bmatrix} 1 & j\omega L_c \\ 0 & 1 \end{bmatrix} \begin{bmatrix} 1 & 0 \\ j[\omega C_{v2} - 1/(\omega L_s)] & 1 \end{bmatrix}$$

$$\begin{bmatrix} 1 & j\omega L_c \\ 0 & 1 \end{bmatrix} \begin{bmatrix} \cos\beta d_1 & j\eta_1 \sin\beta d_1 \\ j\sin\beta d_1 / \eta_1 & \cos\beta d_1 \end{bmatrix} \begin{bmatrix} 1 & 0 \\ j[\omega C_{v1} - 1/(\omega L_p)] & 1 \end{bmatrix} \tag{7.3}$$

where ω is operating radian frequency. The transmission coefficient (S_{21}) on the phase control part can then be related to the *ABCD*-matrix of the corresponding circuit model:

$$S_{21} = \frac{2}{A + B/\eta_0 + C\eta_0 + D} \tag{7.4}$$

According to Eqn. 7.4, the phase and amplitude response of transmission wave can be obtained.

In the simulation of the phase control part, we set the operating frequency range is from 5 GHz to 6 GHz. For the square patch sheet, the dimension is 13 mm × 13 mm, and the width of gap is 1 mm. The size of the ground plane is 30 mm × 30 mm. In the lower ground, the size of slot is 5 mm × 3 mm, and the loop slot is drawn with 0.4 mm width and 20 mm × 8 mm inside dimension. For substrates, we use Rogers Duroid 6002 with 2.94 dielectric constant and 3 mm thickness. The capacitance range of varactor C_1 and C_2 is set to 0.1-1 pF and 0.1-0.5 pF, respectively. Fig. 7.4 shows the simulation results of the amplitude and phase response. From Fig. 7.4(b), by tuning the capacitance of varactors, the phase of transmission wave can be fully tuned between -173° and +177° at 5.8 GHz. However, from Fig. 7.4(a), even few three resonators are designed in the phase control part, the amplitude appears a sizable variation (almost from 0 to 1). It is clear that the amplitude completely depends on the tuned value of the phase. To realize independent control on phase and amplitude simultaneously, several additional layers focusing on the amplitude control are designed and cascaded with the phase control part. The proposed amplitude control part is introduced in the next section.

7.2.2 Amplitude Control Part

The three-dimension schematic diagram of the proposed amplitude control part is shown in Fig. 7.5. Two identical square loops with embedded patch are laid on the top and bottom sides of the substrate. Between square loop and embedded patch, two tunable varactors C_3 are inserted in the E-field axis. Total four varactors are applied for dynamically controlling the amplitude of the transmission wave. The double-side layout can increase the maximum level of amplitude tuning range. The equivalent circuit of the amplitude control part consists of multiple cascaded sheet admittances (as shown in Fig. 7.6). For the transverse electrical (TE) excitation, parameter L_m can represent the inductance of the loop section along the E-field axis. The embedded patch is simply analyzed as a shunt LC circuit with capacitance C_n and inductance L_n. Parameter C_{v3} is the total capacitance between square loop and patch:

$$C_{v3} = C_3 + C_l \tag{7.5}$$

where C_3 is the capacitance of varactor inserted between square loop and patch, and C_l is the inherent capacitance in the square loop. Between two metallic layers, a substrate with thickness d_3 can be modeled as transmission line with intrinsic impedance $\eta_3$and electrical length βd_3. Following the same method in phase control part, the *ABCD*-matrix of the amplitude control part is derived:

$$\begin{bmatrix} A & B \\ C & D \end{bmatrix}_{amp} = \begin{bmatrix} 1 & 0 \\ jY & 1 \end{bmatrix} \begin{bmatrix} \cos\beta d_3 & j\eta_1 \sin\beta d_3 \\ j\sin\beta d_3 / \eta_3 & \cos\beta d_3 \end{bmatrix} \begin{bmatrix} 1 & 0 \\ jY & 1 \end{bmatrix} \tag{7.6}$$

where $= \frac{1}{\frac{2}{\omega C_{v3}} + \frac{1}{\omega C_n - \frac{1}{\omega L_n}}} - \frac{2}{\omega L_m}$. Then, the transmission coefficient (S_{21}) on the amplitude control part can be obtained by using Eqn. 7.4.

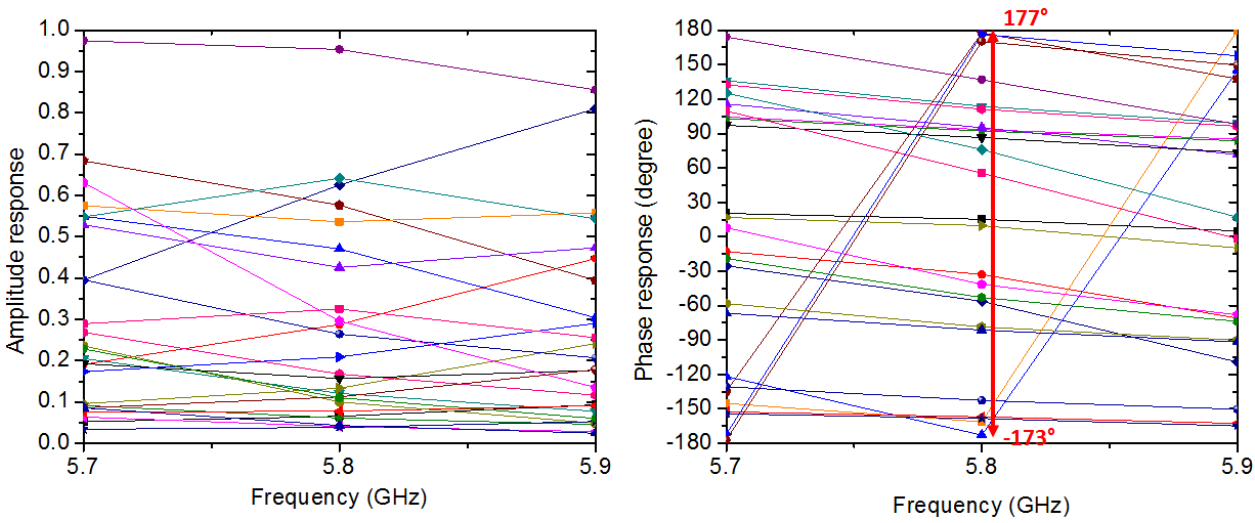

(a) (b)

Figure 7.4: Simulation results of the phase control part: (a) amplitude response and (b) phase response.

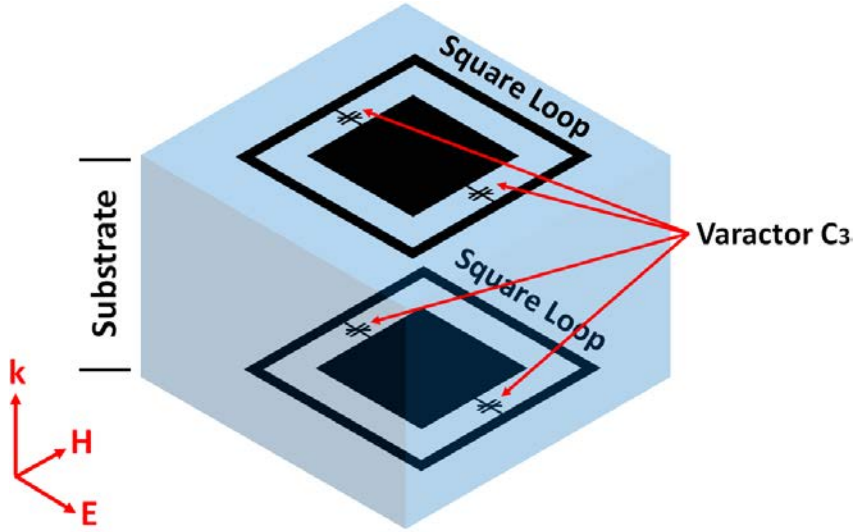

Figure 7.5: Schematic structure of the amplitude control part in 3D view.

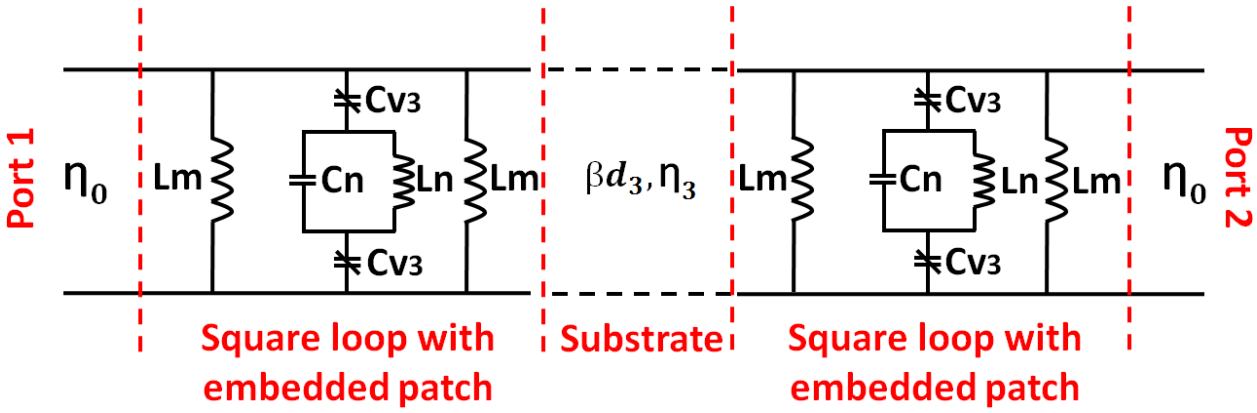

Figure 7.6: Equivalent circuit model of the amplitude control part (Port 1 is input port, and Port 2 is output port).

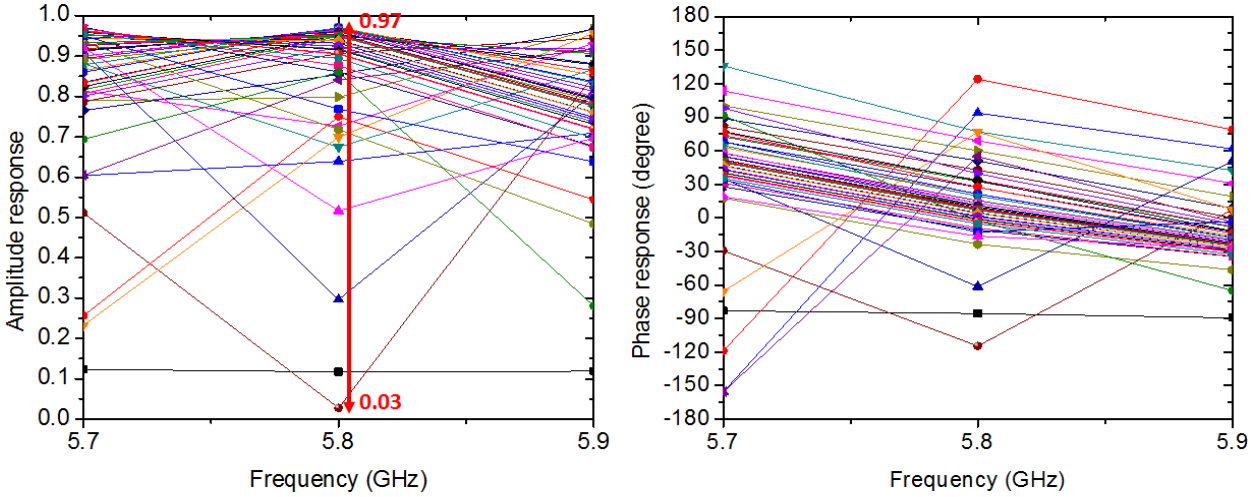

(a) (b)

Figure 7.7: Simulation results of the amplitude control part: (a) amplitude response and (b) phase response.

For the simulation of the amplitude control part, we set the width of square loop is 1 mm and the inside dimension is 23 mm × 23 mm, while the size of embedded patch is 20 mm × 20 mm. The substrate uses Rogers Duroid 5880 with 2.2 dielectric constant and 3.15 mm thickness. The varactor C_3 can be tuned from 1 pF to 10 pF. The simulation results are presented in Fig. 7.7. For the amplitude response, the value can vary between 0.03 and 0.97 at 5.8 GHz, leading a wide range of amplitude control (as shown in Fig.

7.7(a)). Meanwhile, Fig. 7.7(b) exhibits that the phase is held within a narrow range at the same frequency, which is from -110° to +120° (less than 64% of the full phase range). Therefore, we can conclude that the proposed amplitude control part can achieve a wide tenability on the amplitude and constrict the phase's variation into a small fraction.

7.2.3 Tunable Metasurface

In our design, the few-layer metasurface is composed of the phase and amplitude control parts. Based on the simulation results mentioned in last two sections, it is available to realize independent control on phase and amplitude by integrating phase and amplitude control parts. The final schematic of unit cell in the few-layer metasurface is illustrated in Fig. 7.8(a). An air gap with thickness d_2 = 5 mm is inserted between the phase and amplitude control part for avoiding overlap. The final *ABCD*-matrix for the proposed few-layer metasurface is summarized as following:

$$\begin{bmatrix} A & B \\ C & D \end{bmatrix}_{total} = \begin{bmatrix} A & B \\ C & D \end{bmatrix}_{pha} \begin{bmatrix} \cos\beta d_2 & j\eta_1 \sin\beta d_2 \\ \dfrac{j\sin\beta d_2}{\eta_0} & \cos\beta d_2 \end{bmatrix} \begin{bmatrix} A & B \\ C & D \end{bmatrix}_{amp} \tag{7.7}$$

The simulation of few-layer metasurface is obtained by ANSYS HFSS. From Fig. 7.8(a), Wave Port 1 and 2 are used as input/output port, and one unit cell of metasurface with PEC-PMC boundaries can be equivalent to the infinite array (the same simulation setup is also applied for the individual phase and amplitude control part). As a result, the proposed metasurface in an infinite array can manipulate the electromagnetic wave on phase and amplitude by adjusting the bias voltage fed on each cell (as shown in Fig. 7.8(b)). To exhibit the independently and simultaneously full control on phase and amplitude, the simulation results at 5.8 GHz of the proposed metasurface are classified

into two types. The first type is tuning amplitude with a fixed phase response. Fig. 7.9 shows the simulation results of tuning amplitude from 0 to 0.8 with phase is equal to -140°. In another example, Fig. 7.10 illustrates the simulation results for tuning amplitude between 0 and 0.8 with +70° fixed phase. Fig. 7.11 and 7.12 show the second type of full phase control with a fixed amplitude. One group generates 360° phase tuning with 0.6 amplitudes in Figure 7.11, and another one shows the same phase tuning with 0.3 amplitudes in Figure 7.12. For all simulation data, we set the acceptable tolerance is ±5° for phase and ±0.05 for amplitude. All above groups of simulations exhibit that the proposed tunable metasurface has the capability of independently and simultaneously tuning both the phase and amplitude of transmission wave.

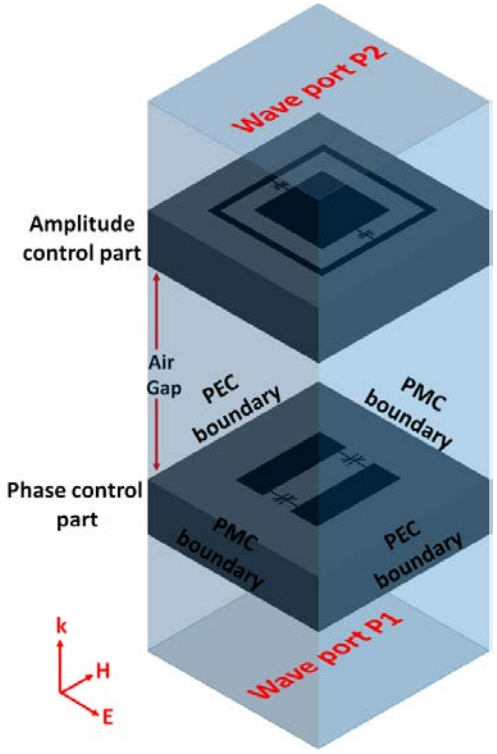

(a)

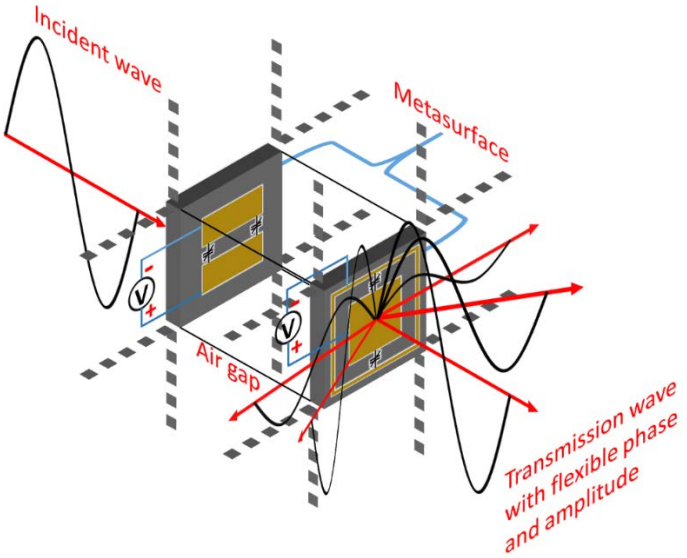

(b)

Figure 7.8: (a) Schematic structure and simulation setup of the proposed metasurface including the phase and amplitude control parts (in 3D view); (b) Schematic diagram of simultaneously controlling both the phase and amplitude of incident wave using the proposed metasurface.

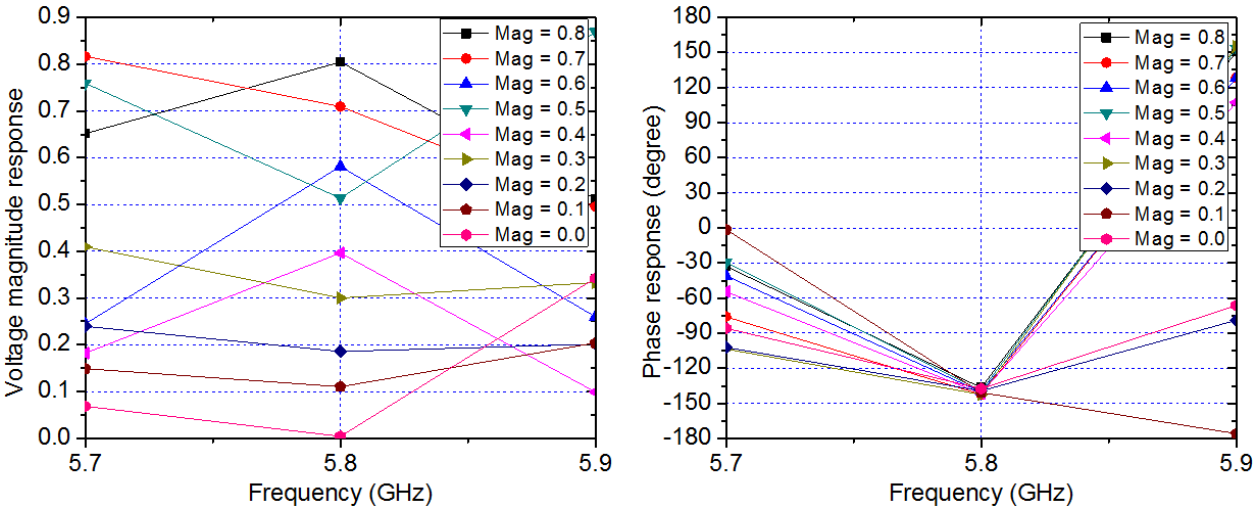

(a) (b)

Figure 7.9: Simulation results of the proposed metasurface realizing tuning amplitude and constant -140° phase: (a) amplitude response and (b) phase response.

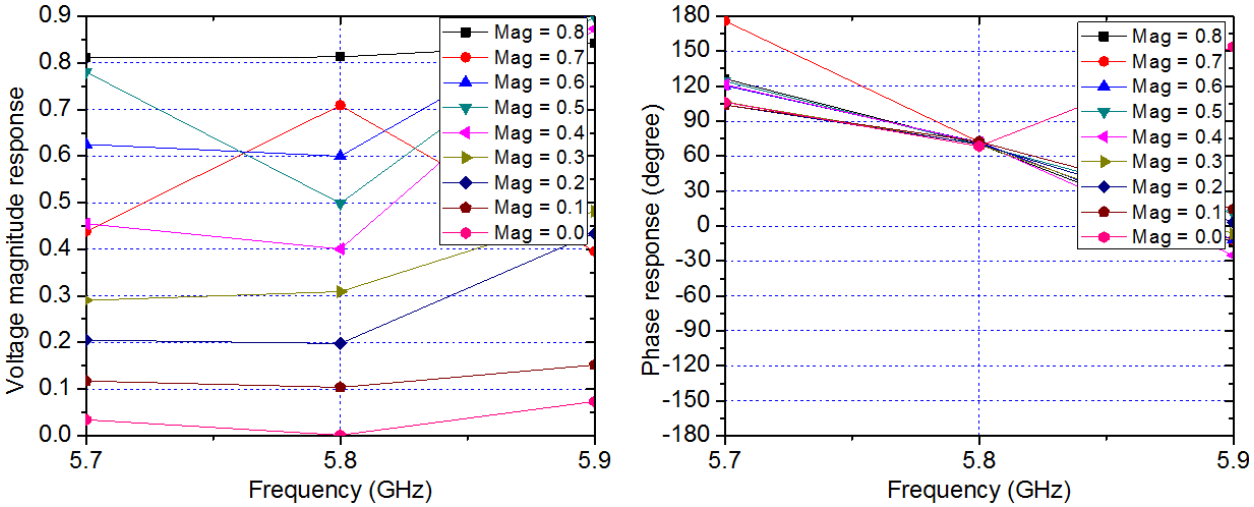

(a) (b)

Figure 7.10: Simulation results of the proposed metasurface realizing tuning amplitude and constant +70° phase: (a) amplitude response and (b) phase response.

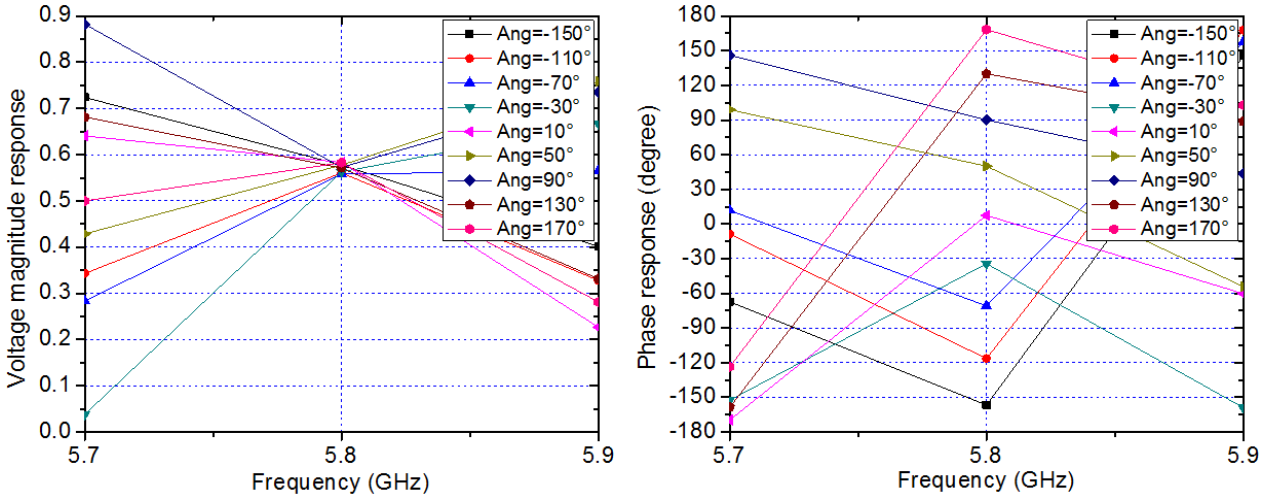

(a) (b)

Figure 7.11: Simulation results of the proposed metasurface realizing tuning phase and fixing amplitude around 0.6: (a) amplitude response and (b) phase response.

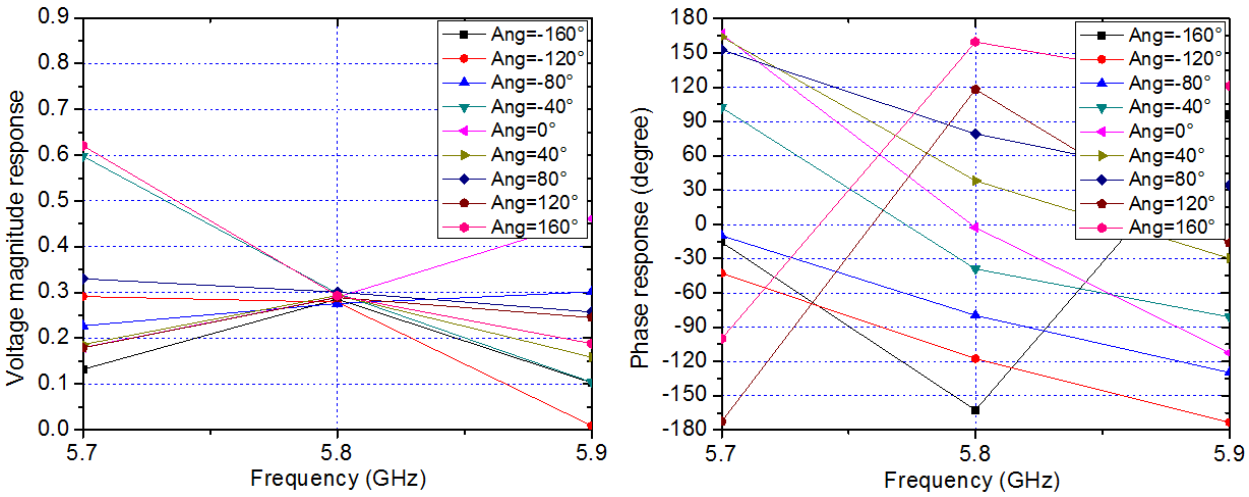

(a) (b)

Figure 7.12: Simulation results of the proposed metasurface realizing tuning phase and fixing amplitude around 0.3: (a) amplitude response and (b) phase response.

7.3 Experimental Verification

To verify our design concept, the proposed metasurface is fabricated to one row of three unit cells for the experimental measurement. Fig. 7.13(a)-(c) illustrate the fabricated square patch layer, lower ground layer, and square loop layer, respectively. To feed DC voltage to varactor diodes, the bias lines are applied for each layer. The width of bias lines is very thin for minimize the undesired effect on the metasurface. The AC blocks are also needed to avoid the energy lost into the DC voltage source. In our experiment, MA46H201-1088 is used for varactor C_1 and C_2, and varactor C_3 employs NXP-BB181. For AC block, we choose Coilcraft 0403HQ-9N0XJLU inductor, which can support the high frequency. The measurement setup diagram and photograph are shown in Fig. 7.14. From Fig. 7.14(a), one transverse EM (TEM) cell is used as the measurement tool to install the metasurface. TEM cell can generate electromagnetic wave with 377Ω in transverse mode, providing the same characteristics with the plane wave in free space [198]. In our experiment, the TEM cell are constituted by a conducting metallic strip and

a ground plane (as shown in Fig. 7.14(b)). By prior simulation of TEM, the optimized dimension is obtained to match the feed cable at the input/output ports. To ensure the incident wave can completely pass through the metasurface, the width of conducting metallic strip is set which as wide as the fabricated row of three unit cells. Three DC voltage sources are used to support three different varactor diodes (C_1, C_2 and C_3). In the data measurement, the transmitted wave of the metasurface is measured by the vector network. The TEM cell without metasurface is also tested, and the recorded value is used as the reference data for the analysis of amplitude control. In the measurement, the operating frequency is detected at 6.03 GHz for the dynamic control of phase and amplitude on the transmission line. Comparing with simulation results, a frequency shift occurred due to the fabrication tolerance and the parasitic inductance in the varactor diodes. Based on the measurement data, the phase tuning can complete the full range of 360°, while the measured value of the amplitude can be tuned within 0.025 to 0.4. The decreased tuning range of amplitude control depends on the energy loss in TEM cell. From Fig. 7.14(b), the surrounding environment of the TEM cell is not ideal. Due to the open structure of the TEM cell, a sizeable amount of energy can be absorbed by non-DUT objects (such as, metallic sheets on the DC voltage source or metallic clip on cables). Regardless of the undesired energy loss, the proposed metasurface achieves the independent control of phase and amplitude by tuning external DC voltages. Fig. 7.15 lists the values of biasing DC voltages for realizing the flexible combination of phase and amplitude on the transmission line. From these 3D bars figures, it is clear that, within the tuning range of phase (360°) and amplitude (0.025 - 0.4), random couple of phase and amplitude can derive the corresponding values of DC voltages for three different varactor

diodes. To prove the independent control of phase and amplitude, several special measured functions are provided in Fig. 7.16 - 7.18. Fig. 7.16 shows the measurement results of tuning amplitude while the phase response is fixed to +60°.

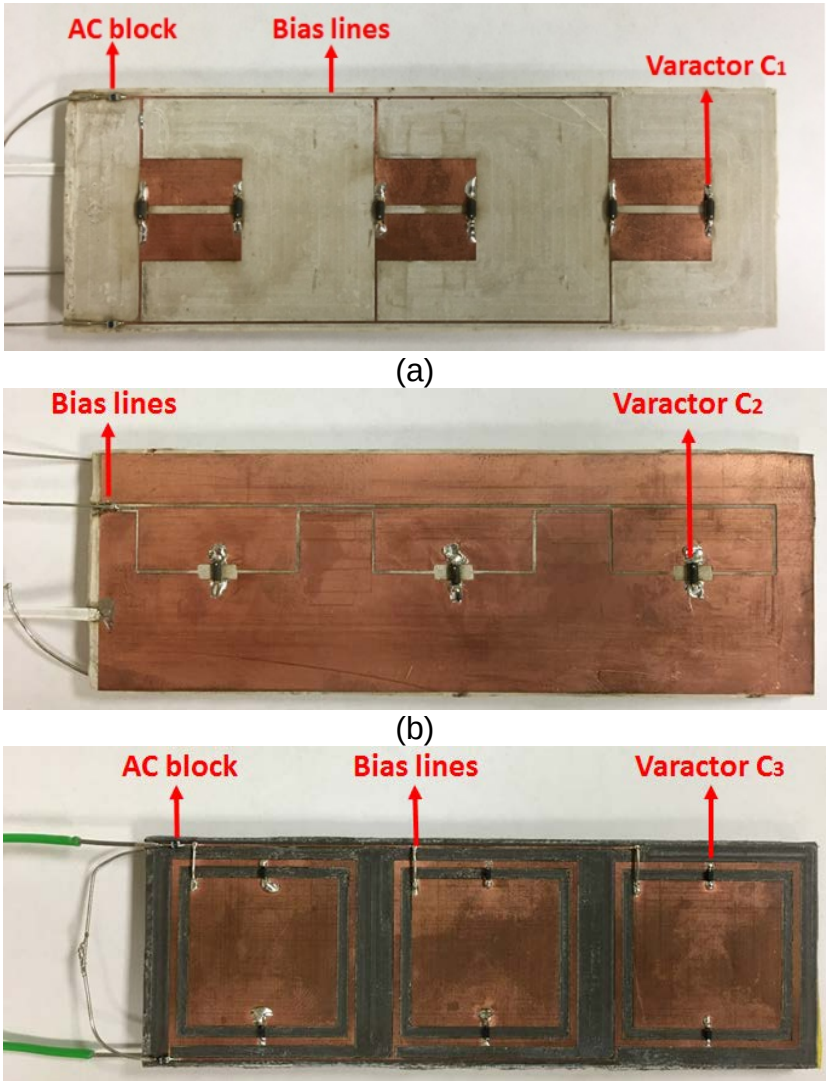

Figure 7.13: Photographs of the fabricated layers including three unit cells: (a) square patch layer, (b) lower ground layer, and (c) square loop layer.

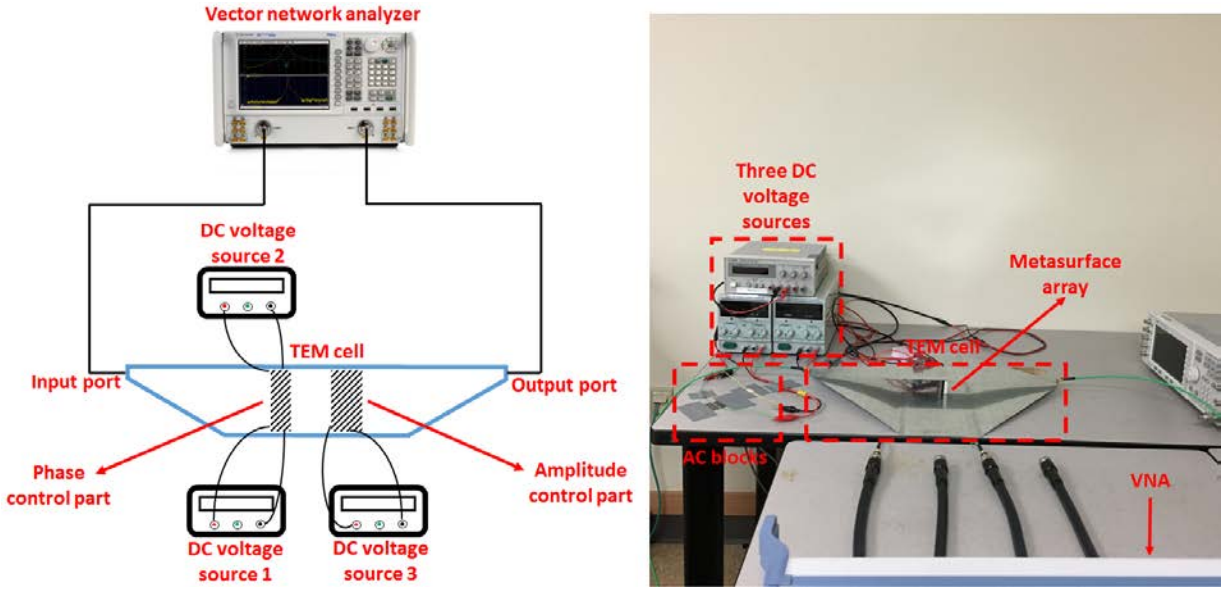

(a) (b)

Figure 7.14: (a) Schematic of measurement setup for the proposed metasurface and (b) photograph of the experiment.

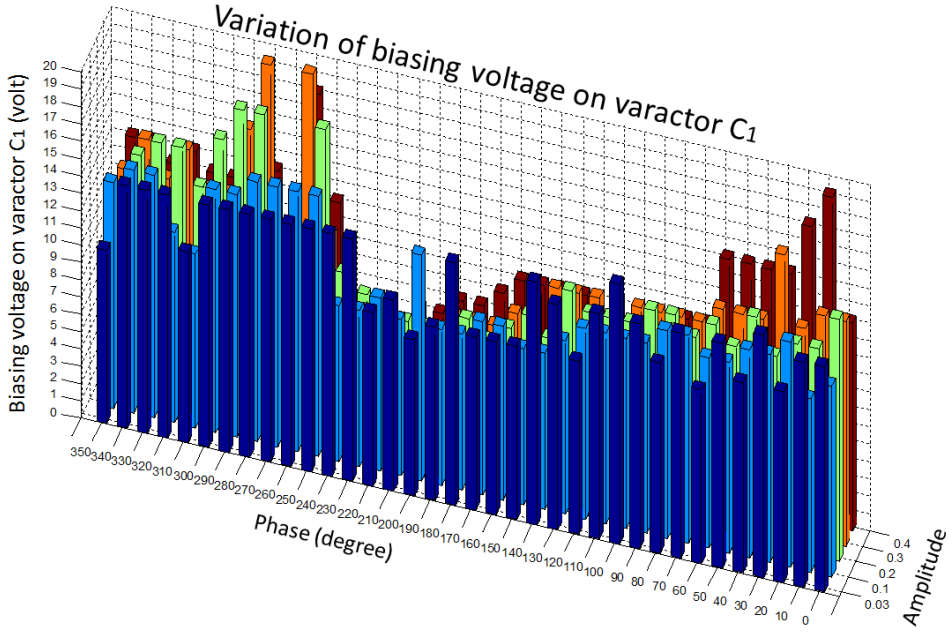

(a)

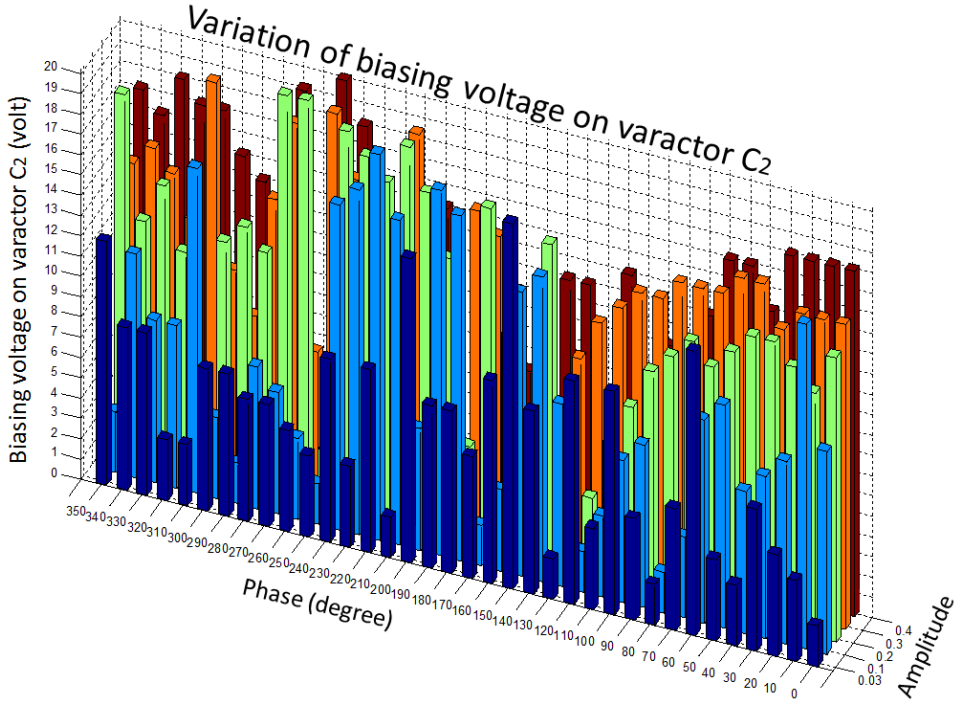

(b)

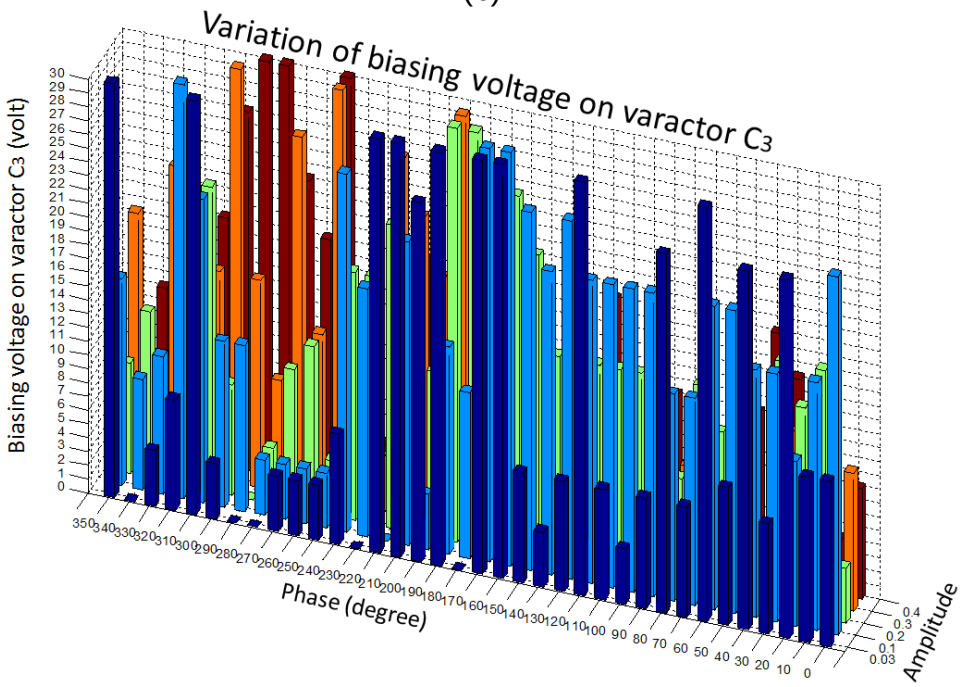

(c)

Figure 7.15: 3D bars illustrate the variation of biasing voltages on (a) varacotr C_1, (b) varacotr C_2, and varacotr C_3 for achieving the independent phase and amplitude control.

he curves of measured phase and amplitude responses are plotted in Fig. 7.16(a) and 7.16(b) respectively. Table 7.1 illustrates the values of all three DC voltages for couples of constant phase and different amplitude. The measurement margin is set to ±5° for phase and ±0.05 for amplitude. Another case of tuning amplitude with -160° phase response is shown in Fig. 7.17, and Table 7.2 provides the values of DC voltages for different amplitude level. About tuning phase with constant amplitude, the measurement results of a corresponding case are shown in Fig. 7.18. In Fig. 7.18(b), it is obvious that the value of phase response is tuned between -180° and +180° at 6.03 GHz, achieving a full phase control. Fig. 7.18(a) exhibits the curves of amplitude responses under different phase values, and the variation of the amplitude response is hold within 0.3±0.05 at 6.03 GHz. Table 7.3 shows the values of all DC voltages for couples of different phase levels and constant amplitude. To further demonstrate the flexibility of the proposed metasurface, an implementation of the phased array consisting of four metasurface cells with the identical magnitude and progressive phase response is designed to steering the normal incident wave (as shown in Fig. 7.19). In Fig. 7.19(a), each metasurface cell generates 0.5 magnitude, and the phase difference between two adjacent cells is -90°. Based on the Snell's law of refraction, the angle of refracted wave is +15°. Another refraction angle -29° can be achieved by adjusting the metasurface cells to obtain the 0.65 magnitude and the phase difference +180°. In general, we believe that the flexibility of the proposed metasurface makes the promise for device manipulation of electromagnetic waves, leading the potential of a wide range of applications.

Table 7.1

The values of all three DC voltages for couples of constant +60° phase and different amplitude

Power Magnitude (±0.05)	Phase Response (degree) (±5°)	DC Voltage Biased on C1 (V)	DC Voltage Biased on C2 (V)	DC Voltage Biased on C3 (V)
0.4	+60°	12	15	26
0.3	+60°	12	10	30
0.2	+60°	16	12	8
0.1	+60°	14	4	12
0.025	+60°	14	7	4

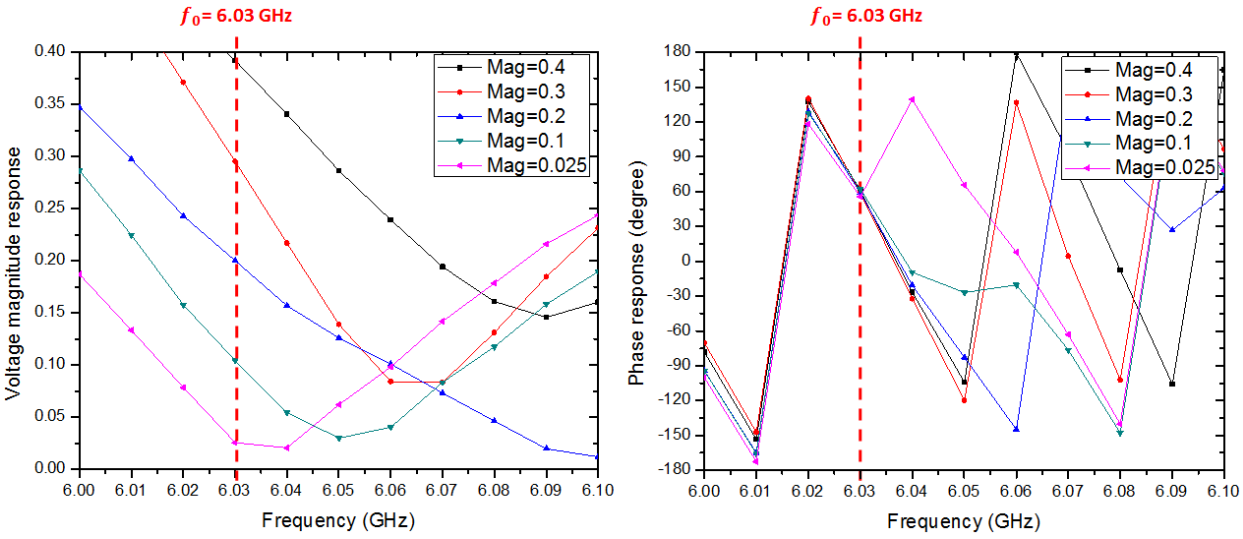

(a) (b)

Figure 7.16: Measurement results of the proposed metasurface realizing tuning amplitude and constant +60° phase: (a) amplitude response and (b) phase response.

Table 7.2

The values of all three DC voltages for couples of constant -160° phase and different amplitude

Power Magnitude (±0.05)	Phase Response (degree) (±5°)	DC Voltage Biased on C1 (V)	DC Voltage Biased on C2 (V)	DC Voltage Biased on C3 (V)
0.4	-160°	10	8	10
0.3	-160°	9	11	22
0.2	-160°	9	11	26
0.1	-160°	10	4	30
0.025	-160°	10	10	30

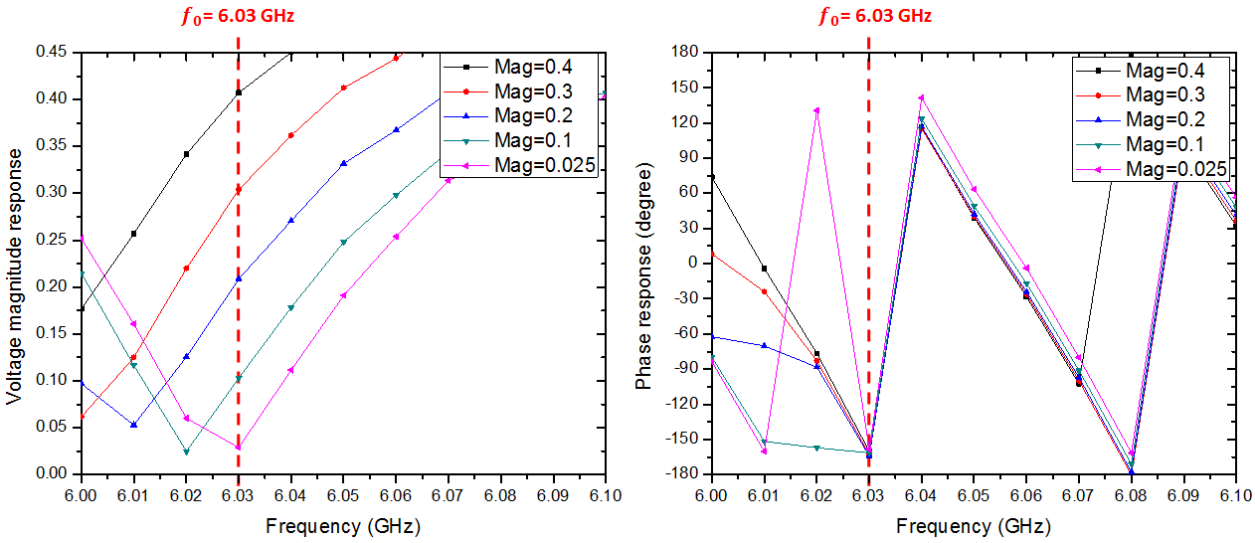

(a) (b)

Figure 7.17: Measurement results of the proposed metasurface realizing tuning amplitude and constant -160° phase: (a) amplitude response and (b) phase response.

Table 7.3

The values of all three DC voltages for couples with 0.3 amplitude and different phase

Power Magnitude (±0.05)	Phase Response (degree) (±5°)	DC Voltage Biased on C1 (V)	DC Voltage Biased on C2 (V)	DC Voltage Biased on C3 (V)
0.3	0	13	15	10
0.3	-20	12	15	12
0.3	-40	12	16	4
0.3	-60	12	15	4
0.3	-80	11	15	8
0.3	-100	11	14	8
0.3	-120	11	12	8
0.3	-140	11	6	8
0.3	-160	9	11	22
0.3	+180	8	16	12
0.3	+160	7	16	18
0.3	+140	6	13	26
0.3	+120	2	16	10
0.3	+100	20	7	12
0.3	+80	20	14	8
0.3	+60	12	10	30
0.3	+40	14	12	15
0.3	+20	14	15	8

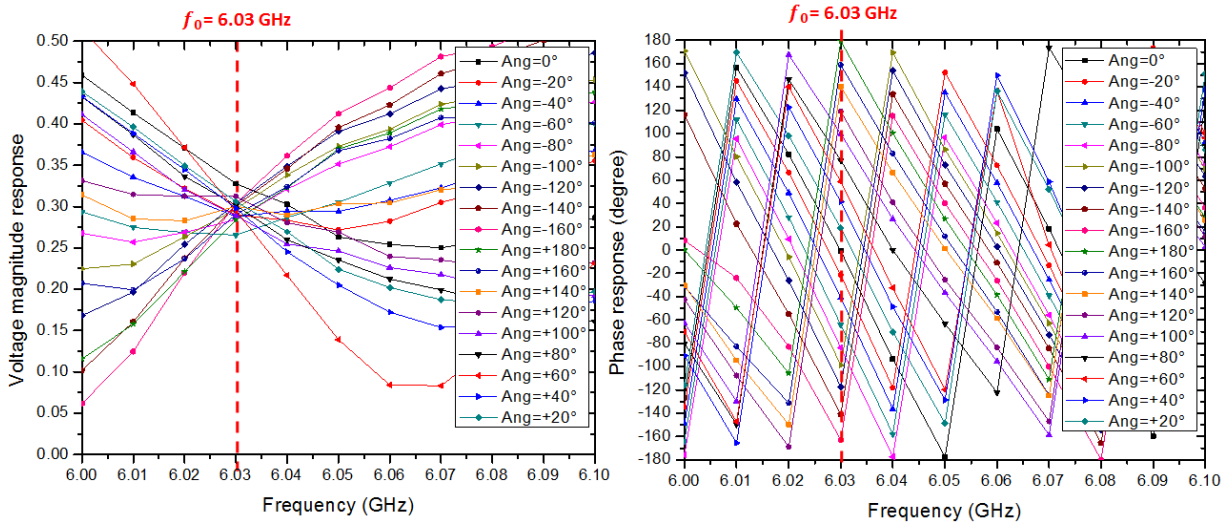

(a) (b)

Figure 7.18: Measurement results of the proposed metasurface realizing tuning phase and fixing amplitude around 0.3: (a) amplitude response and (b) phase response.

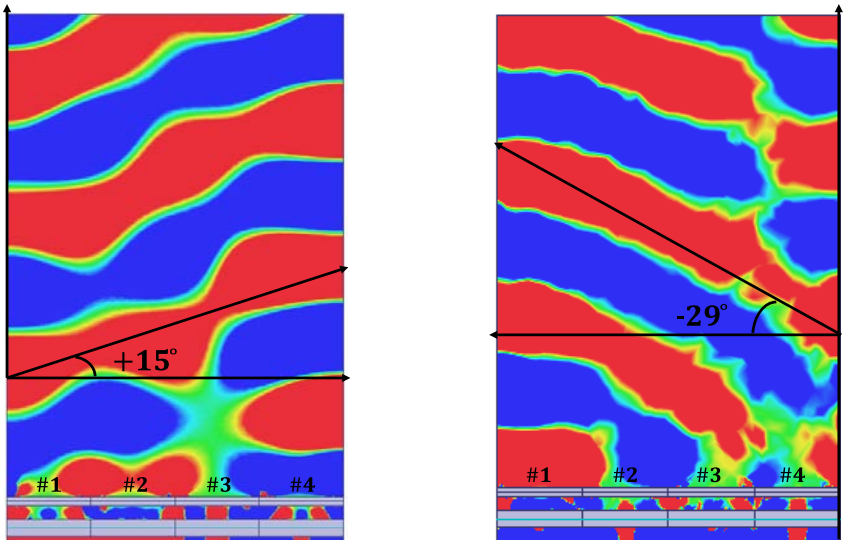

(a) (b)

Figure 7.19: The simulations of two phased arrays consist of four proposed metasurface cells with the identical magnitude and progressive phase response to realize the refracted wave with different angles: (a) +15° and (b) -29°.

7.4 Conclusion and Future Work

A design of few-layer metasurface with active components is realized to simultaneously control the phase and amplitude of electromagnetic waves in a large

dynamic range. The simulation of proposed metasurface shows full 360° phase control and a wide range amplitude control. To verify the proposed design theory, an experiment is implemented. From the measurement results, phase control achieves a full range while a decreased tuning range is obtained on amplitude control. To address this issue, the future work will apply single power amplifier (PA) and variable gain amplifier (VGA) to compensate the energy loss and improve the amplitude tuning scales. Fig. 7.20 and 7.21 show the prophase test about PA and VGA respectively. The PA applies HMC476MP86 with 10 dB gain, and the VGA applies MAAM-011100 with 29 dB range (from +8 dB to -21 dB). The next step is to integrate PA/VGA with the previous metasurface for the measurement.

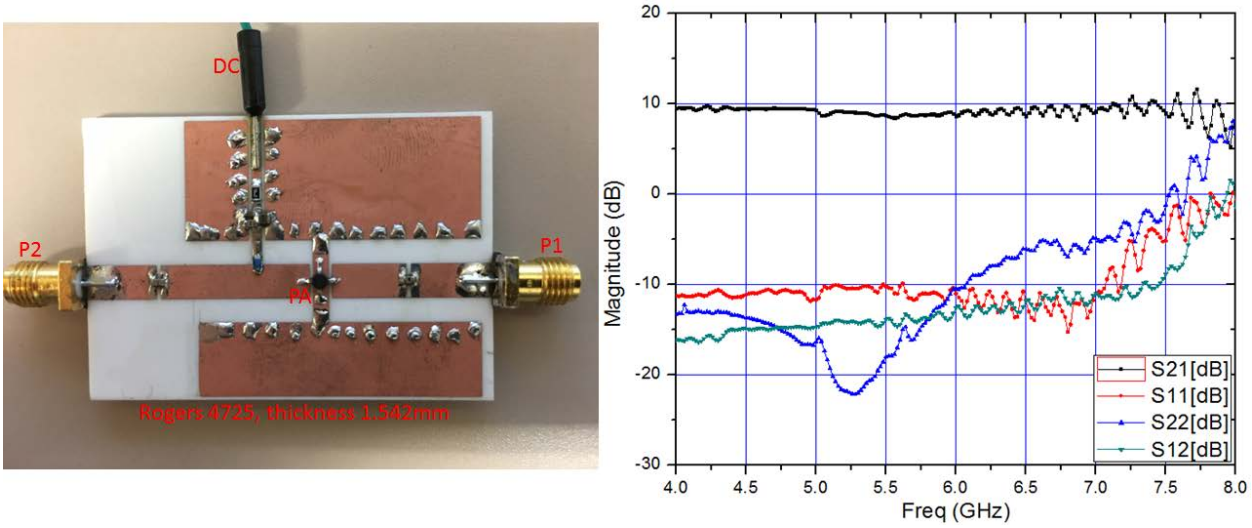

(a) (b)

Figure 7.20: (a) Photograph of the PA test circuit and (b) the measurement results including gain (S_{21}), return loss (S_{11} and S_{22}), and isolation (S_{12}).

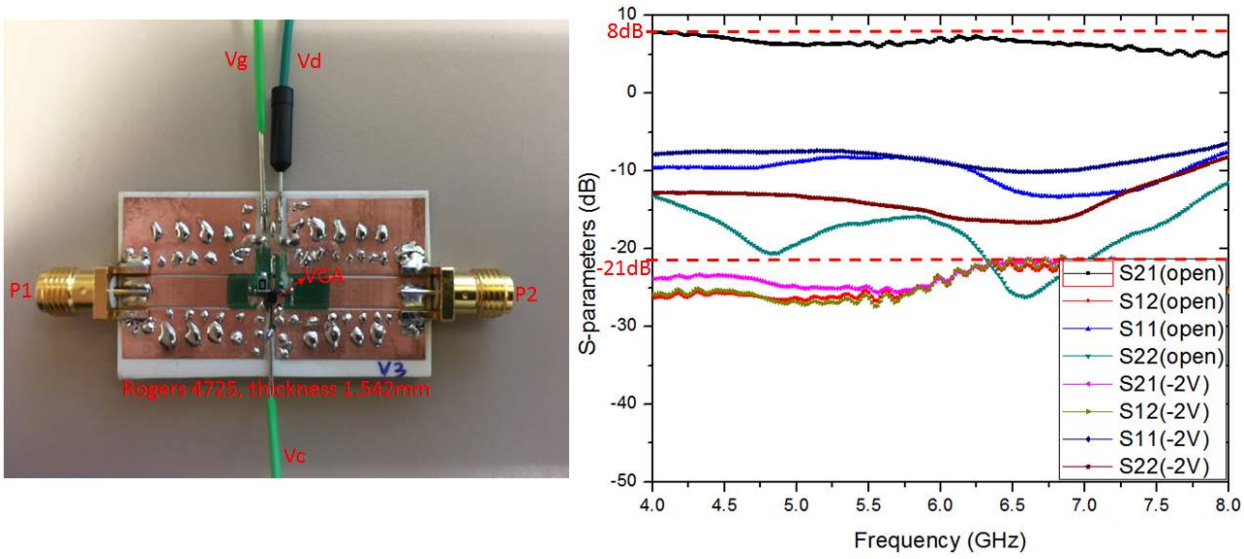

(a) (b)

Figure 7.21: (a) Photograph of the VGA test circuit and (b) the measurement results including gain (S_{21}), return loss (S_{11} and S_{22}), and isolation (S_{12}).

CHAPTER 8

CONCLUSION AND FUTURE WORK

In this dissertation, several novel approaches and designs for improving beam-forming systems were presented. First, the multi-band RF components were realized by using a novel multi-band transmission line to replace the conventional transmission line. In the proposed designs, dual-band and tri-band RF couplers were are designed and verified. The proposed multi-band RF couplers can be employed in the beam-forming system to extend the operating frequency bands. Moreover, a novel feeding network using Butler matrix topology with advanced couplers is realized to increase the radiation beam angles while the conventional Butler matrix only can generate four angles. The beam-forming systems using the proposed novel Butler matrix can generate a random radiation beam angle from -90° to +90°. To achieve a fully tunable transmission line, a graphene parallel-plate waveguide with T-type structure is presented. By adding the external biasing voltage, Graphene parallel-plate waveguide features, tunable propagation constant and characteristic impedance, leading full-scale tunability (e.g., tunable operating frequency, characteristic impedance, and electrical length). The proposed theory can realize the flexible tuning functions of the beam-forming systems in THz band. In the last project, we report a novel design of electrically tunable metasurface, which is able to dynamically control the phase and amplitude of the electromagnetic wave simultaneously. The proposed metasurface consists of two major parts: a phase control part with dominant phase tuning and an amplitude control part with dominant amplitude tuning.

In the future, in order to further improve the performance of beam-forming systems while maintaining a compact size, high efficiency, and high frequency band, the implementation of phased array antennas in the Integrated Circuits (ICs) in millimeter wave shows great potential for practical applications.

REFERENCES

[1] Y. Lo and S. Lee, *Antenna Handbook: Application*: Kluwer Academic Publishers, 1993.

[2] R. C. Hansen, *Phased Array Antennas*: Wiley-Interscience, 2009.

[3] D. Parker and D. C. Zimmermann, "Phased arrays – part 1: theory and architectures," *Microwave Theory and Techniques, IEEE Transactions on,* vol. 50, pp. 678-687, 2002.

[4] J. J. Yao, C. Lee, and S. P. Yeo, “Microstrip branch-line couplers for crossover application,” *IEEE Trans. Microw. Theory & Tech.,* vol. 59, no. 1, pp. 87-92, Jan. 2011.

[5] D. M. Pozar and D. H. Schaubert, “Comparision of three series fed microstrip array geometries,” in *Antennas and Propagation Society International Symposium, 1993. AP-S. Digest*, vol. 2, pp. 728-731, 1993.

[6] J. Butler and R. Howe, “Beamforming matrix simplifies design of electronically scanned antennas,” *Elec. Design*., vol. 9, no. 8, pp. 170-173, 1961.

[7] I. Lin, M. Vincentis, C. Caloz, and T. Itoh, “Arbitrary dual-band components using composite right/left-hand transmission lines,” *IEEE Trans. Microw. Theory Tech.*, vol. 52, no. 4, pp. 1142-1149, Apr. 2004.

[8] H. Zhang, Y. Peng, and H. Xin, “A tapped stepped-impedance balun with dual-band operations,” *IEEE Antennas Wireless Propag. Lett.*, vol. 7, pp. 119-122, 2008.

[9] X. Gao, L. K. Yeung, and K. L. Wu, “A dual-band balun using partially coupled stepped-impedance coupled-line resonators,” *IEEE Trans. Microw. Theory Tech.*, vol. 56, no. 6, pp. 1455-1460, June 2008.

[10] L. K. Yeung, W. Cheng, and Y. E. Wang, “A dual-band balun using broadside-coupled coplanar striplines,” *IEEE Trans. Microw. Theory Tech.*, vol. 56, no. 8, pp. 1995-2000, Aug. 2008.

[11] J. Shao, H. Zhang, C. Chen, S. Tan, and K. J. Chen, “A compact dualband coupled-line balun with tapped open-ended stubs,” *Progr. Electromagn. Res. C*, vol. 22, pp. 109-122, 2011.

[12] L.-C. Tsai and C.-W. Hsue, “Dual-band bandpass filters using equal-length coupled-serial-shunted lines and Z-transform technique,” *IEEE Trans. Microw. Theory Tech.*, vol. 52, no. 4, pp. 1111-1117, Apr. 2004.

[13] Y. P. Zhang and M. Sun, “Dual-band microstrip bandpass filter using stepped-impedance resonators with new coupling schemes,” *IEEE Trans. Microw. Theory Tech.*, vol. 54, no. 10, pp. 3779-3785, Oct. 2006.

[14] C.-W. Tang and S.-F. You, “Using the technology of low temperature co-fired ceramic to design the dual-band bandpass filter,” *IEEE Microw. Wireless Compon. Lett.*, vol. 16, no. 7, pp. 407-409, Jul. 2006.

[15] H.-M. Lee and C.-M. Tsai, “Dual-band filter design with flexible passband frequency and bandwidth selections,” *IEEE Trans. Microw. Theory Tech.*, vol. 55, no. 5, pp. 1002-1009, May 2007.

[16] R. V. Gatti, A. Ocera, S. Bastioli, L. Marcaccioli, and R. Sorrentino, “A novel compact dual-band reconfigurable power divider for smart antenna systems,” *in IEEE MTT-S Int. Microw. Symp. Dig.*, pp. 423-426, Jun. 2007.

[17] Y. C. Chiou, C. Y. Wu, and J. T. Kuo, “New miniaturized dual-mode dual-band ring resonator bandpass filter with microwave c-sections,” *IEEE Microw. Wireless Compon. Lett.*, vol. 20, no. 2, pp. 67-69, Feb. 2010.

[18] S. Luo, L. Zhu, and S. Sun, “A dual-band ring-resonator bandpass filter based on two pairs of degenerate modes,” *IEEE Trans. Microw. Theory Tech.*, vol. 58, no. 12, pp. 3427-3432, Dec. 2010.

[19] R. Zhou, Z. Zhang, C. Chen, and H. Zhang, “Design of dual-band microwave duplexers,” *Electronics Letters*, vol. 50, no. 3, pp. 219-221, Jan. 2014.

[20] H. Zhang and X. Hao, “Design of dual-band Wilkinson power dividers with flexible frequency ratios,” *in IEEE MTT-S Int. Microw. Sump. Dig.*, 2008, pp. 1223-1226.

[21] Y. Wu, Y. Liu, and Q. Xue, “An analytical approach for a novel coupled-line dual-band Wilkinson power divider,” *IEEE Trans. Microw. Theory Tech.*, vol. 59, no. 2, pp. 286-294, Feb. 2011.

[22] H. Zhang and K. J. Chen, “A stub tapped branch-line coupler for dualband operations,” *IEEE Microw. Wireless Compon. Lett.*, vol. 17, no. 2, pp. 106-108, Feb. 2007.

[23] H. Zhang and K. J. Chen, “Design of dual-band rat-race couplers,” *IET Microw. Antennas Propag.*, vol. 3, no. 3, pp. 514-521, 2009.

[24] K. K. M. Cheng and S. Yeung, “A novel dual-band 3-dB branch-line coupler design with controllable bandwidths,” *IEEE Trans. Microw. Theory Tech.*, vol. 60, no. 10, pp. 3055-3061, Oct. 2012.

[25] X. Wang, W.-Y. Yin, and K.-L. Wu, “A dual-band coupled-line coupler with an arbitrary coupling coefficient,” *IEEE Trans. Microw. Theory Tech.*, vol. 60, no. 4, pp. 945-951, Apr. 2012.

[26] F. L. Wong and K. K. M. Cheng, “A novel, planar, and compact crossover design for dual-band applications,” *IEEE Trans. Microw. Theory Tech.*, vol. 59, no. 3, pp. 568-573, Mar. 2011.

[27] J. Shao, H. Ren, B. Arigong, C. Li, and H. Zhang, “A fully symmetrical crossover and its dual-freuqnecy application,” *IEEE Trans. Microw. Theory Tech.*, vol. 60, no. 8, pp. 2410-2416, Aug. 2012.

[28] H. Ren, J. Shao, R. Zhou, B. Arigong, H. S. Kim, C. Li, and H. Zhang, “A compact phased array antenna system based on dual-band Butler matrices,” *IEEE Raido and Wireless Symposium (RWS)*, pp. 214-216, 2013.

[29] K. K. M. Cheng and F.-L. Wong, “A novel approach to the design and implementation of dual-band compact planar 90° branch-line coupler,” *IEEE Trans. Microw. Theory Tech.*, vol. 52, no. 11, pp. 2458-2463, Nov. 2004.

[30] P.-L. Chi and T. Itoh, “Miniaturized dual-band directional couplers using composite right/left-handed transmission structures and their applications in beam pattern diversity systems,” *IEEE Trans. Microw. Theory Tech.*, vol. 57, no. 5, pp. 1207-1215, May 2009.

[31] C.-L. Hsu, J.-T. Kuo, and C.-W. Chang, “Miniaturized dual-band hybrid couplers with arbitrary power division ratios,” *IEEE Trans. Microw. Theory Tech.*, vol. 57, no. 1, pp. 149-156, Jan. 2009.

[32] S. Y. Zhang, S. H. Yeung, W. S. Chan, K. F. Man, S. H. Leung, and Q. Xue, “Dual-band rectangular patch hybrid coupler,” *IEEE Trans. Microw. Theory Tech.*, vol. 56, no. 7, pp. 1721-1728, Jul. 2008.

[33] H. Kim, B. Lee, and M.-J. Park, “Dual-band branch-line coupler with port extensions,” *IEEE Trans. Microw. Theory Tech.*, vol. 58, no. 3, pp. 651-655, Mar. 2010.

[34] K.-S. Chin, K.-M. Lin, Y.-H. Wei, T.-H. Tseng, and Y.-J. Yang, “Compact dual-band branch-line and rat-race couplers with stepped-impedance-stub lines,” *IEEE Trans. Microw. Theory Tech.*, vol. 58, no. 5, pp. 1213-1221, May 2010.

[35] L. K. Yeung, “A compact dual-band 90° coupler with coupled-line sections,” *IEEE Trans. Microw. Theory Tech.*, vol. 59, no. 9, pp. 2227-2232, Sep. 2011.

[36] C.-Y. Liou, M.-S. Wu, J.-C. Yeh, Y.-Z. Chueh, and S.-G. Mao, “A novel triple-band microstrip branch-line coupler with arbitrary operating frequencies,” *IEEE Microw. Wireless Compon. Lett.*, vol. 19, no. 11, pp. 683-685, 2009.

[37] F. Lin, Q.-X. Chu, and Z. Lin, “A novel tri-band branch-line coupler with three controllable operating frequencies,” *IEEE Microw. Wireless Compon. Lett.*, vol. 20, no. 12, pp. 666-668, 2010.

[38] H. J. Moody, “The systematic design of the Butler matrix,” *IEEE Trans. Antennas Propag.*, vol. 12, no. 6, pp. 786-788, Nov. 1964.

[39] T. Macnamara, “Simplified design procedures for Butler matrices incorporating 90° hybrids or 180° hybrids,” *Microwaves, Antennas and Propagation, IEE Proceedings H*, vol. 134, no. 1, pp. 50-54, Feb. 1987.

[40] C. H. Tseng, C. J. Chen, and T. H. Chu, “A low-cost 60-GHz switched-beam patch antenna array with Butler matrix network,” *IEEE Antennas Wireless Propag. Lett.*, vol. 7, pp. 432-435, 2008.

[41] H. Ren, J. Shao, R. Zhou, B. Arigong, and H. Zhang, “Compact phased array antenna system based on dual-band operations,” *Microw. Opt. Technol. Lett.*, vol. 56, no. 6, pp. 1391-1396, Jun. 2014.

[42] H. T. Nguyen, K. S. Ang, and G. I. Ng, “Design of a broad-band novel Butler matrix,” *in Proc. Asia-Pacific Microw. Conf.*, pp. 753-756, 2011.

[43] G. Tian, J.-P. Yang, and W. Wu, “A novel compact Butler matrix without phase shifter,” *IEEE Microw. Wireless Compon. Lett.*, vol. 24, no. 5, pp. 306-308, May 2014.

[44] A. M. Martir, I. M. Fernandez, and A. O. Monux, “Wideband slot-coupled Butler matrix,” *IEEE Microw. Wireless Compon. Lett.*, vol. 24, no. 12, pp. 848-850, Dec. 2014.

[45] K. Staszek, S. Gruszczynski, and K. Wincza, “Broadband measurements of S-parameters with the use of a single 8 × 8 Butler matrix,” *IEEE Trans. Microw. Theory Tech.*, vol. 62, no. 2, pp. 352-360, Feb. 2014.

[46] N. Sutton, and D. S. Filipovic, “Design of a K- thru Ka-band modified Butler matrix feed for a 4-arm spiral antenna,” *in Proc. Antennas and Propagation Conf.*, pp. 521-524, 2010.

[47] Y. S. Wong, S. Y. Zheng, and W. S. Chan, “Quasi-arbitrary phase-difference hybrid coupler,” *IEEE Trans. Microw. Theory Tech.*, vol. 60, no. 6, pp. 1530-1539, Jun. 2012.

[48] Y. Wu, J.-Y. Shen, Y. Liu, S.-W. Leung, and Q. Xue, “Miniaturized arbitrary phase-difference couplers for arbitrary coupling coefficients,” *IEEE Trans. Microw. Theory Tech.*, vol. 61, no. 6, pp. 2317-2324, Jun. 2013.

[49] A. K. Geim and K. S. Novoselov, “The rise of graphene,” *Nat. Mater.*, vol. 6, pp. 183-191, 2007.

[50] K. S. Novoselov, A. K. Geim, S. V. Morozor, D. Jiang, Y. Zhang, S. V. Dubonos, I. V. Grigorieva, and A. A. Firsov, “Electric field effect in atomically thin carbon films,” *Science*, vol. 306, no. 5696, pp. 666-669, Oct. 2004.

[51] A. H. C. Neto, F. Guinea, N. M. R. Peres, K. S. Novoselov, and A. K. Geim, “The electronic properties of graphene,” *Rev. Mod. Phys.*, vol. 81, no. 1, pp. 109-162, Jan. 2009.

[52] A. S. Mayorov, R. V. Gorbachev, S. V. Morozov, L. Britnell, R. Jalil, L. A. Ponomarenko, P. Blake, K. S. Novoselov, K. Watanabe, T. Taniguchi, and A. K. Geim, “Micrometer-scale ballistic transport in encapsulated graphene at room temperature,” *Nano Lett.*, vol. 11, no. 6, pp. 2396-2399, May 2011.

[53] H. S. P. Wong, and D. J. Akinwande, *Carbon Nanotube and Graphene Device Physics*, Cambridge University Press: Cambridge, 2011.

[54] Y. Zhang, Y. -W. Tan, H. L. Stormer, and P. Kim, “Experimental observation of the quantum Hall effect and Berry’s phase in graphene,” *Nature*, vol. 438, pp. 201-204, Nov. 2005.

[55] Z. Q. Li, E. A. Henriksen, Z. Jiang, Z. Hao, M. C. Martin, P. Kim, H. L. Stormer, D. N. Basov, “Dirac charge dynamics in graphene by infrared spectroscopy,” *Nat. Phys.*, vol. 4, pp. 532-535, Jun. 2008.

[56] A. Vakil and N. Engheta, “Transformation optics using graphene,” *Science*, vol. 332, no. 6035, pp. 1291-1294, Jun. 2011.

[57] G. W. Hanson, “Dyadic Green’s functions for an anisotropic, non-local model of biased graphene,” *IEEE Trans. Antenna Propag.*, vol. 56, no. 3 pp. 747-757, Mar. 2008.

[58] P. Y. Chen and A. Alù, “Atomically thin surface cloak using graphene monolayers,” *ACS Nano*, vol. 5, no. 7, pp. 5855-5863, Jun. 2011.

[59] V. P. Gusynin, S. G. Sharapov, and J. P. Carbotte, “Magneto-optical conductivity in graphene,” *J. Phys.: Cond. Mater.*, vol. 19, no. 2, pp. 026222, Jan. 2007.

[60] L. A. Falkovsky and S. S. Pershoguba, “Optical far-infrared properties of a graphene monolayer and multilayer,” *Phys. Rev. B*, vol. 76, pp. 153410, 2007.

[61] F. T. Chuang, P. Y. Chen, T. C. Cheng, C. H. Chien, and B. J. Li, “Improved field emission properties of thiolated multi-wall carbon nanotubes on a flexible carbon cloth substrate,” *Nanotech.*, vol. 18, no. 39 pp. 395702, Oct. 2007.

[62] F. Rana, “Graphene terahertz plasmon oscillators,” *IEEE Trans. Nanotechnol.*, vol. 7, no. 1, pp. 91-99, Jan. 2008.

[63] P. Y. Chen and A. Alù, “Terahertz metamaterial devices based on graphene nanostructures,” *IEEE Trans. Terahertz Sci. Technol.*, vol. 3, no. 6, pp. 748-756, Nov. 2013.

[64] A. Cabellos, I. Llatser, E. Alarcón, A. Hsu, and T. Palacios, “Use of THz photoconductive sources to characterize tunable graphene RF plasmonic antennas,” *IEEE Trans. Nanotechnol.*, vol. 14, no. 2, pp. 390-396, Mar. 2015.

[65] X. C. Wang, W. S. Zhao, J. Hu, and W. Y. Yin, “Reconfigurable terahertz leaky-wave antenna using graphene-based high-impedance surface,” *IEEE Trans. Nanotechnol.*, vol. 14, no. 1, pp. 62-69, Jan. 2015.

[66] M. Tamagnone, J. S. Gomez-Diaz, J. R. Mosig, and J. Perruisseau-Carrier, “Reconfigurable terahertz plasmonic antenna concept using a graphene stack,” *Appl. Phys. Lett.*, vol. 101, pp. 214102, Nov. 2012.

[67] Z. Xu, X. Dong, and J. Bornemann, “Design of a reconfigurable MIMO system for THz communications based on graphene antennas,” *IEEE Trans. Terahertz Sci. Technol.*, vol. 4, no. 5, pp. 609-617, Sep. 2014.

[68] J. S. Gómez-Díaz, M. Esquius-Morote, and J. Perruisseau-Carrier, “Plane wave excitation-detection of non-resonant plasmons along finite-width graphene strips,” *Opt. Express*, vol. 21, no. 21. pp. 24856-24872, Oct. 2013.

[69] M. Esquius-Morote, J. S. Gómez-Díaz, and J. Perruisseau-Carrier, “Sinusoidally-modulated graphene leaky-wave antenna for electronic beam-scanning at THz,” *IEEE Trans. Terahertz Sci. Technol.*, vol. 4, no. 1, pp. 116-122, Jan. 2014.

[70] E. Carrasco and J. Perruisseau-Carrier, “Reflectarray antenna at terahertz using graphene,” *IEEE Antennas Wireless Propag. Lett.*, vol. 12, pp. 253-256, 2013.

[71] D. Correas-Serrano, J. S. Gomez-Diaz, J. Perruisseau-Carrier, and A. Álvarez-Melcón, “Graphene-based plasmonic tunable low-pass filters in the terahertz band,” *IEEE Trans. Nanotechnol.*, vol. 13, no. 6, pp. 1145-1153, Nov. 2014.

[72] H. Deng, Y. Yan, and Y. Yu, “Tunable flat-top bandpass filter based on coupled resonators on a graphene sheet,” *IEEE Photon. Technol. Lett.*, vol. 27, no. 11, pp. 1161-1164, Jun. 2015.

[73] Y. Huang, L. S. Wu, M. Tang, and J. Mao, “Design of a beam reconfigurable THz antenna with graphene-based switchable high-impedance surface,” *IEEE Trans. Nanotechnol.*, vol. 13, no. 1, pp. 70-79, Jan. 2014.

[74] P. Sharma, J. P. Carrier, C. Moldovan, and A. M. Ionescu, “Electromagnetic performance of RF NEMS graphene capacitive switches,” *IEEE Trans. Nanotechnol.*, vol. 11, no. 4, pp. 836-842, Jul. 2012.

[75] J. S. Gómez-Díaz, and J. Perruisseau-Carrier, “Graphene-based plasmonic switches at near infrared frequencies,” *Opt. Express*, vol. 21, no. 13, pp. 15490-15504, Jul. 2013.

[76] P. Y. Chen, C. Argyropoulos, and A. Alù, “Terahertz antenna phase shifters using integrally-gated graphene transmission-lines,” *IEEE Trans. Antennas Propag.*, vol. 61, no. 4, pp. 1528-1537, Apr. 2013.

[77] A. Fallahi and J. Perruisseau-Carrier, “Manipulation of giant faraday rotation in graphene metasurfaces,” *Appl. Phys. Lett.*, vol. 101, pp. 231605, Dec. 2012.

[78] D. L. Sounas, H. S. Skulason, H. V. Nguyen, A. Guermoune, M. Siaj, T. Szkopek, and C. Caloz, “Faraday rotation in magnetically-biased graphene at microwave frequencies,” *Appl. Phys. Lett.*, vol. 102, pp. 191901, May 2013.

[79] P. Y. Chen, J. Soric, Y. R. Padooru, H. M. Bernety, A. B. Yakovlev, and A. Alù, “Nanostructured graphene metasurface for tunable terahertz cloaking,” *New J. Phys.*, vol. 15, pp. 123029, Dec. 2013.

[80] Z. Fang, Y. Wang, A. E. Schlather, Z. Liu, P. M. Ajayan, F. J. García de Abajo, P. Nordlander, X. Zhu, and N. J. Halas, “Active tunable absorption enhancement with graphene nanodisk arrays,” *Nano Lett.*, vol. 14, no. 1, pp. 299-304, 2014.

[81] M. Liu, X. Yin, E. Ulin-Avila, B. Geng, T. Zentgraf, L. Ju, F. Wang, and X. Zhang, “A graphene-based broadband optical modulator,” *Nature*, vol. 474, pp. 64-67, Jun. 2011.

[82] M. Liu, X. Yin, and X. Zhang, “Double-layer graphene optical modulator,” *Nano Lett.*, vol. 12, no. 3, pp. 1482-1485, Feb. 2012.

[83] Z. Fang, S. Thongrattanasiri, A. Schlather, Z. Liu, L. Ma, Y. Wang, P. M. Ajayan, P. Nordlander, and N. J. Halas, “Gated tenability and hybridization of localized plasmons in nanostructured graphene,” *ACS Nano*, vol. 7, no. 3, pp. 2388-2395, Feb. 2013.

[84] V. Ryzhii, M. Ryzhii, V. Mitin, M. S. Shur, and T. Otsuji, “Terahertz photomixing using plasma resonances in double-graphene layer structures,” *J. Appl. Phys.*, vol. 113, pp. 174506, May 2013.

[85] P. Y. Chen and A. Alù, “A terahertz photomixer based on plasmonic nanoantennas coupled to a graphene emitter,” *Nanotechnology*, vol. 24, pp. 455202, 2013.

[86] Q. Bao, H. Zhang, B. Wang, Z. Ni, C. Haley, Y. X. Lim, Y. wang, D. Y. Tang, and K. P. Loh, “Broadband graphene polarizer,” *Nat. Photonics*, vol. 5, pp. 411-415, May 2011.

[87] S. Rakheja, Y. Wu, H. Wang, T. Palacios, P. Avouris, and D. A. Antoniadis, “An ambipolar virtual-source-based charge-current compact model for nanoscale graphene transistors,” *IEEE Trans. Nanotechnol.*, vol. 13, no. 5, pp. 1005-1013, Sep. 2014.

[88] M. Foxe, G. Lopez, I. Childres, R. Jalilian, A. Patil, C. Roecker, J. Boguski, I. Jovanovic, and Y. P. Chen, “Graphene field-effect transistors on undoped semiconductor substrates for radiation detection,” *IEEE Trans. Nanotechnol.*, vol. 11, no. 3, pp. 581-587, May 2012.

[89] G. M. Landauer, D. Jimenez, and J. L. Gonzalez, “An accurate and Verilog-A compatible compact model for graphene field-effect transistors,” *IEEE Trans. Nanotechnol.*, vol. 13, no. 5, pp. 895-904, Sep. 2014.

[90] B. W. Scott and J. Leburton, “Modeling of the output and transfer characteristics of graphene field-effect transistors,” *IEEE Trans. Nanotechnol.*, vol. 10, no. 5, pp. 1113-1119, Sep. 2011.

[91] S. Fregonese, M. Magallo, C. Maneux, H. Happy, and T. Zimmer, “Scalable electrical compact modeling for graphene FET transistors,” *IEEE Trans. Nanotechnol.*, vol. 12, no. 4, pp. 539-546, Jul. 2013.

[92] G. W. Hanson, “Quasi-transverse electromagnetic modes supported by a graphene parallel-plate waveguide,” *J. Appl. Phys.*, vol. 104, pp. 084314, Oct. 2008.

[93] M. Dressel, and G. Grüner, *Electrodynamics of Solids*, Cambridge University Press: London, 2002.

[94] S. E. Kocabas, G. Veronis, D. A. B. Miller, and S. Fan, “Transmission line and equivalent circuit models for plasmonic waveguide components,” *IEEE Quan. Electron.*, vol. 14, no. 6, pp. 1462-1472, 2008.

[95] P. Y. Chen, H. Huang, D. Akinwande, and A. Alù, “Graphene-based plasmonic platform for reconfigurable terahertz nanodevices,” *ACS Photonics*, vol. 1, no. 8, pp. 647-654, Jul. 2014.

[96] S. A. Thiele, J. A. Schaefer, and F. Schwierz, “Modeling of graphene metal-oxide-semiconductor field-effect transistors with gapless large-area graphene channels,” *J. Appl. Phys.*, vol. 107, pp. 094505, May 2010.

[97] K. N. Parrish, and D. Akinwande, “An exactly solvable model for the graphene transistor in the quantum capacitance limit,” *Appl. Phys. Lett.*, vol. 101, pp. 053501, Jul. 2012.

[98] H. Cheng, S. Chen, P. Yu, X. Duan, B. Xie, and J. Tian, “Dynamically tunable plasmonically induced transparency in periodically patterned graphene nanostrips,” *Appl. Phys. Lett.*, vol. 103, pp. 203112, Nov. 2013.

[99] S. Thongrattanasiri, A. Manjavacas, and F. J. García de Abajo, “Quantum finite-size effects in graphene plasmons,” *ACS Nano*, vol. 6, no. 2, pp. 1766-1775, Jan. 2012.

[100] H. Ren, J. Shao, M. Zhou, B. Arigong, J. Ding, and H. Zhang, “Design of dual-band transmission line with flexible phase shifts and its applications,” *Electron. Lett.*, vol. 51, no. 3, pp. 261-262, Feb. 2015.

[101] N. Yu, P. Genevet, M. A. Kats, F. Aieta, J. -P. Tetienne, F. Capasso, and Z. Gaburro, “Light propagation with phase discontinuities: generalized laws of reflection and refraction,” *Science*, vol. 334, no. 6054, pp. 333-337, Oct. 2011.

[102] F. Aieta, P. Genevet, M. A. Kats, N. Yu, R. Blanchard, Z. Gaburro, and F. Capasso, “Aberration-free ultrathin flat lenses and axicons at telecom wavelengths based on plasmonic metasurfaces,” *Nano Lett.*, vol. 12, no. 9, pp. 4932-4936, Aug. 2012.

[103] X. Chen, L. Huang, H. Mühlenbernd, G. Li, B. Bai, Q. Tan, G. Jin, C.-W. Qiu, S. Zhang, and T. Zentgraf, “Dual-polarity plasmonic metalens for visible light,” *Nat. Commun.*, vol. 3, p. 1198, Nov. 2012.

[104] X. Ni, S. Ishii, A. V. Kildishev, and V. M. Shalaev, “Ultra-thin, planar, Babinet-inverted plasmonic metalenses,” *Light: Sci. Appl.*, vol. 2, no.4, p. e72, Apr. 2013.

[105] A. Pors, M. G. Nielsen, R. L. Eriksen, and S. I. Bozhevolnyi, “Broadband focusing flat mirrors based on plasmonic gradient metasurfaces,” *Nano Lett.*, vol. 13, no. 2, pp. 829-834, Jan. 2013.

[106] A. S. Roberts, A. Pors, O. Albrektsen, and S. I. Bozhevolnyi, “Subwavelength plasmonic color printing protected for ambient use,” *Nano Lett.*, vol. 14, no. 2, pp. 783-787, Jan. 2014.

[107] S. Larouche, Y. -J. Tsai, T. Tyler, N. M. Jokerst, and D. R. Smith, “Infrared metamaterial phase holograms,” *Nat. Mater.*, vol. 11, pp. 450-454, Mar. 2012.

[108] X. Ni, A. V. Kildishev, and V. M. Shalaev, “Metasurface holograms for visible light,” *Nat. Commun.*, vol. 4, Nov. 2013.

[109] J. Hao, Y. Yuan, L. Ran, T. Jiang, J. A. Kong, C. T. Chan, and L. Zhou, “Manipulating electromagnetic wave polarizations by anisotropic metamaterials,” *Phys. Rev. Lett.*, vol. 99, no. 6, pp. 063908, Aug. 2007.

[110] J. B. Pendry, A. J. Holden, D. J. Robbins, and W. J. Stewart, “Magnetism from conductors and enhanced nonlinear phenomena,” *IEEE Trans. Microw. Theory Tech.*, vol. 47, no. 11, pp. 2075-2084, Nov. 1999.

[111] D. R. Smith, W. J. Padilla, D. C. Vier, S. C. Nemat-Nasser, and S. Schultz, “Composite medium with simultaneously negative permeabiity and permittivity,” *Phys. Rev. Lett.*, vol. 84, no. 18, pp. 4184-4187, May 2000.

[112] J. Li, S. Chen, H. Yang, J. Li, P. Yu, H. Cheng, C. Gu, H. -T. Chen, and J. Tian, “Simultaneous control of light polarization and phase distributions using

plasmonic metasurfaces," *Adv. Funct. Mater.*, vol. 25, no. 5, pp. 704–710, Dec. 2014.

[113] S. Sun, Q. He, S. Xiao, Q. Xu, X. Li, and L. Zhou, "Gradient-index meta-surfaces as a bridge linking propagating waves and surface waves," *Nature Mater.*, vol. 11, pp. 426-431, Apr. 2012.

[114] X. Zhang, Z. Tian, W. Yue, J. Gu, S. Zhang, J. Han, and W. Zhang, "Broadband terahertz wave deflection based on c-shape complex metamaterials with phase discontinuities," *Adv. Mater.*, vol. 25, no. 33, pp. 4567-4572, Jun. 2013.

[115] B. O. Zhu, J. Zhao, and Y. Feng, "Active impedance metasurface with full 360° reflection phase tuning," *Sci. Rep.*, vol. 3: 3059, Oct. 2013.

[116] T. Jiang, Z. Wang, D. Li, J. Pan, B. Zhang, J. Huangfu, Y. Salamin, C. Li, and L. Ran, "Low-DC voltage-controlled steering-antenna radome utilizing tunable active metamaterial," *IEEE Trans. Terahertz Sci. Technol.*, vol. 60, no. 1, pp. 170-178, Jan. 2012.

[117] Y. Wang, J. Yin, G. Yuan, X. Dong, and C. Du, "Tunable I-shaped metamaterial by loading varactor diode for reconfigurable antenna," *Appl. Phys. A*, vol. 104, pp. 1243-1247, May 2011.

[118] M. Farmahini-Farahani, J. Cheng, and H. Mosallaei, "Metasurfaces nanoantennas for light processing," *J. Opt. Soc. Amer. B*, vol. 30, no. 9, pp. 2365-2370, Sep. 2013.

[119] M. Kim, H. Wong, M. Alex, and G. V. Eleftheriades, "Optical huygens' metasurfaces with independent control of the magnitude and phase of the local reflection coefficients," *Phys. Rev. X*, vol. 4, p. 041042, Dec. 2014.

[120] C. Pfeiffer, C. Zhang, V. Ray, L. J. Guo, and A. Grbic, "High performance bianisotropic metasurfaces: Asymmetric transmission of light," *Phys. Rev. Lett.*, vol. 113, no. 2, p. 023902, Jul. 2014.

[121] L. Liu, X. Zhang, M. Kenney, X. Su, N. Xu, C. Ouyang, Y. Shi, J. Han, W. Zhang, and S. Zhang, "Broadband metasurfaces with simultaneous control of phase and amplitude," *Adv. Mater.*, vol. 26, no. 29, pp. 5031-5036, May 2014.

[122] B. O. Zhu, K. Chen, N. Jia, L. Sun, J. Zhao, T. Jiang and Y. Feng, "Dynamic control of electromagnetic wave propagation with the quivalent principle inspired tunable metasurface," *Sci. Rep.*, vol. 4: 4971, May 2014.

[123] M. Esquius-Morote, J. Gomez-Diaz, and J. Perruisseau-Carrier, "Sinusoidally modulated graphene leaky-wave antenna for electronic beamscanning at THz," *IEEE Trans. Terahertz Sci. Technol.*, vol. 4, no. 1, pp. 116-122, Jan. 2014.

[124] J. Y. Lau, S. V. Hum, “Analysis and Characterization of a Multipole Reconfigurable Transmitarray Element,” *IEEE Trans. Antenna Propag.*, vol. 59, no. 1 pp. 70-79, Jan. 2011.

[125] C. A. Balanis, *Antenna Theory: Analysis and Design*, 3rd ed. Hoboken, NJ: Wiley, 2005.

[126] N. Marcuvitz, *Waveguide Handbook*, New York: McGraw-Hill, 1951.

[127] M. L. Crawford, “Generation of standard electromagnetic fields using TEM transmission cells,” *IEEE Transactions on Electromagnetic Compatibility*, vol. EMC-16, pp. 189-195, Nov. 1974.